Quantitative Modeling and Control of Nascent Sprout Geometry in *In Vitro* Angiogenesis

by

Levi Benjamin Wood

B.S., Mechanical Engineering, Oregon State University, 2004

S.M., Mechanical Engineering, Massachusetts Institute of Technology, 2008

S.M., Electrical Engineering and Computer Science, Massachusetts Institute of Technology, 2008

Submitted to the Department of Mechanical Engineering
in partial fulfillment of the requirements for the degree of

Doctor of Philosophy

at the

MASSACHUSETTS INSTITUTE OF TECHNOLOGY

February 2012

Author .....
Department of Mechanical Engineering
October 31, 2011

Certified by .....
H. Harry Asada
Ford Professor of Mechanical Engineering
Thesis Supervisor

Accepted by .....
David E. Hardt
Chairman, Department Committee on Graduate Students

Quantitative Modeling and Control of Nascent Sprout Geometry in *In Vitro* Angiogenesis

by

Levi Benjamin Wood

Submitted to the Department of Mechanical Engineering
on October 31, 2011, in partial fulfillment of the
requirements for the degree of
Doctor of Philosophy

Abstract

Nascent blood vessel growth in angiogenesis is a complex process involving cellular response to biochemical growth factors, degradation of the surrounding matrix, and coordinated migration of multiple endothelial cells up a growth factor gradient. Mechanistic understanding and quantitative modeling of the dominant dynamics involved in nascent vessel growth will enable new strategies for regulating vessel growth rate and geometry, and will have implications in controlling growth of complete vascular networks in many research areas, ranging from cancer treatment and wound healing to tissue engineering.

In this thesis, we investigate the dynamics of nascent vessel growth in 3D microfluidic assays, formulate a quantitative process model based on our experimental characterization, and formulate a feedback approach to regulate growth. We begin by developing a new microfluidic assay consisting of a collagen gel scaffold with features to reduce assay-to-assay variability and increase experimental throughput. This high throughput assay reveals that there is an inverse relationship between nascent vessel elongation rate and diameter under diverse biochemical conditions. This finding is supported by immunofluorescent staining and biochemical inhibition studies, which give insight into the dominant mechanisms determining nascent vessel diameter. Based on our experimental characterization, we formulate a simple quantitative reaction-diffusion model that relates vessel diameter to elongation rate, and supports our understanding of the relevant dynamics. We conclude by formulating a model-based optimization approach for planning the optimal trajectory of elongation rate vs. time needed to obtain desired sprout geometry, and illustrate in simulation that model predictive feedback control can be used to correct for noise in the response of elongation rate to growth factor inputs.

Thesis Supervisor: H. Harry Asada
Title: Ford Professor of Mechanical Engineering

Acknowledgments

My success, both in finishing this thesis and finishing the last eleven years of my education, is due to the support I have had from my advisor, thesis committee, friends, and family. I could not have done it without any of them.

I would like to thank Professor Asada for everything he has taught me about conducting and disseminating exciting research, and for involving my in this interdisciplinary research project that has opened my eyes to the exciting world of engineering biology. I am privileged to have worked with an advisor who has introduced me to such a breadth of analytic and experimental research topics. I want to thank Professor Kamm for inviting me to work in his lab as part of the NSF Emerging Frontiers and Innovation (EFRI) project and constantly being available to discuss ideas and problems. His leadership in the EFRI project has inspired me to pursue an academic career. Thank you to Professor Lauffenburger for providing much support and many ideas throughout this project. His enthusiastic, yet pragmatic evaluation of our ideas for combining experiments, modeling, and control have been immensely helpful in shaping this thesis. Just as importantly, thank you to Professor Tedrake for agreeing to sit on my committee through a very unusual control project and for supporting my modeling approach when it was unclear whether it would work.

All of the students and postdocs in the Asada and Kamm labs have played a huge role in my learning and professional growth. I feel that I have a home in both labs and the many friendships in both are immeasurably important to me. There are too many friends to list, but I want to especially thank Yannis, Joy, Waleed, and Alisha, who have been outstanding colleagues on the EFRI project. I couldn't have made any progress without their continued support. During this project, I spent 6 months working with our Singapore based colleagues. I want to thank Sharon Ong and Min-Cheol for making my stay in Singapore intellectually stimulating and a lot of fun. Lastly, I want to give a very special thanks to my girlfriend, Cherry, for putting up with me working constantly during the last two years and for giving me so much great advice on research, interpersonal problems, and professional advancement.

Cherry and I met in the Kamm lab two years ago, and to me, meeting her is the single most important outcome of this project.

I would like to thank my grandparents, Lawrence and Barbara, for taking a special concern in my developmental education and for making it possible for me to go to college at the age of 14. I would not be the person I am today without their loving support. I wish to thank my aunt, Glenda, for helping me find what I am capable of and for helping me go to college. I wish to thank my parents, Lonnie and Raquel, who have been tremendously supportive since I left home and who are constantly a stabilizing force in my life. I would also like to thank my undergraduate advisor and friend Dr. Jeff Hayen. He helped guide my early introduction to science and engineering as well as my direction in graduate school and taught me solid analytical skills that aid me in every research project. I want to conclude by thanking my first boss and dear friend, Sharon Miller. She has been one of the most important influences in my life, always believing that I could achieve more and reach higher, and she has always been ready to help me and give good advice for dealing with every situation.

Contents

List of Figures

List of Tables

Chapter 1

Introduction

1.1 Angiogenesis in Development and Tissue Engineering

Angiogenesis is the process of sprouting and growing new blood vessels from pre-existing blood vessels in the body [27]. Coordinated vascular growth is essential for perfusing developing thick tissues ($> 100\mu$m thick) *in vitro* that can be successfully engrafted into the body [48], has been shown to provide essential guidance cues for organ development [47], and is essential for perfusing wounded and ischemic tissues [74]. Promoting growth of coordinated vascular networks remains one of the main challenges in growing thick tissues and organs *in vitro* [39]. Understanding how to promote successful angiogenic growth will play an important role in each of these fields.

The objective of this thesis is to understand how to reliably regulate vascular growth using an active feedback approach.

1.2 Mechanisms of Angiogenic Growth

Vascular network growth in angiogenesis is initiated when tip cells are selected from endothelial cells (ECs) in pre-existing vasculature in response to biochemical factors,

such as vascular endothelial growth factor (VEGF), among a multitude of others [27, 29]. See Fig. 1-1. The tip cells proteolyze extracellular matrix (ECM), of which type I collagen is the main structural constituent [8], enabling them to chemotactically migrate and leaving a cleaved conduit behind them in the ECM [14, 73]. Endothelial stalk cells migrate and proliferate in this conduit behind the tip cell, and configure themselves in a lumen structure to form the stalk of the new vasculature [36]. Eventually the new vessels branch and anastomose to form a network as shown in Fig. 1-1C. *In vivo*, as the network matures, a "pruning" process eliminates some of the

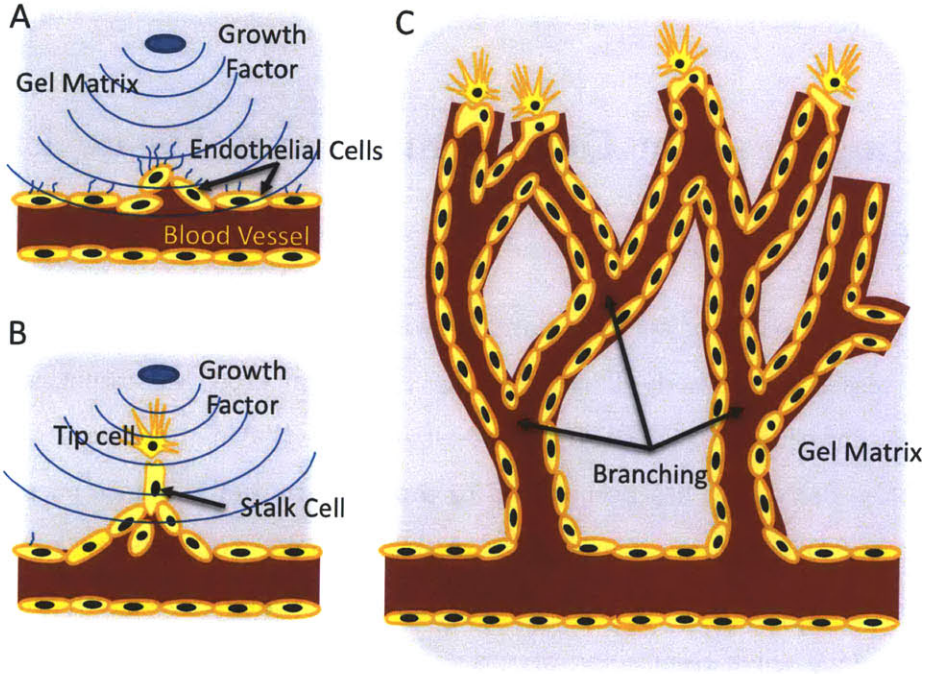

Figure 1-1: Illustration of angiogenic sprouting process. (A) ECs residing in a blood vessel sprout out in response to growth factor molecules. (B) A leading tip cell, detects gradients in certain growth factors, cleaves the ECM, and chemotactically migrates toward the growth factor source while stalk cells follow behind the tip. (C) New sprouts branch at multiple stages and anastamose to form a new vascular network.

many sprouts [57]. Finally, flow induction and attraction of pericyte and smooth muscle mural cells stabilize the sprouts and a tiered network forms [57]. The network maturation process is very complex and has been heavily studied [36, 30, 16, 57]. In this thesis, we restrict our attention to the early stage nascent vessel formation before pruning and stabilization.

1.3 Microfluidic Angiogenesis Models

Recent advances in 3D microfludic angiogenesis models [15] provide important tools for both investigating and regulating angiogenic growth. Fig. 1-2 shows the device used for angiogenesis experiments. A collagen gel matrix is formed between micro-

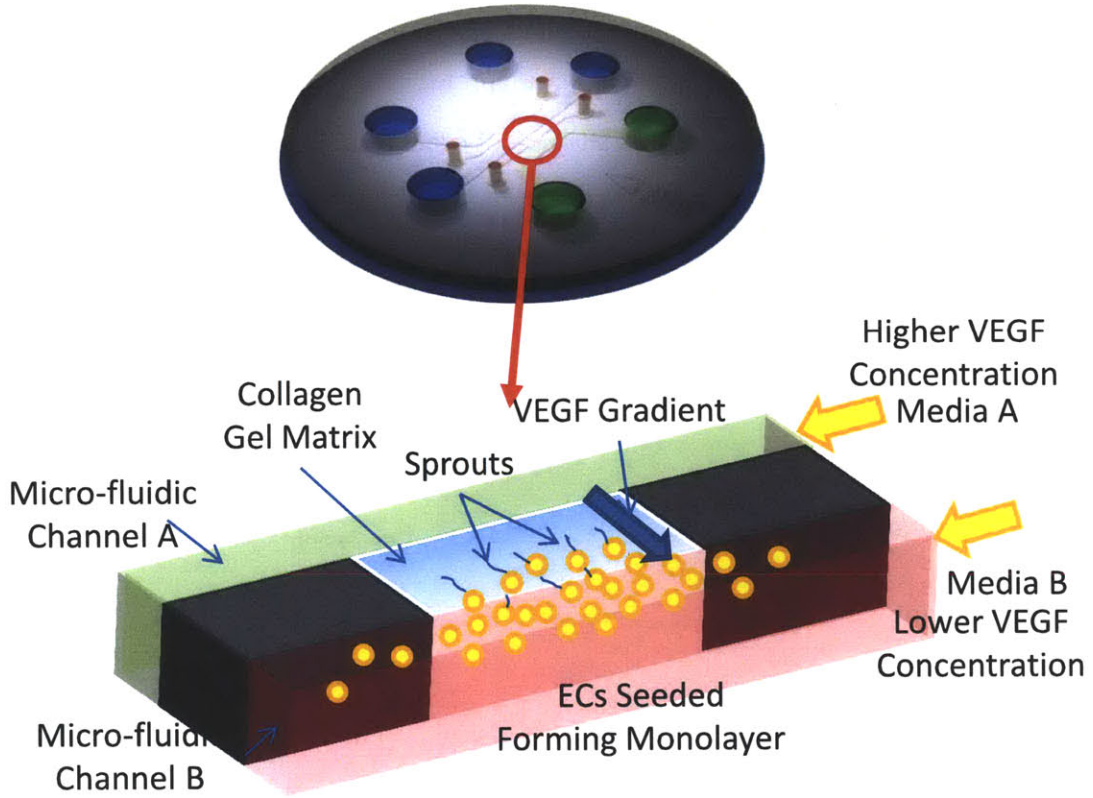

Figure 1-2: Schematic of microfluidic angiogensis model used in [15].

fluidic channels A and B (see fabrication details in Appendix A.1). Human Micro-Vascular Endothelial Cells (hMVEC) are seeded on one side of the gel matrix facing Channel B. Fluids containing growth factors and other molecules are delivered to the gel matrix through both channels. The fluid provided to Channel A usually contains a higher concentration level of VEGF than that of Channel B, so that a uniform gradient of VEGF concentration can be formed across the gel matrix. In response to the gradient of VEGF provided, ECs sprout out and extend towards the higher VEGF

concentration. The sprouting process is observed from beneath using a confocal or widefield microscope, from which we can observe the evolution of individual ECs and the total sprout morphology.

Fig. 1-3 shows an example phase contrast experiment taken from one of the microfluidic device designs used by Chung et al. in [15]. The device enables us to observe growth in response to multiple concentrations and gradients of VEGF and other angiogenic factors (e.g. sphingosine-1-phosphate [20], platelet derived growth factor [31], angiopoietins 1 and 2 [1], among a multitude of others) under tightly regulated biophysical and biochemical conditions. Furthermore, this platform provides a means of observing growth in real time and actively regulating growth by manipulating the application of angiogenic factors in channels A and B.

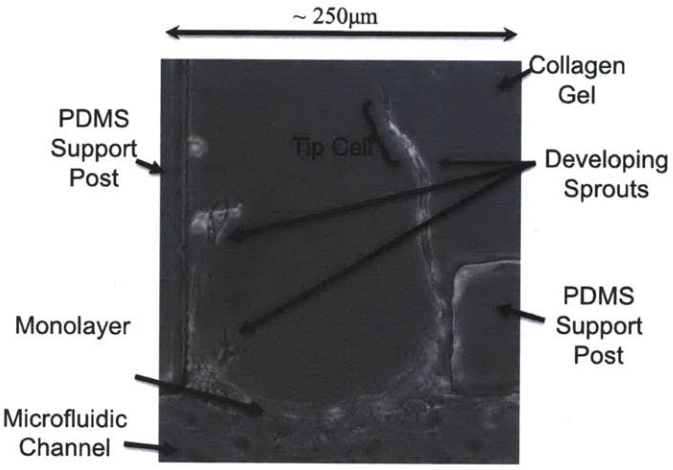

Figure 1-3: Phase contrast image of nascent sprouts grown in microfluidic platform from [15].

1.4 Regulating Growth

1.4.1 Prior Work in Angiogenic Regulation

Many previous studies have attempted to grow vascular networks *in vitro*. These studies have been targeted at attempting to reproduce *in vivo* conditions in an *in*

vitro setting, including embedding angiogenic growth factors into the matrix scaffold [22], co-culturing mural cell types with vascular endothelial cells [42], micropatterning molds to mimic *in vivo* vasculature that are later seeded with ECs [43], and ECM scaffold fabrication by decellularization of mouse hearts, later seeded with ECs [60].

These attempts have had some success, but are not yet fully functional [39], and successful and reliable growth remains a challenging issue. These prior works have attempted to engineering and regulate vascular growth using passive approaches in the sense that they do not monitor growth and actively change conditions to make corrections. In this thesis, we will take an active approach to regulating growth into a 3D ECM with no preexisting patterning.

1.4.2 Feedback Approach

Microfluidic technology (like in Fig. 1-2) opens up the possibility of actively controlling the angiogenic growth process. As shown in Fig. 1-4, we can use a process model to determine the best time-sequence of biochemical factors to apply in channels A and B to obtain desired growth. Furthermore, we can observe vessel growth in real time and close the loop to correct for error in the vessel growth.

Model based control and feedback are widely implemented in traditional engineering problems ranging from aircraft autopilots and robotics to chemical process control and are adaptable here. While many control approaches exist for determining the best sequence of conditions to apply, a technique known as model predictive control (MPC) has been widely used in chemical process control among many other amplifications to regulate systems with large time delay and nonlinearities [65, 12].

However, angiogenesis and cell population growth processes differ in many ways from traditional engineered systems where control technology has been successfully applied. First, the system consists of a population of EC's, each interacting with nearby cells, the ECM, and responding to exogenous biochemical inputs. Second, cells live in a "wet" environment, where biochemical inputs propagate through diffusion and influence broad regions of the cells. It is infeasible to directly control the behavior of each and every cell in the population. Available inputs are broadcast in nature,

influencing the multitude of cells. Further, it is not necessary, or even desirable, to control each and every cell. In generating a vascular network, the system as a whole should satisfy certain collective requirements, such as vascular density in the matrix, rate of branching, rate of growth, vessel diameter, or others. Rather than the behavior of each individual cell, correct development of the cellular population as a whole is important in growing a useful vascular system.

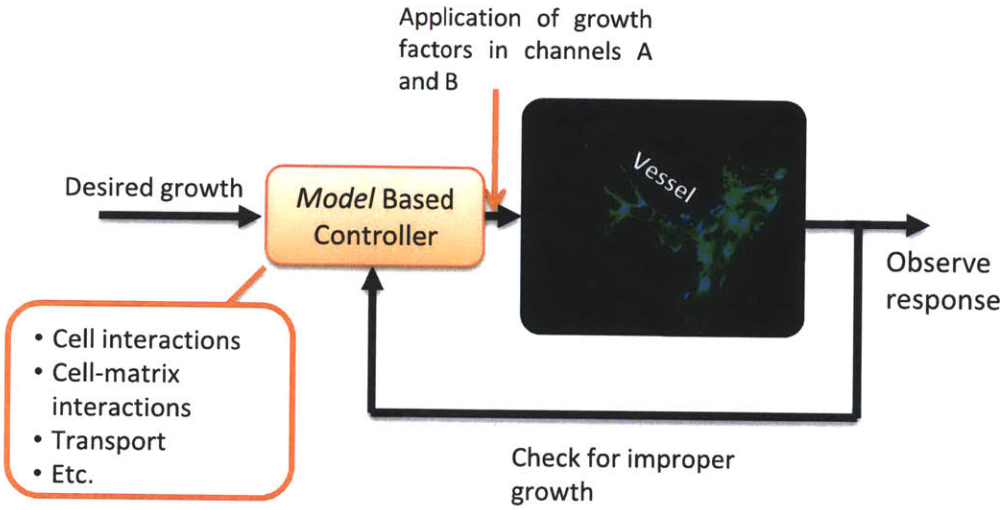

Figure 1-4: Model based feedback control approach used for actively regulating angiogenic growth.

1.4.3 Mathematical Angiogenesis Models

A key aspect of this work will be formulation of quantitative predictive process model to be used for MPC. This means predicting how fast or how large a developing vessel will be in the future given application of growth factors and current conditions. The model needs to be tailored to take measurable and known quantities as inputs and yield quantities related to future sprout development, like diameter, as an output.

A multitude of mathematical models have been proposed to describe different aspects of the angiogenesis process. To list a few, [4] has proposed a stochastic tip cell selection model, [38] has proposed a detailed reaction-diffusion tip cell matrix degradation model, [34, 67, 66] have proposed complex, multiscale models to capture

cell-cell interaction and chemotactic dynamics in a forming sprout, and [64] has proposed a hybrid discrete/continuum model involving random walks. See [51] for an in depth review of some of these models as well many other stochastic and deterministic modeling approaches.

Despite the great mechanistic insights and qualitatively similar results obtained from these models, they are extremely complex with many parameters and many equations, and none has shown significant capability to quantitatively predict any of the behaviors or geometries observed in angiogenesis. Therefore, we will need to formulate a new model designed to quantitatively describe future growth based on current observations and known inputs.

1.4.4 Vascular Growth Metric

A key initial question in understanding how to regulate angiogenesis is: What are the important features to regulate? Do we need to concern ourselves with the positions and internal states of all of the ECs and the ECM, or are bulk measures like vessel diameter and rate of growth sufficient?

To our knowledge, there has been no specific discussion in the literature about which vessel features are important to promote successful growth. However, the mechanisms determining the geometry, e.g., diameter, of nascent vessels are still poorly understood. In fact, recent murine vessel explant studies [57, 59] have observed a wide distribution in the range of 5-25μm during the first 14 days of nascent vessel growth, but there has been no explanation of the mechanisms behind such dramatic sizing variability. In this work, we aim to investigate the mechanisms mediating nascent vessel geometry in precisely regulated microfluidic assays, and describe and verify the mechanisms using a quantitatively predictive mathematical model, which will later be useful for formulating a control framework.

1.5 Contributions of this Thesis

It is clear that understanding how to reliably manipulate and guide angiogenic growth will provide an important advancement in fields as diverse as tissue engineering, wound repair and even cancer inhibition [36].

In this thesis, we take a new approach to regulating vascular growth by integrating quantifiable angiogenesis assays with a quantitative process model and feedback to improve reliability/variance, as illustrated in Fig. 1-5. We use *in vitro* microfluidic as-

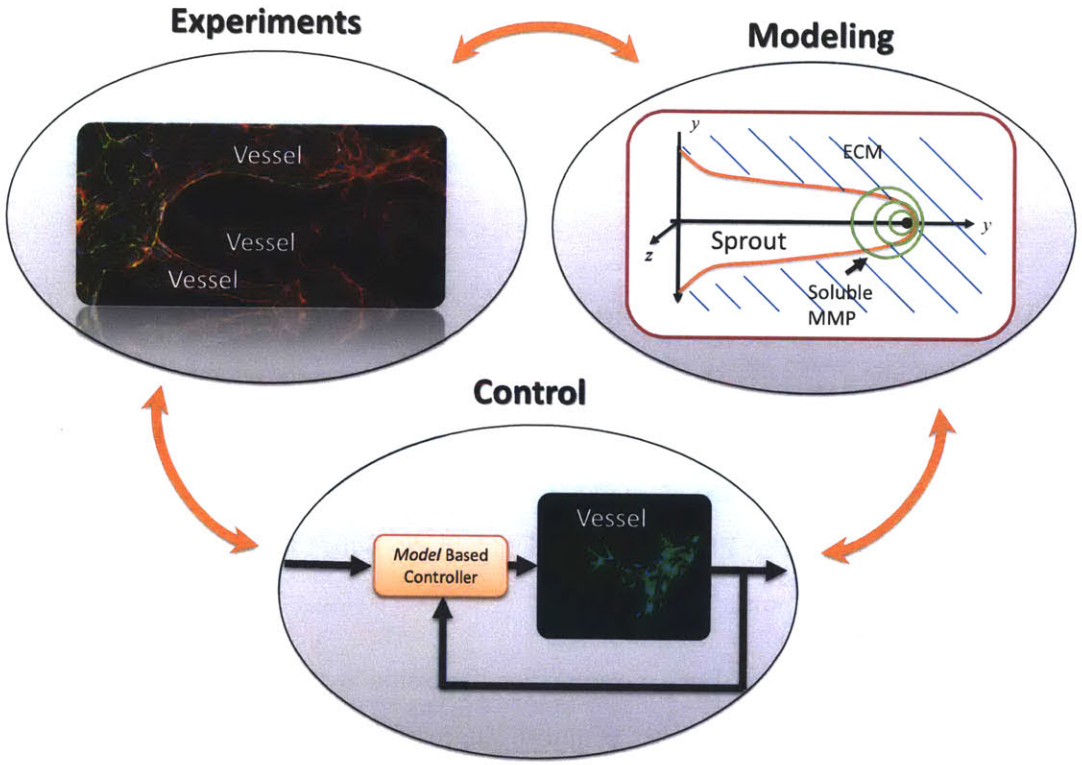

Figure 1-5: This work takes an integrated appraoch by combining experimental observations with quantitative process models to implement feedback.

says with precisely controlled biophysical and biochemical conditions [15], which can be systematically modulated to experimentally study and regulate angiogenic growth. Observed response to applied angiogenic stimuli, such as vascular endothelial growth factor (VEGF), will provide insights necessary for formulating a mathematical process model. The process model will be used to predict future growth based on observed

growth-so-far and applied biophysical conditions, will enable open loop selection of the best input stimuli to obtain desired growth patterns, and will enable active feedback control to regulate incorrect growth. Since angiogenesis is a complex, multi-stage, process [57], I focus on modeling and controlling nascent sprout development after the tip cell is selected, but before branching and maturation occurs. Relatively little is known about this portion of the process, but since later stages of angiogenic development depend on these initial sprouts, understanding their process and how to regulate them may play an important role in learning how to attain successful mature networks.

In the following chapters, we take the following integrated approach to regulating control of angiogenic growth:

- **Quantitative assay development** Present the design of a new microfluidic assay, which is an extension of the design developed by [15]. The new design provides a multitude of angiogenic growth regions subjected to virtually identical biochemical and biophysical conditions, enabling quantitative evaluation of nascent vessel growth despite a high level of variability in the growth of individual vessels.
- **Experimental observation** Employ the new assay design to systematically evaluate growth in response to multiple ∇VEGF conditions and MMP inhibitors. These observations will lead to new understanding of the mechanisms mediating nascent vessel geometry.
- **Computational model formulation** Formulate a quantitative process model with structure based on the experimental observations and parameter tuned to match the data.
- **Controller formulation** Formulate an input vs. time trajectory optimization approach to plan the best sequence of inputs to obtain desired growth and formulate a Model Predictive Control approach to correct for noise in the process response to growth factor inputs.

Taken together, this thesis contributes the first methodology to integrate exper-

imental observations with a quantitative and predictive mathematical model to actively regulate angiogenic growth.

Chapter 2

"High Throughput" Microfluidics [1]

2.1 Need for a High Throughput Angiogenesis Assay

Recent advances in microfluidic assay technologies have demonstrated the ability to produce physiologically relevant three dimensional microenvironments with precise biophysical and biochemical conditions for studying morphological growth, such as in angiogenesis [15]. These devices have enabled systematic study of morphological response to multiple exogenous biophysical and biochemical inputs. However, previous designs suffer from the key limitation that just a few observational instances are available from each assay. In contrast, single cell assays, measured using flow cytometry, can automatically evaluate millions of ensemble observations [9], yielding quantitative and statistical measurements. A similar capability in microfluidic morphology assays would enable us to characterize angiogenic growth in response to multiple growth factors and combinations thereof. In this chapter, we aim to help bridge the capability gap in microfluidic morphology assays by developing a new device design for statistically comparing the angiogenic response to multiple biochemical cues. As we will show in the next chapter, the multitude of data will enable us to find consistent relationships in angiogenic growth that will facilitate predictive modeling and control.

[1] This work was conducted as a collaboration between myself, Waleed Farahat, and Ioannis Zervantonakis. See [25] for further topics on usage of this design.

2.2 High Throughput Assay

2.2.1 Design

The founding motivation for this work came when we attempted to quantify and distinguish angiogenic response to different growth factor stimuli, including conditions with gradient of VEGF (∇VEGF)=0 and ∇VEGF=20ng/mL/(gel region width). Increasing ∇VEGF is known to stimulate chemotactic response in ECs [71]. However, the growth response in the microfluidic devices was highly variable from region to region and from device to device (see Fig. 2-1). We employed numerous metrics, including counting the number of nuclei to invade beyond the monolayer, the total number of sprouts, and attempting to measure the overall length of sprout growth. Regardless of metric, it was difficult to statistically discern morphological differences between the conditions.

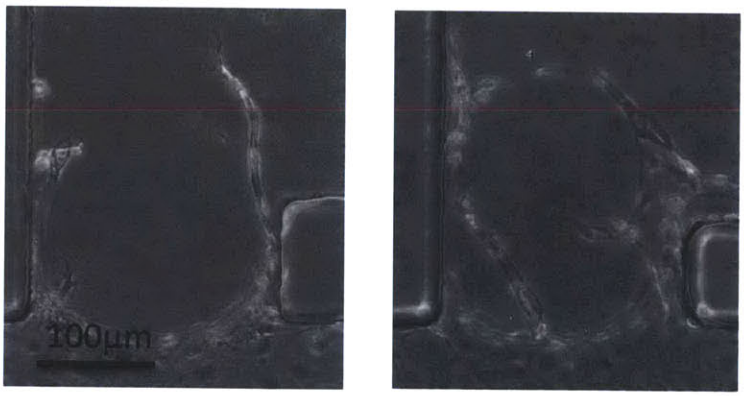

Figure 2-1: Sprouting in two of the microfluidic devices designed in [15] after 72hr of growth. Despite being constructed at the same time and subjected to apparently identical conditions (20ng/mL VEGF in the lower channel and 40ng/mL VEGF in the upper channel), the devices show enormous growth variability, including rate and shape of the elongating vessels.

To improve on these issues, we developed a new microfluidic design that extended the approach described in [15] to incorporate an increased number of cell growth regions, yielding multiple observation instances on a single chip. The new device design (Fig. 2-2A) consists of 2 media channels engulfing an extended, central region containing the extracellular gel matrix. By varying the biochemical conditions in

the channels, growth factor concentrations and gradients across the gel region are established to stimulate cellular responses. Because all of the gel regions are subjected to virtually identical conditions via channels a and b, and they are all filled using a single gel injection through the ports at the end of the gel region, the gel regions should comprise an ensemble of virtually identical experimental repetitions.

Two objectives were sought in the design of the device with respect to gel containment in the central region:

- **Extending the length of the gel region** to enable the formation of a longer monolayer, thereby increasing the number of cell growth regions and their associated observations, and
- **Achieving a uniform gel-fluidic channel interface** since non-uniformities would result in aberrations in the extra-cellular conditions and non-uniform cell seeding.

These two objectives were achieved via post design (Fig. 2-2C). To enable uniform gel interface with channels a and b, trapezoidal shapes were chosen for the posts. The post angle (60°) was chosen to supplement the contact angle of the PDMS surface (measured to be $\sim 120°$) such that the collagen is parallel and flush with the medium channels [32] (see Figs. 2-2C-D).

To extend the length of the gel region, posts were spaced such that the pressure containment capability of the cage was sufficient to withstand filling pressure transients encountered during filling of the gel solution.

Ideally, it is desirable to minimize the presence of the posts (in number and in size) since they diminish the usable length of the device. However, since the posts provide the necessary functionality of gel caging, they need to be sufficiently close to maintain sufficient pressure containment capability.

To maximize pressure containment in the gel cage, we analyzed factors driving surface tension at the air-liquid interface. The pressure drop across the air-liquid interface is given by [44]

$$\Delta P = \gamma \left(\frac{1}{R_x} + \frac{1}{R_z} \right) \tag{2.1}$$

where P is the pressure differential sustained by surface tension, γ is the surface tension coefficient, and R_x and R_z are the radii of curvature of the air-liquid interface in two mutually perpendicular directions (shown in Fig. 2-2B). In conjunction with the contact angle between PDMS and gel solution, R_x is determined by post spacing, whereas R_z is determined by channel height. An interface that is robust to spillage during the filling process is one that can withstand large pressure perturbations P. Thus, to maximize P, two steps were taken: first, devices were baked during fabrication (see Appendix A.1) to render the PDMS hydrophobic [77], which allowed for the formation of interfaces with smaller radii of curvature. Second, the radius of curvature R_x, was chosen via empirical testing of various post spacings to provide the necessary P that allowed the gel to be filled through the length of the gel region without spilling into channels a or b. The radius of curvature R_z was not subject to optimization since it was determined by channel height, and was constrained by the desire to maintain three-dimensionality of the cell culture. Furthermore, the converging geometry of the trapezoidal posts helped stabilize the air-gel interface since it results in narrower radius R_x as more gel is filled in the device. Thus, the geometry provided a stiffening interface that helped arrest perturbations that may have occurred during the manual gel filling process.

2.2.2 Transport Validation

To validate growth factor transport dynamics, we used Texas Red-conjugated Dextran (40 kDa) as an analog for biological growth factors such as VEGF-165 (38 kDa). By imaging the fluorescence intensity, diffusion profiles are attained (Fig. 2-3A-B). These characterizations were conducted when flow was drawn through the device at 1 μL/min via a perfusion pump (Harvard Apparatus). Under flow conditions, the device developed nearly linear gradients that can be sustained for extended durations (>6hr measurement duration). The concentration profiles in the outermost gel regions nearest to the gel filling ports were affected by the large mass of gel at the ports that acted as a sink. This resulted in reduced gradients in the first and last 2 to 3 gel growth regions in the device. We have noted a significantly reduced (50-75%) reduction of

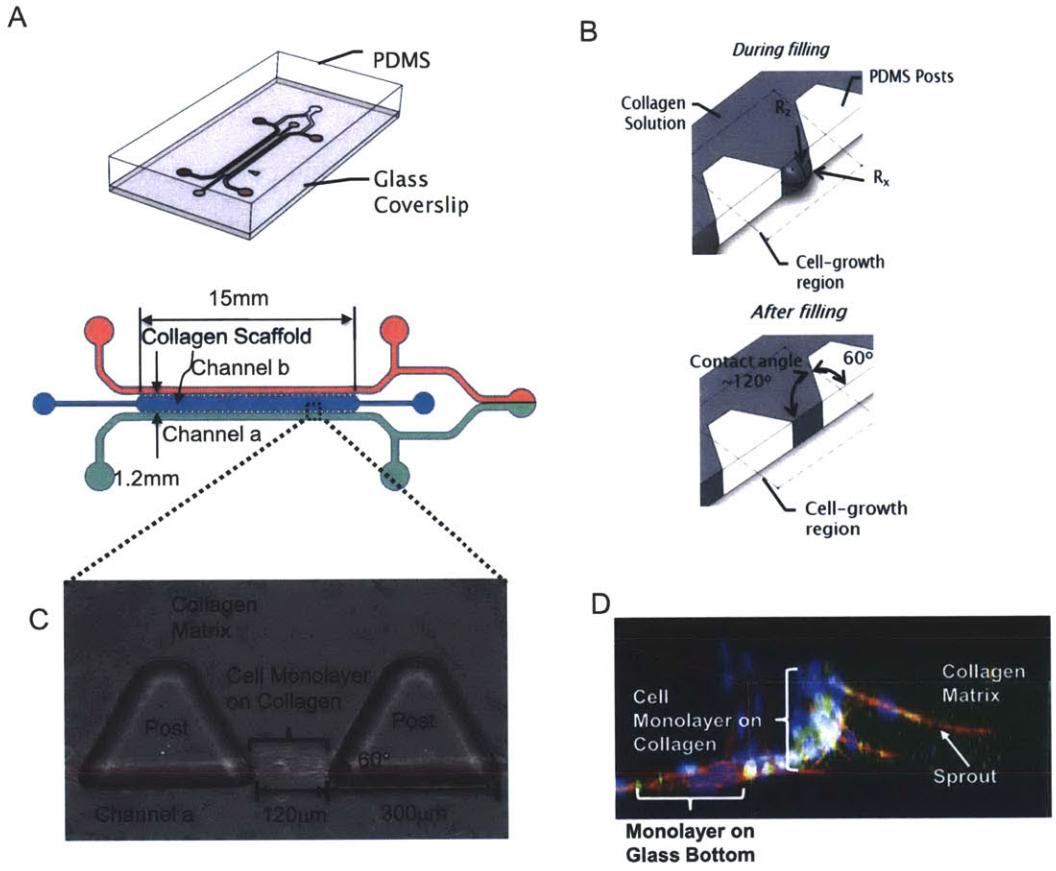

Figure 2-2: "High throughput" microfluidic device design. (A) The device is constructed from a PDMS substrate fabricated using standard soft lithographic techniques [77] and bonded to a glass coverslip (see Appendix A.1). The device consists of a central 3D collagen gel matrix with a fluidic media channel on either side. The gel channel is bounded by trapezoidal support posts leaving 37 separated growth regions along its length. The collagen matrix and channels are 120μ m deep. (B) The device contains an array of trapezoidal posts that cage collagen gel into well-defined regions with uniform surface interface. During collagen filling, the gel solution-air interface curvature sustains transient filling pressures. The posts have an angle of 60°, supplementary to the contact angle of the liquid collagen and hydrophobic PDMS surface (measured to be 120°). Post spacing is 100-125 μm, and width of gel region is 1.3mm. (C) Phase contrast image of trapezoidal posts bounding collagen-channel interface after 72hr of cell growth from monolayer in channel a into collagen matrix. (D) Side view confocal image of ECs built up on the collagen wall and sprouting into the collagen matrix. Blue: Dapi. Red: Cytosolic CellTracker CMMRA. Green: DQ quenched collagen.

sprouting incidence in the outer 2 regions, and the sprouts that do grow are typically stunted.

While we validated transport in this microfluidic design using flow, all of the cell growth experiments in this thesis were conducted without flow. Instead the "Y-junction" on the right side of Fig. 2-2A was blocked by injecting collagen. Channel medium was replaced every 24hr, meaning that the gradient decays with time. From previous work, we expect the gradient to decay with a time constant ~60min [80].

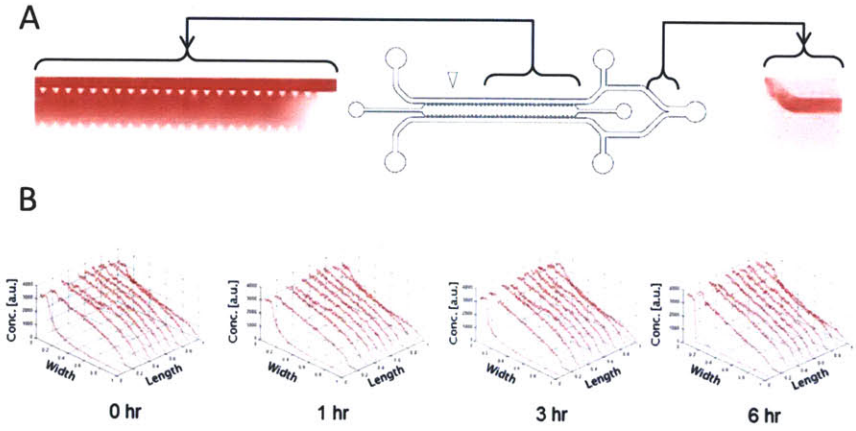

Figure 2-3: Characterization of device transport characteristics in the absence of monolayers. Characterization was conducted using Texas Red conjugated 40 kDa Dextran in lieu of VEGF (molecular weight38kDa) (A) Gradients are estimated via fluorescent intensity measurements along the entire gel region (B) The generation gradients that are stable in time when device is under flow of 1 μL/min. Gradients are shown to be stable over 6hr.

2.3 Illustration of High Throughput Data

With this high throughput design, we expected to be able to quantify and statistically distinguish the influence of multiple biochemical conditions on angiogenic growth. One metric of interest that we first used for evaluating growth is the rate of new sprout growth in response to multiple biochemical factors. We wanted to check whether we could influence the rate of growth using different applications of VEGF and sphingosine-1-phosphate (S1P). The former is well known to illicit angiogenic

growth, while the latter is known to illicit a highly invasive phenotype in ECs [20].

We seeded ECs into into channel a of the high throughput design (see Appendix A.2 for details of cell loading). The cells build up on the collagen wall and sprout into the collagen matrix during the next several days (see Fig. 2-2D). The experiment began 24hr after cell loading (referred to as day 1). We considered three different conditions in channels [a,b]: i) complete EGM-2MV minus VEGF (referred to as basal) in both channels, ii) basal plus [20ng/mL VEGF, 40ng/mL VEGF], and iii)basal plus [20ng/mL VEGF, 40ng/mL VEGF + 250nM S1P]. We use $n = 3$ devices per condition for a total of $N = 111$ growth regions. We then counted the number of new sprouts that has grown in each region by comparing phase contrast images from both days.

As shown in Figs. 2-4A-C, we were able to get different number of new sprouts depending on the conditions. However observing the individual instances in Figs. 2-4A-C alone is insufficient to fully understand the distribution of each response. (see Fig. 2-4D). As shown, our large number of observations for each condition were able to define three completely different growth distributions ($P < 0.01$ between each pair of conditions).

2.4 Summary and Utility

Our high throughput design enables us to quantify the sprouting response to multiple combinations of growth factors in terms of a statistical distribution. As in the previous section, this gives us the ability to learn how growth factors and interventions manipulate angiogenic growth. As we will illustrate in the next chapter, observation of so many growth regions gives us the additional capability to look for low variance relationships in the data. These relationships will lead to formulation of a quantitative and predictive model that can be used for control.

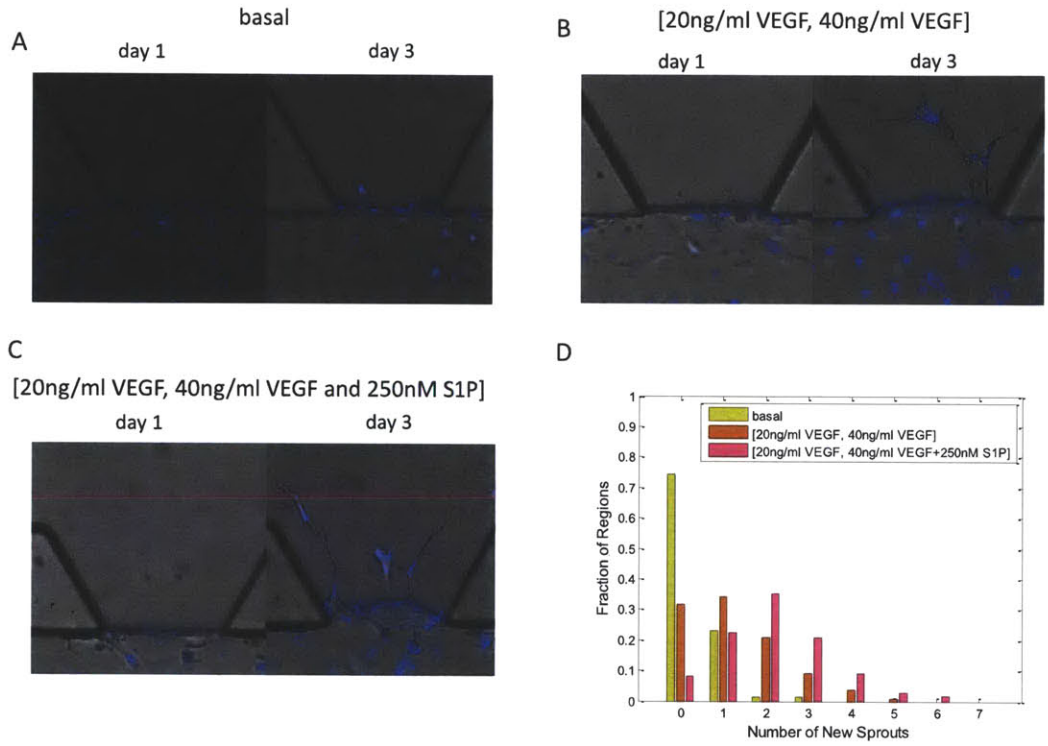

Figure 2-4: Number of new sprouts grown over 48hrs from each of three conditions: (A) complete EGM-2MV minus VEGF (referred to as basal; see Appendix A.2) in both channels, (B) basal plus [20ng/mL VEGF, 40ng/mL VEGF], and (C) basal plus[20ng/mL VEGF, 40ng/mL VEGF + 250nM S1P]. (D) The instances shown in (A) - (C) are representative but they do not illustrate the overall distribution shown.

Chapter 3

Experimental Evaluation and Quantitative Model Formulation

3.1 Introduction

Vascular network growth in angiogenesis is initiated when tip cells are selected from endothelial cells (ECs) in pre-existing vasculature in response to biochemical factors, such as vascular endothelial growth factor (VEGF) [27, 29]. The tip cells proteolyze extracellular matrix (ECM), of which type I collagen is the main structural constituent [8], enabling them to chemotactically migrate and leaving a cleaved conduit behind them in the ECM [14, 73]. Endothelial stalk cells migrate and proliferate in this conduit behind the tip cell to form the stalk of the new vasculature [36].

Many aspects of nascent vessel elongation have been heavily studied, including tip cell selection [37, 49, 69], collagen proteolysis [38], and tip and stalk cell migration [46]. However, the mechanisms determining the geometry, e.g., diameter, of nascent vessels are still poorly understood. In fact, recent murine vessel explant studies [57, 59] have observed a wide distribution in the range of 5-25μm during the first 14 days of nascent vessel growth, but there has been no explanation of the mechanisms behind such dramatic sizing variability. In this work, we aim to investigate the mechanisms behind nascent vessel growth in precisely regulated microfluidic assays and verify the mechanisms using a quantitatively predictive mathematical model.

Angiogenic sprout growth and conduit formation have been shown to depend on matrix metalloproteinase (MMP) mediated remodeling of the collagen extracellular matrix [14, 73], making MMPs key candidates for explaining observed conduit and sprout geometries. There are several important MMP species involved in degradation of type I collagen, including the cell-membrane bound species, membrane type 1 (MT1)-MMP (MMP14) [14], as well as the soluble species MMP1 (collagenase I) [70] and MMP2 (gelatinase A) [33]. In addition MMP2 and MMP9 (gelatinase B) both proteolyze type IV collagen [54], which ECs secrete to form a basement membrane while cleaving the ECM [35, 51].

Quantitatively predicting nascent vessel geometry requires understanding of the spatial distribution of MMP secretion and activation in addition to which species play a dominant role in matrix remodeling. MT1-MMP is known to be activated prior to secretion and has shown to be essential for vascular growth in murine retina models, but whether it is expressed solely at the tip cell or distributed along the sprout has been a key question [56, 73, 79]. Furthermore, MT1-MMP is involved in the MMP2/MMP9 activation cascade [75], meaning that the proteoytic forms of MMP2 and MMP9 co-localize with MT1-MMP. Finally, MMP1 is activated by MMP3 (stromelysin-1) and MMP10 (stromelysin-2), neither of which proteolyze triple helix fibers in type I collagen [55, 62, 70]. To our knowledge, MMP1 localization has not been studied.

In this chapter, we investigate the mechanisms determining nascent sprout diameter by combining a microfluidic angiogenesis model with a computational MMP-collagen reaction-diffusion simulation. The microfluidic model involves vessel growth into a 3D type I collagen scaffold from a primary microvascular endothelial cell monolayer [15, 25]. This assay enables precise manipulation of biophysical and biochemical conditions, including application of MMP inhibitors, while eliminating many of the poorly understood and unmeasured interactions involved in in vivo assays. Simultaneously, the computational simulation supports the experimentally observed mechanisms and serves as a tool to analyze experimental data. We will use the model to formulate our control framework in Chapter 4.

3.2 Results

3.2.1 Diameter is Inversely Correlated with Elongation Speed

We first tested whether we could produce a range of nascent vessel diameters in our microfluidic angiogenesis model, similar to what has been observed in *in vivo* murine studies [57, 59]. In a microfluidic device shown in Figs. 2-2A, 2-2C, a collagen gel scaffold was created between the two microfluidic channels, a and b, and different concentrations of Vascular Endothelial Growth Factor (VEGF) were applied to both channels to create a gradient of VEGF concentration across the gel scaffold. Human microvascular endothelial cells (hMVEC) were seeded into one channel (channel a), formed a confluent monolayer on the vertical wall of the gel scaffold, and sprouted out towards the higher VEGF concentration (Fig. 2-2D). The 3D growth of sprouts into the collagen scaffold was observed, and their elongation speed and the sprout diameter were measured. Different combinations of VEGF concentration and gradient resulted in diverse speed and diameter distributions, as shown in Fig. 3-1B. Comparing faster and slower elongating vessels, slower vessels had wider diameters (Fig. 3-1A). Interestingly, comparing multiple experiments, with different VEGF concentrations applied in channels a and b, and therefore gradients across the gel region, showed that all of the vessel speeds and diameters fell on a single curve (Fig. 3-1B)[1].

3.2.2 Diameter vs. Speed Curve is Consistent with Tip Cell Localized Soluble MMP Activation

We sought to understand and explain the mechanisms relating speed and diameter in Fig. 3-1B. Since vessel growth is dependent on matrix remodeling, we considered the important MMP species involved in proteolysis of types I and IV collagen (see Fig. 3-2). These include the cell membrane bound MT1-MMP, as well as the soluble species MMP1, MMP2, and MMP9 [54]. The soluble species are secreted from the cell as

[1]To give an idea of how consistent a typical sprout geometry is along its length, Experiment 2) yielded a total of approximately 82 sprouts, and only 5 (about 6%) satisfied our criterion.

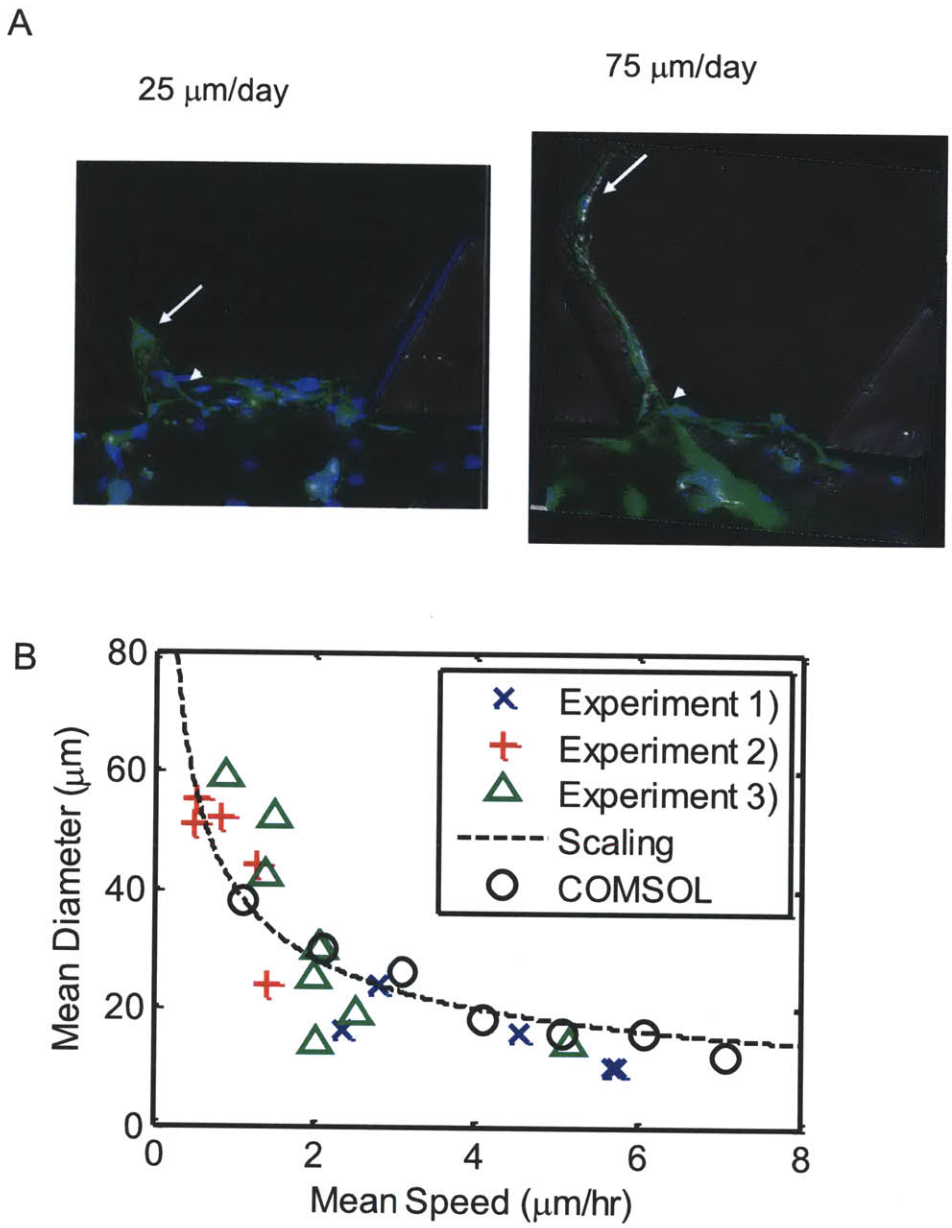

Figure 3-1: Vessel diameter is correlated with elongation speed. (A) Live cell stained confocal images showing a thick, slow growing lumen developing at 25μm/day and a narrow, faster growing lumen developing at 75μm/day. Green: CellTracker CMFDA. Blue: Live nuclear stain Hoechst 33342. Arrows: vessel tip cell nuclei. Arrow heads: vessel stalks connected to monolayer. (B) Diameter vs. elongation rate from experimental measurements, scaling analysis, and COMSOL. Experimental measurements are taken from nascent vessels grown over 3-9 days with less than 20% variation in cross sectional diameter over their length. Channel [a, b] conditions were either [20ng/mL VEGF, 40ng/mL VEGF] in experiments 1) and 3) or [30ng/mL VEGF, 60ng/mL VEGF] in experiment 2). The scaling analysis was given by Eq. 3.2 with $a = 39.8$. The simulation was conducted in COMSOL according to Eqs. 3.3-3.4 and used parameter values from Table 1.

the latent proenzymes proMMP1, proMMP2, and proMMP9, and are activated via a cleaving process that exposes their own proteolytic domains. MT1-MMP is known to be the key activator of proMMP2 [33] while MMP2 and MMP3 are important activators of proMMP9 [75]. In addition proMMP1 is known to be activated by MMP3 and MMP10 [70]. Finally, membrane bound plasmin is known to activate MMP1, MMP3, and MMP9 [53]. Furthermore, 3D human umbilical endothelial cell cultures showed that MT1-MMP expression is localized to the tip cell in the presence of mural smooth muscle cells (SMCs), but may be distributed along the vessel without SMCs [79].

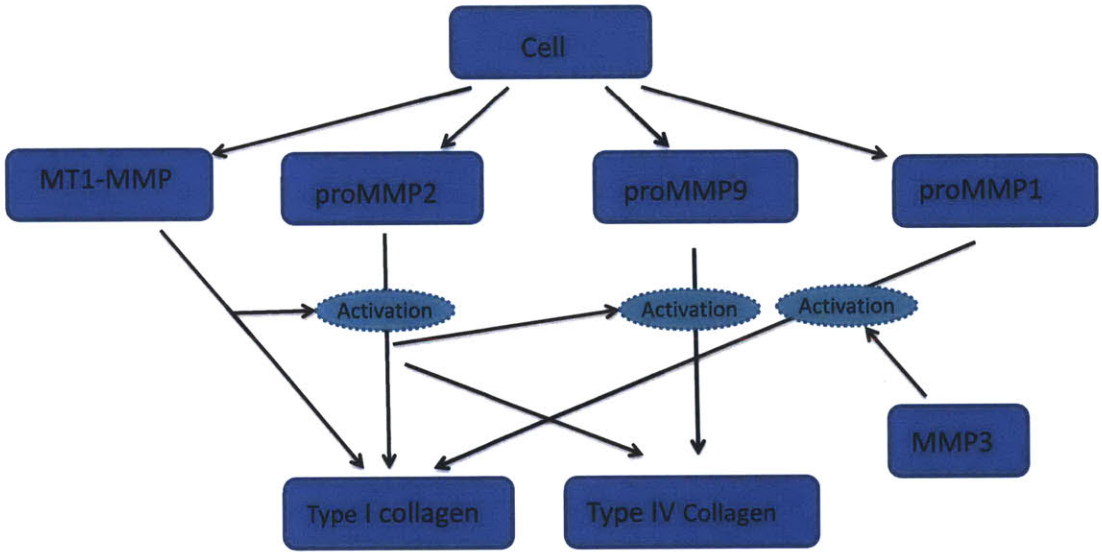

Figure 3-2: Hierarchy of MMP secretion, activation and reaction with ECM components types I and IV collagen.

Because of the many MMPs and overall complexity involved in proMMP activation and localization, we conducted a basic analysis to understand how vessel diameter would scale with elongation rate, assuming that activated soluble MMP species are localized to the tip cell. Suppose that a tip cell elongates at a constant speed v along a straight line while producing activated soluble MMPs at a constant rate $\dot{Q}_{source}$. Over time T the cell produces $\dot{Q}_{source}T$ of soluble MMPs and proteolyses the collagen gel to create a conduit. This total amount of proteolyzed collagen scales as the amount of activated MMP produced. Therefore, if the initial collagen concentration is c_0, and

the final volume of the vessel is V,

$$c_0 V \sim \dot{Q}_{source} T \tag{3.1}$$

Furthermore, assuming a symmetric distribution of the degraded collagen about the straight line of the tip cell motion, the conduit can be approximated to a cylinder with diameter D_c, which yields the following scaling relationship:

$$D_c \sim \sqrt{1/v} \tag{3.2}$$

Fitting $D_c = a\sqrt{1/v}$, with a as a parameter, to the data in Fig. 3-1B yields $a = 40.0\text{m}^{3/2}\text{s}^{-1/2}$ with a correlation coefficient of $R^2 = 0.87$ between the scaling curve and the experiment data. Thus, the experimental observations are consistent with a mechanism involving soluble MMPs produced and activated locally at the tip cell.

3.2.3 Inhibition of MMP2 Reduces Vessel Diameters

We next used several specific soluble MMP inhibitors commercially available from Calbiochem to ascertain which species play a significant role in mediating vessel diameter. Previous knockout studies in mouse retina models have shown that MMP2 and MMP9 are not as important as MT1-MMP in mediating vascular network growth [14], but vessel diameters were not analyzed. Therefore, we used three inhibitors from Calbiochem to probe the influence of the soluble species on diameter: i) MMP2/MMP9 Inhibitor I (MMP2/9i), which primarily acts on MMP2 (IC50=310nM) and MMP9 (IC50=240nM), but also inhibits MMP3 (IC50=1μM), ii) MMP9 Inhibitor I (MMP9i), which primarily inhibits MMP9 (IC50=5nM), and iii) MMP Inhibitor I (MMP1i), which primarily acts on MMP1 (IC50=1μM) and MMP8 (IC50=1μM).

We applied [30ng/mL, 40ng/mL] of VEGF in a total of 12 microfluidic devices to be used for four conditions in triplicate. The conditions were: Control of [30ng/mL, 40ng/mL] VEGF only, and each of the inhibitors i)-iii) applied in both channels a and

b, with the VEGF. Fig. 3-3 shows a typical typical vessel from each of the conditions, while Fig 3-5 shows a statistical analysis of the measurements.

Of the three inhibited conditions, only MMP2/9i showed a significant diametric change relative to Control (Figs. 3-5A-B). The MMP2/9i also showed both reduced diameter and elongation speed compared with the scaling analysis (Fig. 3-4), indicating that the total amount of cleaved collagen was reduced. Furthermore, all three soluble MMP inhibited conditions showed no significant change in incidence of sprouting relative to the Control (Fig. 3-5C). Taken together, these results suggest that MMP1 and MMP9 do not play a significant role in determining vessel diameter. In addition, MMP2 does play a significant role in mediating diameter, but is not essential for vessel invasiveness, as found in [14].

As an additional control, we applied the pan-MMP inhibitor GM6001, which has been reported to inhibit angiogenic invasiveness, possibly due to MT1-MMP inhibition [73]. It similarly inhibited angiogenic sprouting in our microfluidic angiogenesis model (see Fig. 3-6). This result suggests that vessel invasiveness is MMP mediated even though it is not dependent on the soluble species, MMP1, MMP2, or MMP9.

3.2.4 MT1-MMP Expression is Tip Cell Localized in the Nascent Vessel

Since MT1-MMP is widely considered to be a key activator of MMP2 [10, 18, 40], we investigated MT1-MMP expression and localization using immunofluorescent staining in nascent vessels after 72hr of growth. We found that elongating vessels led by tip cells having active filopodia consistently stained positive for tip cell localized MT1-MMP (Fig. 3-7A), while vessels without apparent filopodia did not stain positive (Fig. 3-7B). Active tip cells also stained positive for MT1-MMP in the presence of the MMP2/MMP9 inhibitor (Fig. 3-7C), verifying that the inhibitor does not act on MT1-MMP. These results suggest that active tip cells featured by extensive filopodia express MT1-MMP, and that MMP2 activation via MT1-MMP is therefore localized at the tip cell.

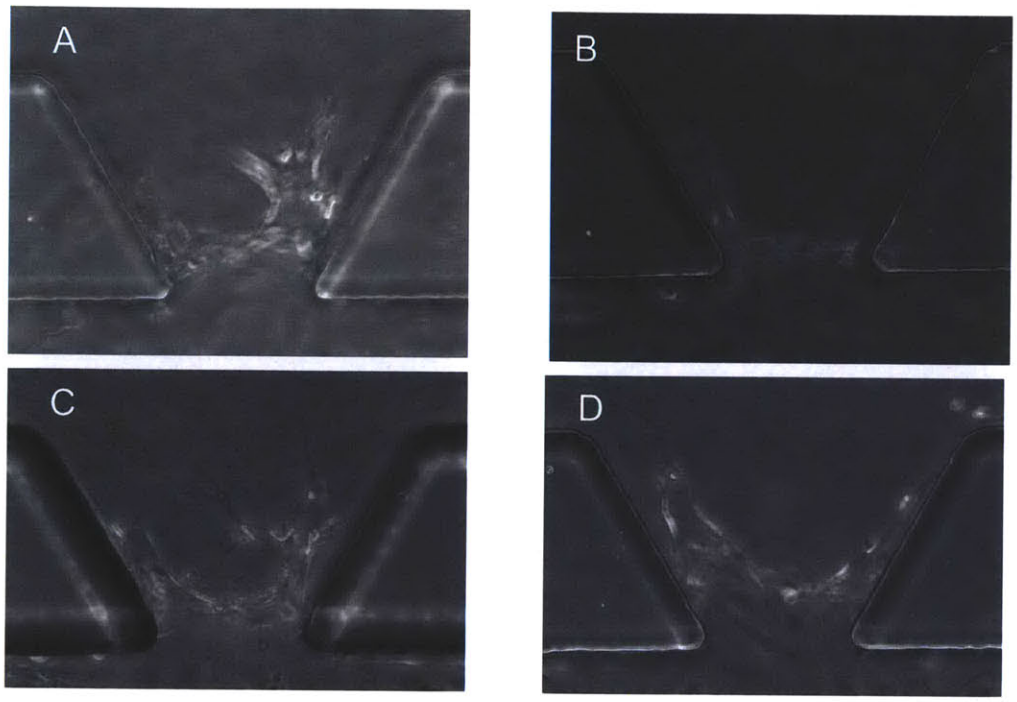

Figure 3-3: Influence of MMP inhibitors on sprout diameter with channel conditions [30ng/mL VEGF, 40ng/mL VEGF] over 72hr. (A) Phase contrast image of representative vessel from control. (B) Representative vessel with 1μM MMP2/9i. (C) Representative vessel with 1μM MMP9i. (D) Representative vessel with 10 μM MMP1i.

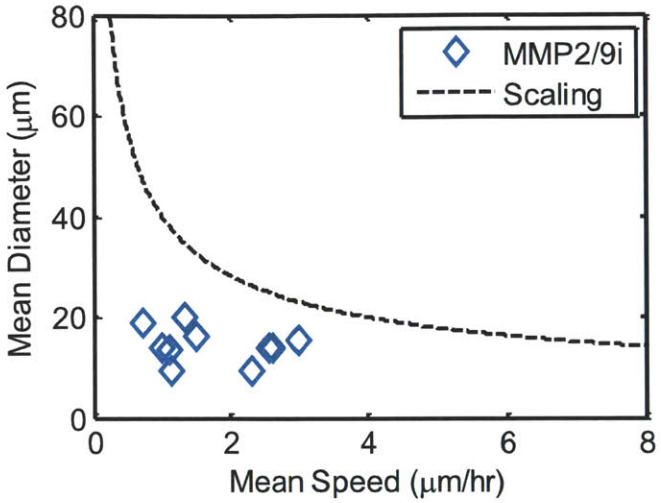

Figure 3-4: Diameter vs. speed measurements from 10 sprouts in the MMP2/9i condition compared against the scaling curve given by Eq. 3.2.

3.2.5 Dynamic Reaction-Diffusion Model Predicts Vessels Geometry

The scaling analysis and the experimental data in Fig. 3-1 delineated the sprout diameter-speed relationship, but it applies only to steady state tip cell migration where a long cylindrical vessel with a constant diameter is produced. However, time lapse observations show that nascent vessels have variability in the elongation rate and direction. Therefore, we have constructed a simple mathematical reaction-diffusion model to validate our hypothesized mechanism in terms of the variable sprouting behavior.

The MMP inhibition and MT1-MMP staining studies suggest that sprout diameter is widened by MMP2, which is activated by MT1-MMP at the sprout tip. The mathematical model was constructed based on these results with two key mechanisms: a) soluble MMPs are produced/activated locally at a tip cell, and b) the activated soluble MMPs diffuse into the collagen gel, degrade the gel, and widen the conduit.

Let $\mathbf{x}^{tip}(t)$ be the coordinates of a tip cell location at time t. Since the soluble MMPs are produced and activated only at the tip cell location, the MMP reaction-diffusion process can be described by the following reaction-diffusion equation .

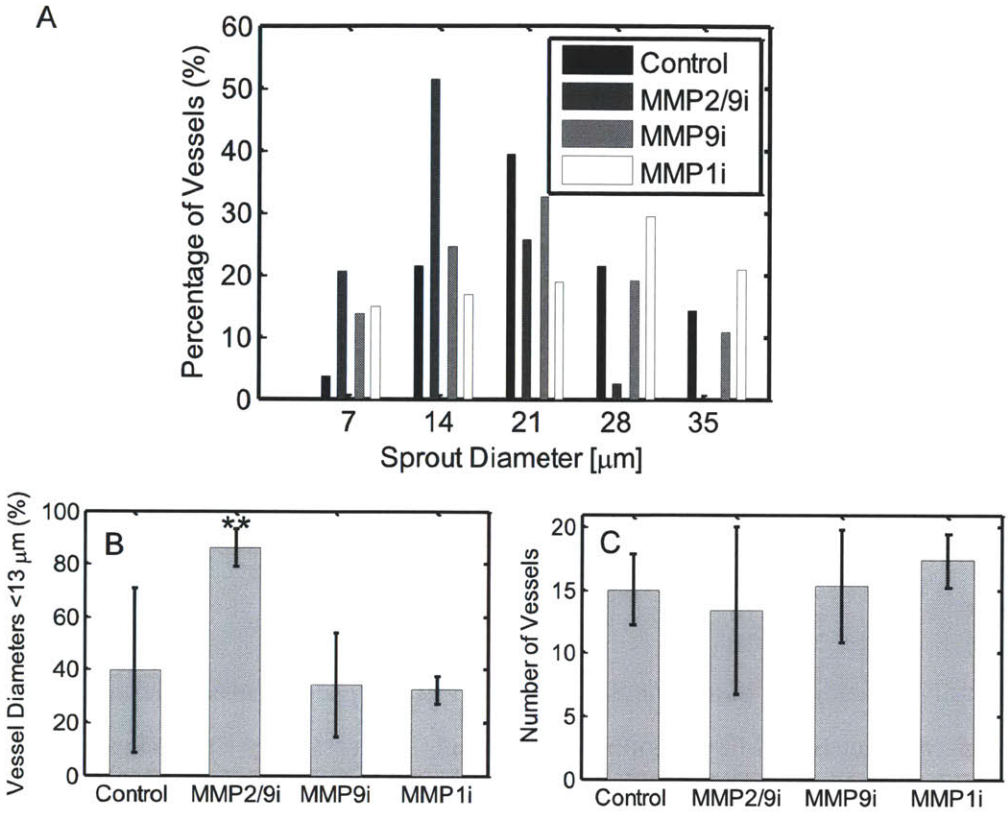

Figure 3-5: Quantification of inhibitor influence on vessel diameter. (A) Histogram of all nascent vessel diameters measured after 72hr of growth for Control and each of the soluble MMP inhibitors. MMP2/9i shows a marked reduction in mean diameter and a reduction in variance of the distribution.(B) Percentage of measured vessels below 13μm for each condition. Measurements were taken from phase contrast images of all clearly defined vessels from 37 gel regions per device. Clearly defined vessels consist of a clear leading tip connected to the monolayer via vessel stalk. $N = 3$ devices for each condition. Only MMP2/9i yielded a significant change in vessel diameters (mean $\pm$ SD, $^{**}P < 0.01$ compared with Control). (C) Number of measured vessels for each condition after 72hr or growth (mean $\pm$ SD).

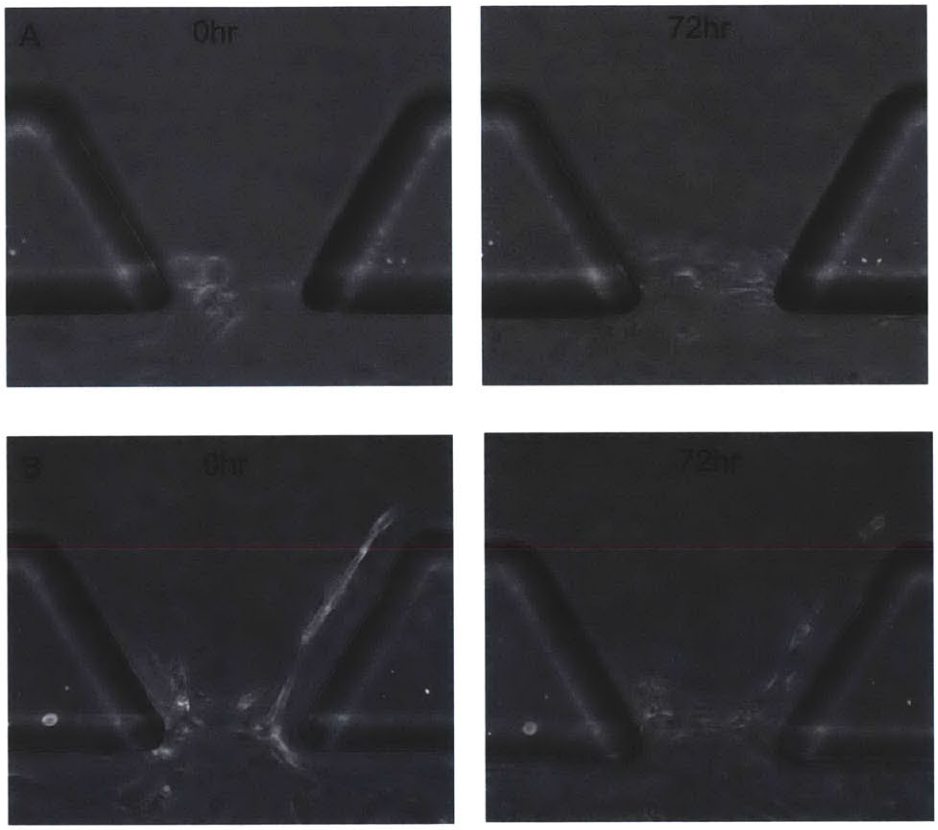

Figure 3-6: Nascent vessel response to 1μM pan-MMP inhibitor GM6001. (A) In stark contrast to inhibition of soluble species alone, pan-MMP inhibition lead to no vessel extension in any growth region that did not already have an existing tip cell. (B) Pan-MMP inhibition applied at 0hr in growth regions that had pre-existing nascent vessels halted vessel elongation.

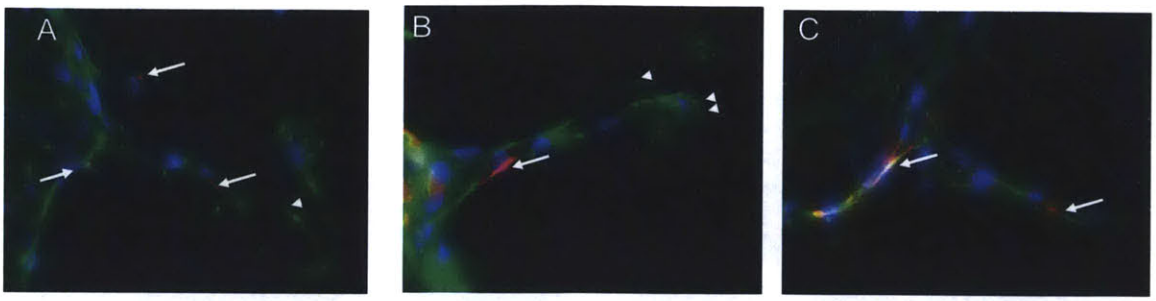

Figure 3-7: Immunofluorescent staining for MT1-MMP of sprouts growing in 2.5mg/ml type I collagen gel. Blue: DAPI. Green: Phalloidin. Red: MT1-MMP. (A) Channel conditions of [30ng/mL VEGF, 40ng/mL VEGF] with leading cell showing apparent filopodia (arrow head) characteristic of tip cell phenotype, and expressing MT1-MMP (arrows). (B) Channel conditions of [30ng/mL VEGF, 40 ng/mL VEGF] with leading cell (double arrow head) showing no apparent filopodia and expressing no MT1-MMP. Trailing cell shows filopodia extension (arrow head) and expresses MT1-MMP. (C) Channel conditions of [30ng/mL VEGF, 40ng/mL VEGF] + 1μM MMP2/9i in both channels. MT1-MMP expression is maintained despite MMP2/9i.

$$\frac{\partial q(\mathbf{x},t)}{\partial t} = D\nabla^2 q(\mathbf{x},t) - k_q c(\mathbf{x},t) q(\mathbf{x},t) + \dot{q}_{source}\left(\mathbf{x}^{tip}(t)\right) \tag{3.3}$$

where $q(\mathbf{x},t)$ is the soluble MMP concentration at position $\mathbf{x}$ and time t, $c(\mathbf{x},t)$ is the collagen concentration, D is the MMP diffusion coefficient, k_q is second order MMP loss rate constant due to reaction with collagen, and $\dot{q}_{source}$ is a fixed MMP production rate at the tip cell location and zero elsewhere. The production rate is computed as $\dot{q}_{source}\left(\mathbf{x}^{tip}(t)\right) = \dot{Q}_{source}/V_{cell}$ where $\dot{Q}_{source}$ is MMP production rate in units of (mol/s) and V_{cell} is the cell volume. In response to the diffusion of soluble MMP into the gel, collagen loss is given by

$$\frac{\partial c(\mathbf{x},t)}{\partial t} = -k_c c(\mathbf{x},t) q(\mathbf{x},t) \tag{3.4}$$

where k_c is the second order collagen proteolysis rate constant. We used published values from the literature for D, k_q, $\dot{Q}_{source}$ (Table 3.1), and tuned only k_c using the data in Fig. 3-1B. To tune k_c, we note that over long periods of time T with constant tip cell speed, the total amount of collagen lost and the total amount of MMP produced, $\dot{Q}_{source}T$ should be consumed in the same period of time. Therefore,

Table 3.1: List of simulation parameter values and their sources.

Parameter	Reported Value	Used Value	Source
Initial collagen concentration, c_0	—	2.5mg/mL	Experimental value used in the microfluidic assay.
Diffusion Coefficient, D	$0.85 \times 10^{-6}\text{cm}^2\text{s}^{-1}$	$0.85 \times 10^{-6}\text{cm}^2\text{s}^{-1}$	Activated MMP2 diffusion coefficient [38, 6].
MMP rate constant, k_q	$1.2 \times 10^5\text{M}^{-1}\text{s}^{-1}$ – $1.4 \times 10^6\text{M}^{-1}\text{s}^{-1}$	$1.2 \times 10^6\text{M}^{-1}\text{s}^{-1}$	Enzymatic efficiencies reported for multiple MMP2 species binding with type IV collagen [52].
Collagen rate constant, k_c	—	$8.0 \times 10^5\text{M}^{-1}\text{s}^{-1}$	Tuned parameter to match the data.
MMP source, $\dot{Q}_{source}$	0 – 180,000 molecules/hr	180,000 molecules/hr	No measurements available for MMP2, but speculated to be similar to MT1-MMP production rate in [38].

their characteristic loss rates must be equal:

$$k_c \dot{Q}_{source} T = k_q c_0 V \tag{3.5}$$

from which we estimated k_c such that the simulated diameter vs. speed curve matched the experimental data and scaling analysis in Fig. 3-1B (Table 3.1). The simulated vessel boundary was taken at $c(\mathbf{x}, t_f) < 0.15 c_0$.

This dynamic model, built upon the hypothesized mechanism, was validated against experimental data. First, the 2D tip position was measured every three days using phase contrast imaging (Figs. 3-8A-B). Next, the spatial tip cell trajectory was taken to be the 3D centerline of the sprout, which was measured from end-point confocal images (Fig. 3-8C). Finally, the full spatiotemporal tip cell trajectory is estimated by linearly interpolating between the phase contrast data to determine the time profile over which the tip cell traversed the centerline. The full spatiotemporal tip cell trajectory, $\mathbf{x}^{tip}(t)$ is used as an input to Eq. 3.3.

We computationally implemented the PDE reaction-diffusion model Eqs. 3.3-3.4 in COMSOL using the full 3D geometry of the microfluidic device and $\mathbf{x}^{tip}(t)$ as an

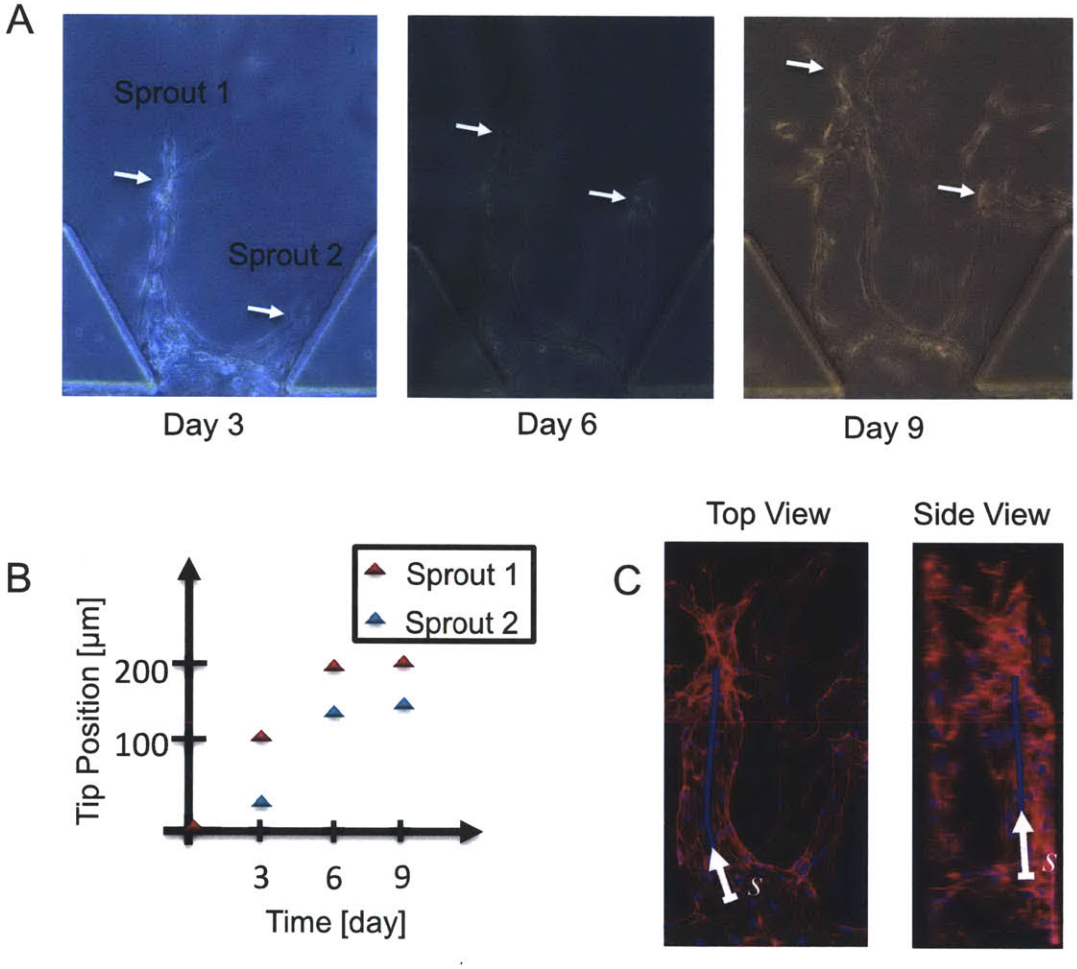

Figure 3-8: Illustration of experimental data analysis for input to the computational model. (A) Phase contrast images yield approximate tip cell locations (arrows) at 3 day intervals for the duration of growth. (B) Tip cell vertical position versus time for both sprouts, as estimated from the phase contrast images. Sprout 2 lost its tip cell phenotype and stopped migrating between day 6 and day 9. (C) Maximum intensity projection top and side views of endpoint confocal image. Stains are: Rhodamine Phalloidin (red) and Dapi (blue). Estimated centerline of sprout 1 (blue line) is taken as estimated tip cell migration trajectory. The tip position information from (B), combined with the estimated migration trajectory in (C) are used as inputs to the quantitative model. The arclength coordinate, s is used for quantitatively evaluating the simulation fit to the data using Eqs. 3.6-3.7.

Table 3.1: List of simulation parameter values and their sources.

Parameter	Reported Value	Used Value	Source
Initial collagen concentration, c_0	—	2.5mg/mL	Experimental value used in the microfluidic assay.
Diffusion Coefficient, D	$0.85 \times 10^{-6}\text{cm}^2\text{s}^{-1}$	$0.85 \times 10^{-6}\text{cm}^2\text{s}^{-1}$	Activated MMP2 diffusion coefficient [38, 6].
MMP rate constant, k_q	$1.2 \times 10^5\text{M}^{-1}\text{s}^{-1}$ – $1.4 \times 10^6\text{M}^{-1}\text{s}^{-1}$	$1.2 \times 10^6\text{M}^{-1}\text{s}^{-1}$	Enzymatic efficiencies reported for multiple MMP2 species binding with type IV collagen [52].
Collagen rate constant, k_c	—	$8.0 \times 10^5\text{M}^{-1}\text{s}^{-1}$	Tuned parameter to match the data.
MMP source, $\dot{Q}_{source}$	0 – 180,000 molecules/hr	180,000 molecules/hr	No measurements available for MMP2, but speculated to be similar to MT1-MMP production rate in [38].

their characteristic loss rates must be equal:

$$k_c \dot{Q}_{source} T = k_q c_0 V \tag{3.5}$$

from which we estimated k_c such that the simulated diameter vs. speed curve matched the experimental data and scaling analysis in Fig. 3-1B (Table 3.1). The simulated vessel boundary was taken at $c(\mathbf{x}, t_f) < 0.15 c_0$.

This dynamic model, built upon the hypothesized mechanism, was validated against experimental data. First, the 2D tip position was measured every three days using phase contrast imaging (Figs. 3-8A-B). Next, the spatial tip cell trajectory was taken to be the 3D centerline of the sprout, which was measured from end-point confocal images (Fig. 3-8C). Finally, the full spatiotemporal tip cell trajectory is estimated by linearly interpolating between the phase contrast data to determine the time profile over which the tip cell traversed the centerline. The full spatiotemporal tip cell trajectory, $\mathbf{x}^{tip}(t)$ is used as an input to Eq. 3.3.

We computationally implemented the PDE reaction-diffusion model Eqs. 3.3-3.4 in COMSOL using the full 3D geometry of the microfluidic device and $\mathbf{x}^{tip}(t)$ as an

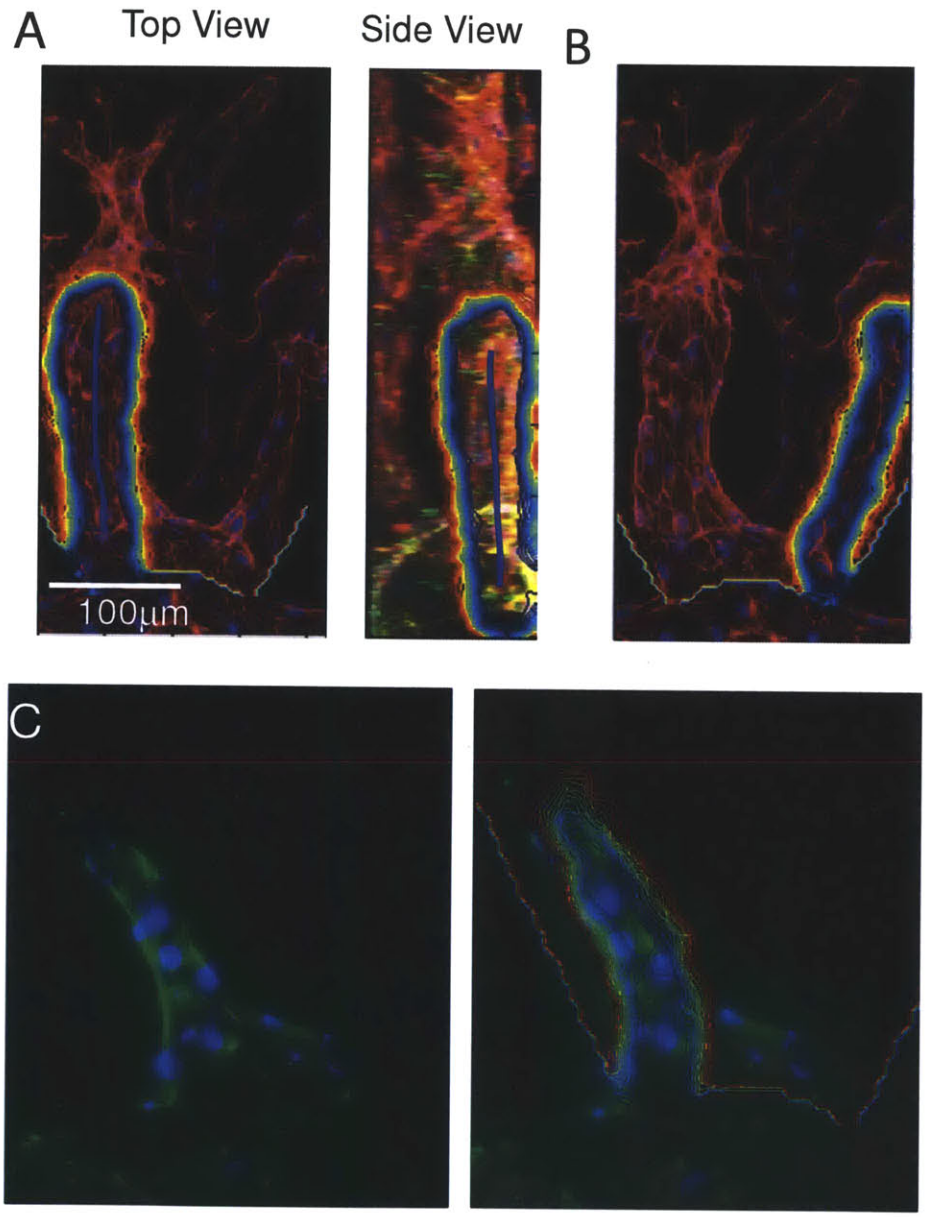

Figure 3-9: Simulated sprout growth based on quantitative model overlaid on experimental confocal images. Contour lines indicate constant collagen concentration and define the sprout boundary. (A) Simulation of Sprout 1 from Fig. 3-8 using published parameter values, as indicated in Table 3.1. (B) Simulation of faster growing Sprout 2 from Fig. 3-8 using the same parameter values. (C) Endpoint image of 72hr sprout growth from a different experiment (left). Green: Phalloidin. Blue: Dapi. Simulation using the parameter values from Table 3.1 superimposed on sprout.

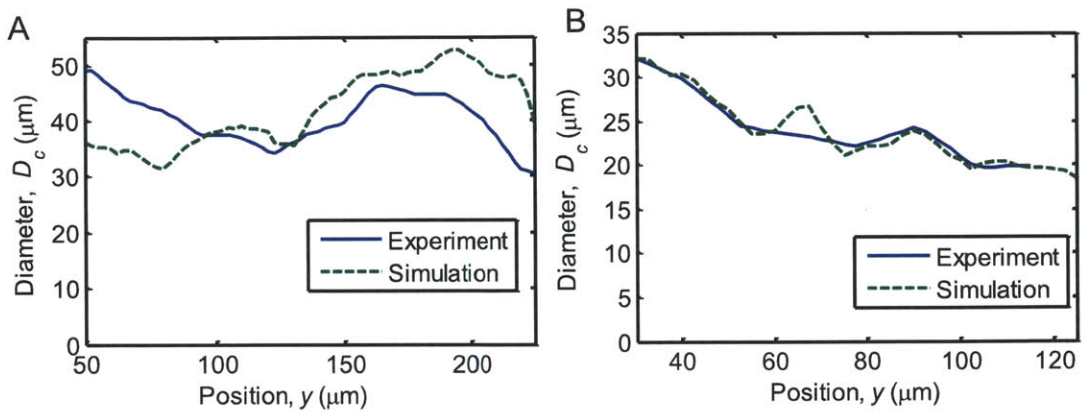

Figure 3-10: Comparison of simulated and experimental cross section diameter vs. vertical position y. (A) Comparison for Sprout 1. (B) Comparison for Sprout 3.

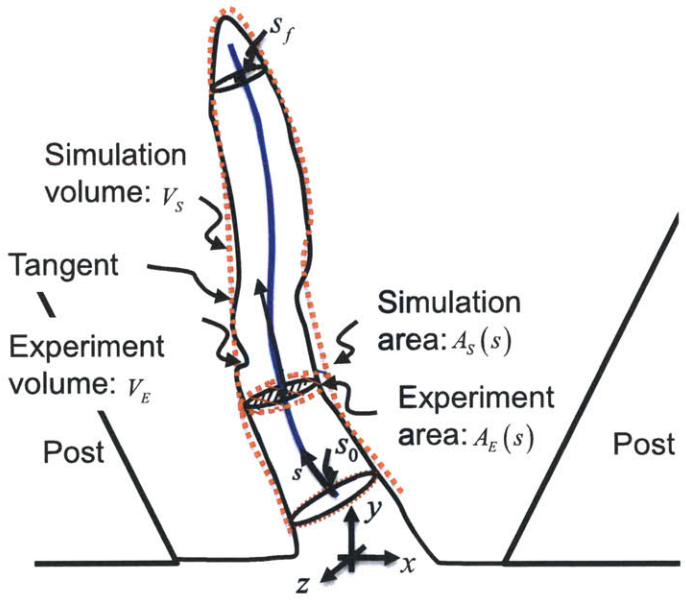

Figure 3-11: Illustration of quantitative comparison between simulation and experiment. The centerline of the final experimental volume is used as the simulated tip cell trajectory. The error between simulation and experiment is computed in terms of both total volume and average error in cross sectional area. The cross sectional area is taken as the area in the plane that is locally perpendicular to the centerline curve, s. Volume and area are analyzed between the planes at s_0 and s_f to eliminate boundary errors due to unobserved MMP production as the tip cell is beginning to invade the gel and unrealized proteolysis at the tip due to endpoint fixation.

Table 3.2: Simulation vs. experiment error metrics. Values are averaged across 5 sprouts.

Metric	Mean	Min	Max
Volume error, ε_V	11%	1%	20%
Ave. area error, ε_A	13%	9%	25%

wheres_0 and s_f are chosen to eliminate measurement ambiguity at the base and tip of the vessel. We evaluated the error of a total of 5 nascent vessels, yielding the results in Table 3.2.

3.3 Discussion

Prior work has considered many aspects of nascent vessel development, including the tip cell selection process, tip cell migration, the influence of collagen degradation, and stalk cell migration and proliferation [27, 29, 8, 73, 14, 36, 4], but has not addressed the mechanisms that determine nascent vessel diameter. In this study, we combined experimental evidence in 3D microfluidic assays with a computational model to support the hypothesis that soluble MMP2 activated at the tip cell plays a dominant role in degrading collagen to determine sprout geometry and diameter. The microfluidic assays provided a platform for observing the spatiotemporal profile of the sprouting process in response to multiple growth conditions and interventions while maintaining the biological relevance of 3D migration and conduit formation [15]. Furthermore, the simple computational model supported the hypothesis by matching the experimental data, despite the multitude of less significant factors that may be involved, e.g., a multitude of MMP species [54], TIMPS [38], plasmin [53], among others.

The vessel diameters observed in control experiments were substantially larger than that of a tip cell (as large as 40μm; Fig. 3-5), suggesting that the vessel conduit may be formed not only by membrane bound MT1-MMP on the tip cell that directly cleaves the collagen gel, but also by other mechanisms. Only the MMP2/9 inhibitor yielded a significant change in conduit diameters relative to Control (Fig. 3-5). Furthermore, vessels grown subjected to the MMP2/9 inhibitor stained posi-

tive for MT1-MMP (Fig. 3-7C), indicating that MT1-MMP alone is insufficient to generate large conduit diameters. These results also imply that MMP9 and MMP1 don not play a significant role. The apparently limited role of MMP1 is somewhat unexpected since MMP1 is known to degrade type I collagen with similar efficacy to MMP2 [62]. One explanation may be that, while MMP1 is capable of proteolyzing the collagen triple helices into 1/4 and 3/4 segments, it does not solubilize the remaining matrix components. In contrast, MMP2 proteolyzes the collagen triple helices and solubilizes all matrix components in type I collagen [62]. That MMP9 plays a less significant role is less surprising since it is capable of preoteolyzing type IV, but not type I collagen, which is the primary ECM component, both in our in vitro model and in vivo [8].

Since the rate of vessel formation was not influenced by MMP2/9i (Fig. 3-5C), sprouting may be MT1-MMP mediated in our microfluidic model and is consistent with previous work in mouse retina models [14]. We also found that application of the pan-MMP inhibitor GM6001, which inhibits MT1-MMP in addition to the relevant soluble species, entirely inhibited new vessel sprouting and stopped elongation of existing nascent vessels (Fig. 3-6). These results are also consistent with previous work [73]. Taken together, our MMP inhibition studies strongly suggest that conduit geometry is mediated by expression of soluble MMP2, but that vessel elongation depends on other species including MT1-MMP.

Immunofluorescent staining for MT1-MMP showed localization in the sprout to tip cells with active filopodia (see Fig. 3-7A), but tip cells without apparent filopodia often do not stain positive for MT1-MMP (see Fig. 3-7B). The latter result is consistent with a vessel that is quiescent and is no longer cleaving the matrix. However, since we must fix the vessel to check for MT1-MMP, it is not possible to determine whether additional matrix remodeling would have occurred. Note that some non-tip cells do express MT1-MMP within the cell monolayer (Fig. 3-7), but we have not observed MT1-MMP expression within the sprout stalk after the 72hr duration of our experiments. We speculate that the MT1-MMP expressing cells within the monolayer may be consistent with cells that are stochastically differentiating to the

tip cell phenotype. This follows from previous work showing that delta like ligand 4/notch signaling is known to inhibit tip cell phenotypic differentiation in the vicinity of an existing tip cell [4, 63], and a recent finding that MT1-MMP expression is up regulated by notch [28]. Since proMMP2 is enzymatically activated by MT1-MMP, tip cell localized MT1-MMP expression in the nascent vessel implies that activated MMP2 is sourced from the vessel tip.

The scaling analysis and experimental data in Fig. 3-1 are valid only for steady state tip cell migration that produces a nascent vessel having a uniform diameter along a long longitudinal axis. We measured the diameter and length of each nascent vessel, took only the vessels with approximately constant diameter, and estimated their average elongation speed to obtain a correlation between speed and diameter at steady state. We took measurements from multiple experiments with different cell batches, and VEGF concentrations and gradients (see Fig 3-1B). Each experiment having 37 sprouting sites shows a range of vessel growth rates despite all sprouts being exposed to similar biophysical and biochemical conditions. In order to explore a wider range of speeds, we applied different concentration and gradients of VEGF.

Interestingly, while the data were obtained from diverse experiments under different conditions, they all lie on a single curve relating vessel diameter to tip cell velocity$D_c \sim v^{-1/2}$. The curve is consistent with the steady state scaling analysis of the degraded collagen gel cleaved by tip cell localized soluble MMPs produced at a constant rate while the tip cell moves at a constant speed.

While the scaling analysis explains the relationship between elongation speed and vessel diameter for tip cells migrating at a constant speed, many experimental data show that both tip cell speed and direction vary over a broad range during nascent sprout formation. The dynamic reaction-diffusion model is applicable to broader experimental data with varying tip cell speed and direction. This elucidates the spatiotemporal profile of sprouting vessels in relation to the varying tip cell velocity and diffusion of soluble MMPs. The reaction-diffusion model with only four parameters fitted very well the spatiotemporal profile of varying vessel diameter obtained experimentally. The model was built based on the key hypothesis: the soluble MMPs

locally activated at a tip cell are responsible for widening the vessel diameter. The agreement with broad experimental data substantiates this hypothesis.

The full mechanism regulating proteolysis of type I collagen includes the interactions of the several essential MMP species discussed so far, both with each other and with the matrix, as well as multiple species of tissue inhibitor of metalloproteinases (TIMPs), which are both MMP agonists and involved in activation of proMMP2 [11]. Furthermore, though MT1-MMP is often cited as the most important proMMP2 activator, plasmin mediates the process [53] and other MT-MMPs, including MT2, 3, and 5-MMP, are known to be involved in proMMP2 activation [21]. Since the experimental data suggest that diameter regulation is MMP2 mediated, but a host of factors may be involved in proMMP2 activation, we supported our hypothesis that active soluble MMP is tip cell localized by implementing a reaction diffusion model that is consistent with the hypothesis and verified it against experimental data.

Due to the complexity of the total proteolytic reaction, some previous work has attempted to construct a mechanistically accurate model of the preteolytic activation and reaction cascade, including MT1-MMP, MMP2, and TIMP2 [38]. However, the process is very complex and the model included 14 equations and more than 30 parameters. While accurate, this model has never been matched with experimental data. Our objective was to formulate a model that included just a few parameters that are tuned to one data set and illustrate that the mechanism holds across a wide collection of experiments. Inspired by the mechanistically complete work in [38], we formulated a simple tip cell localized soluble MMP reaction-diffusion model involving just two equations and a total of 4 parameters. By utilizing the experimentally observed spatiotemporal profile of tip cell position as an input, and assuming constant soluble MMP production rate, we were able to tune the parameters to fit a single sprout, and then showed that the tuned model predicted other experimentally observed sprout geometries from the same, and from other, experiments. Furthermore, the model was able to predict not only sprouts with constant diameter, but also sprouts with non-uniform diameter and speed.

3.4 Summary

In this chapter we took a coupled approach to investigating and quantitatively describing the relationship between nascent vessel geometry and sprout elongation rate by combining biochemical assays with a quantitatively tuned computational model. We have illustrated that the model can be used to reliably predict experimentally observed geometries from our experimental platform without needing to re-tune the parameters for every experiment.

As we will show in the next chapter, this quantitative model will enable us to predict the time profile of input speeds necessary to optimize vessel geometry. Furthermore, it will enable implementation of a feedback loop to actively compensate for input and process noise.

Chapter 4

Synthesis of Condition Time Profile and Feedback Control

The long term goal of this thesis is to establish a framework for regulating the nascent sprouting process to generate desired sprout geometries. The quantitative model developed in section 3.2.5 is instrumental for synthesizing the time profile of input conditions to yield a desired geometry, and for implementing feedback control. However, there are several important issues that remain to be addressed (see Fig. 4-1):

- **Understanding how to use the PDE model to determine the the optimal time profile of tip cell speed, $v^{tip}(t)$.** The system dynamics are spatially distributed. Manipulating speed while the tip cell is at one location affects the conduit shape at the tip cell location *and* its surroundings, meaning that the optimal time profile is not trivially obtained.

- **Determining whether we well we can control tip cell speed by applying growth factors in channels a and b.** The relationship between growth factor stimulus, such as ∇VEGF, and chemotactic response is an open research question without an effective quantitative model, and is outside of the scope of this thesis. We will show that we have limited influence over speed, and that the response is highly variable, so we characterize its variability.

- **A computationally efficient model to evaluate the influence of noisy**

$v^{tip}(t)$ **on the terminal sprout geometry.** The computational model requires $\sim$ 1min in COMSOL to evaluate 24hr of sprout growth. $\sim$ 100's of simulations are required to find the optimal $v^{tip}(t)$, and that number squared are required to evaluate the optimal inputs in the face of $v^{tip}(t)$. Therefore, we pose a much simpler ODE representation for a sprout elongating in a straight line.

- **Implementation of feedback control to compensate for noisy** $v^{tip}(t)$**.** Since since the input is very noisy, we implement a feedback loop in simulation to actively make corrections for incorrect growth. We find that with experimentally observed variance, the controller can make only limited improvement. However, if the variance can be reduced in the future, the controller will prove important in regulating final geometry.

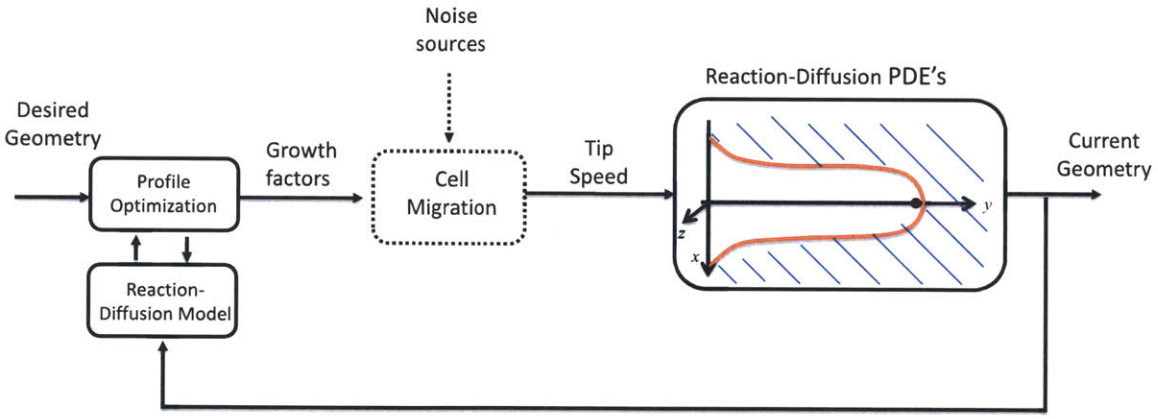

Figure 4-1: Complete formulation for feedback control requires our computational model, a model relating tip cell response to growth factor inputs, and input trajectory optimization. The model relating tip cell response to growth factor inputs is currently an open research question and outside of the scope of this thesis. Therefore, in this work we characterize it and assume that we can directly manipulate tip speed with noise.

4.1 Trajectory Planning

4.1.1 Time Profile Planning

The model developed in section 3.2.5 quantitatively describes the spatiotemporally distributed nature of the reaction-diffusion dynamics. The model enables us to plan how best to manipulate elongation rate, $v^{tip}(t)$, to obtain desired vessel geometric profiles (see Fig. 4-2). However, because of the distributed influence of the tip cell produced MMP2 on its surroundings, we need to take into account not only its influence on the local cross section in the conduit, but also how it will influence the conduit in front and behind of its current location as well as how its future speeds will affect the distributed vessel geometry.

In this section, we implement input trajectory optimization using the PDE model assuming that we can directly control tip cell speed without noise. We will address the issue of noise in the following sections.

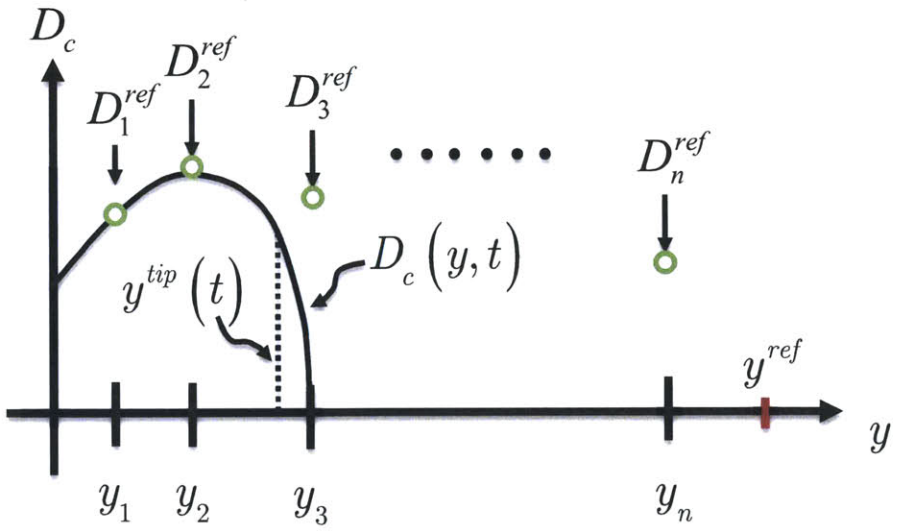

Figure 4-2: Illustration of current diametric time profile, $D_c(y,t)$, compared with desired diametric profile, $D_{ref}(y)$ of the nascent vessel at time t_f. y^{ref} is the desired terminal tip position, $y^{tip}(t_f)$.

We can formulate the open loop trajectory optimization problem as follows. To

begin, we define our state vector to be composed of the quantities we want to control

$$\mathbf{X}(t) = \begin{Bmatrix} y^{tip}(t) \\ D_1(t) \\ \vdots \\ D_n(t) \end{Bmatrix} \tag{4.1}$$

where $D_1(t) \cdots D_n(t)$ are the current diameters at the positions $y_1 \cdots y_n$. In addition, we define a reference vector

$$\mathbf{r} = \begin{Bmatrix} y^{ref} \\ D_1^{ref} \\ \vdots \\ D_n^{ref} \end{Bmatrix} \tag{4.2}$$

from which we can define an error state $\tilde{\mathbf{X}}(t) \equiv \mathbf{X}(t) - \mathbf{r}$.

Assume that the tip cell takes on some time profile of velocity, $v(t)$. Then the states take on nonlinear dynamics according to the PDEs and $v(t)$ (see Fig. 4-1):

$$\dot{\tilde{\mathbf{X}}}(t) = \mathbf{f}\left(\tilde{\mathbf{X}}(t), v(t)\right) \tag{4.3}$$

For the present development, we assume that we take $v(t)$ to be our control input subject to the constraint $0 < v(t) < v_{max}$ and can only change the input at discrete intervals $v(t) = v_i, iT_s < t \leq (i+1)T_s < t_f$ where T_s is the controller sampling period and $i \in \{\mathbb{N}^0 | i \leqslant m\}$ with $m = \lfloor t_f / T_s \rfloor$.

Using this formulation, we can choose an optimal control input policy to minimize terminal error state. Define $\mathbf{v} = [v_1 \cdots v_m]^T$. Then assign a cost function in terms of the terminal error

$$J(\mathbf{v}) = \tilde{\mathbf{X}}^T(t_f) Q \tilde{\mathbf{X}}(t_f) \tag{4.4}$$

where $\mathbf{Q}$ is a $(n+1) \times (n+1)$ weighting matrix that can be used to weight the importance of some final error states more than others. Based on this cost function,

we can choose a sequence of optimal inputs such that

$$\mathbf{v}^{\mathbf{opt}} = \underset{\mathbf{v}\epsilon\mathfrak{V}}{\operatorname{argmin}} \quad \mathbf{J}(\mathbf{v}) \tag{4.5}$$

where $\mathfrak{V} = \{v_i | 0 < v_i < v_{max}\}$.

4.1.2 Input Optimization Approach

Evaluating the cost in Eq. 4.4 given an input sequence $\mathbf{v}$ requires solving the reaction diffusion equations, which we solve numerically in COMSOL. Therefore, an analytic approach to optimizing Eq. 4.5 is not tractable. Instead, we employ MATLAB's `fmincon` numerical optimization package using the active set algorithm obtain the optimal input sequence, $\mathbf{v}^{\mathbf{opt}}$.

The active set algorithm recasts our constrained optimization ($\mathbf{v}\epsilon\mathfrak{V}$) as an unconstrained problem and relies on the local gradient and Hessian of the cost function with respect to the input sequence to descend the cost function toward a local optimality, as shown in Fig. 4-3. Optimization speed is dramatically increased in algorithms utilizing analytic expression for the gradient and Hessian. However, analytic expressions for terminal cost are not feasibly evaluated from the 3D reaction-diffusion equations, so `fmincon` numerically estimates these quantities numerically, using the Broyden-Fletcher-Goldfarb-Shanno(BFGS) method to compute the Hessian [26].

We implemented the input sequence optimization in simulation using MATLAB, and COMSOL with LiveLink for MATLAB. See MATLAB code in Appendix A.6. The simulation was implemented using a radial symmetric geometry using a maximum mesh edge size of 3μm, and using the parameters from Table 3.1. To limit computation time, we take $t_f = 24$hr. While the time constant of cellular response to application of ∇VEGF has not been characterized, we assume that we have direct control over the tip speed, $v(t)$ and take $T_s = 6$hr. Therefore, $m = 4$.

To illustrate the trajectory optimization, we aim to optimize the terminal conduit diameters at $y = 25, 50, 75,$ and 100μm to the terminal reference, $\mathbf{r} = [y^{ref} \quad 20\mu\text{m} \quad 20\mu\text{m} \quad 10\mu\text{m} \quad 10\mu\text{m}]^T$. Note that we have not defined a value for y^{ref} because

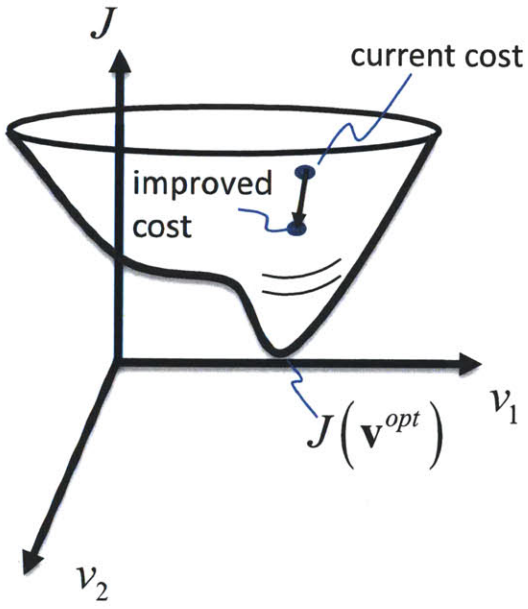

Figure 4-3: Active set algorithm descends cost surface using locally computed gradient and Hessian.

we are not interested in its final value. To eliminate it from the optimization, we set $Q = I_{n+1,n+1}$ except for $Q_{1,1} = 0$. Finally, we take $v^{max} = 12\mu$m.

Fig. 4-4 shows the final diameter profile using the optimal input sequence $\mathbf{v}^{opt}$ obtained from the COMSOL simulation at $t_f = 24$hr. The terminal root-mean-squared error between the simulation and the desired values is approximately 1.6μm. Fig. 4-5 illustrates the time profile of the input and the evolution of the states $\boldsymbol{X}(t)$.

At first glance, it appears that the terminal diametric profile obtained in Fig. 4-4, may not be optimal. It appears that if we increase the v_1 and v_2, we should be able to reduce the error in $D_1(t_f)$ and $D_2(t_f)$. Fig. 4-6, shows the resultant terminal diameter profile with increased v_1 and v_2. As we can see can see, the error in $D_1(t_f)$ and $D_2(t_f)$ is reduced. However, in elevating v_1 and v_2 by less than 0.5μm/hr, we pushed the tip cell much closer to y_3 by the end of the third control interval ($i = 3$). In doing so, $D_3(t_f)$ is considerably widened due to the proximity of the slow moving cell, and increases the total mean squared error. Therefore, the original optimal solution is better.

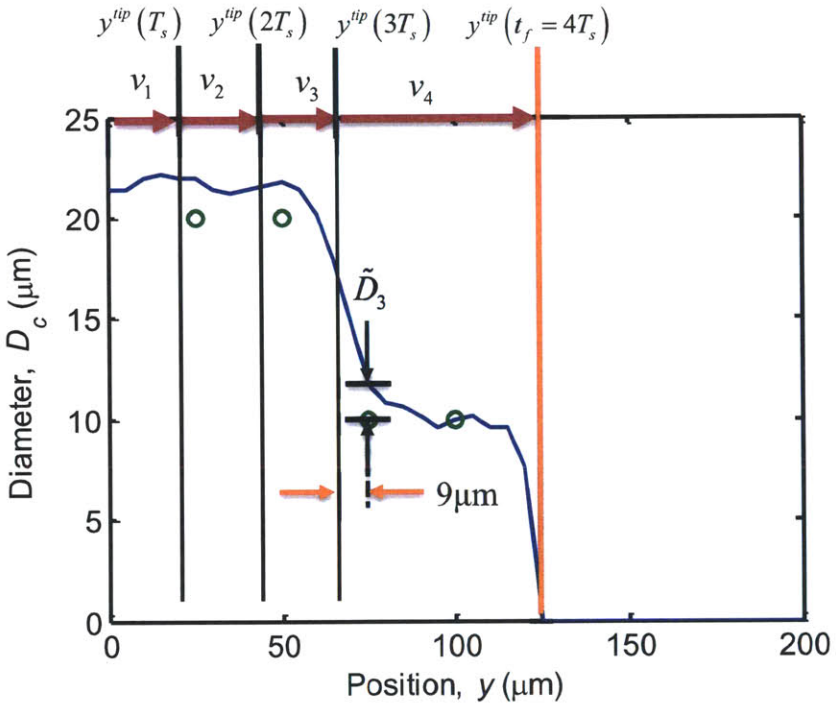

Figure 4-4: Final conduit profile $D_c(y, t_f)$ using optimal input sequence, $\mathbf{v}^{opt}$ (line), compared with reference diameters, D_i^{ref} (circles). Vertical lines indicate the tip cell location $y^{tip}(iT_s)$ and the arrows at the top indicate the speeds, v_i used during the i^{th} time interval.

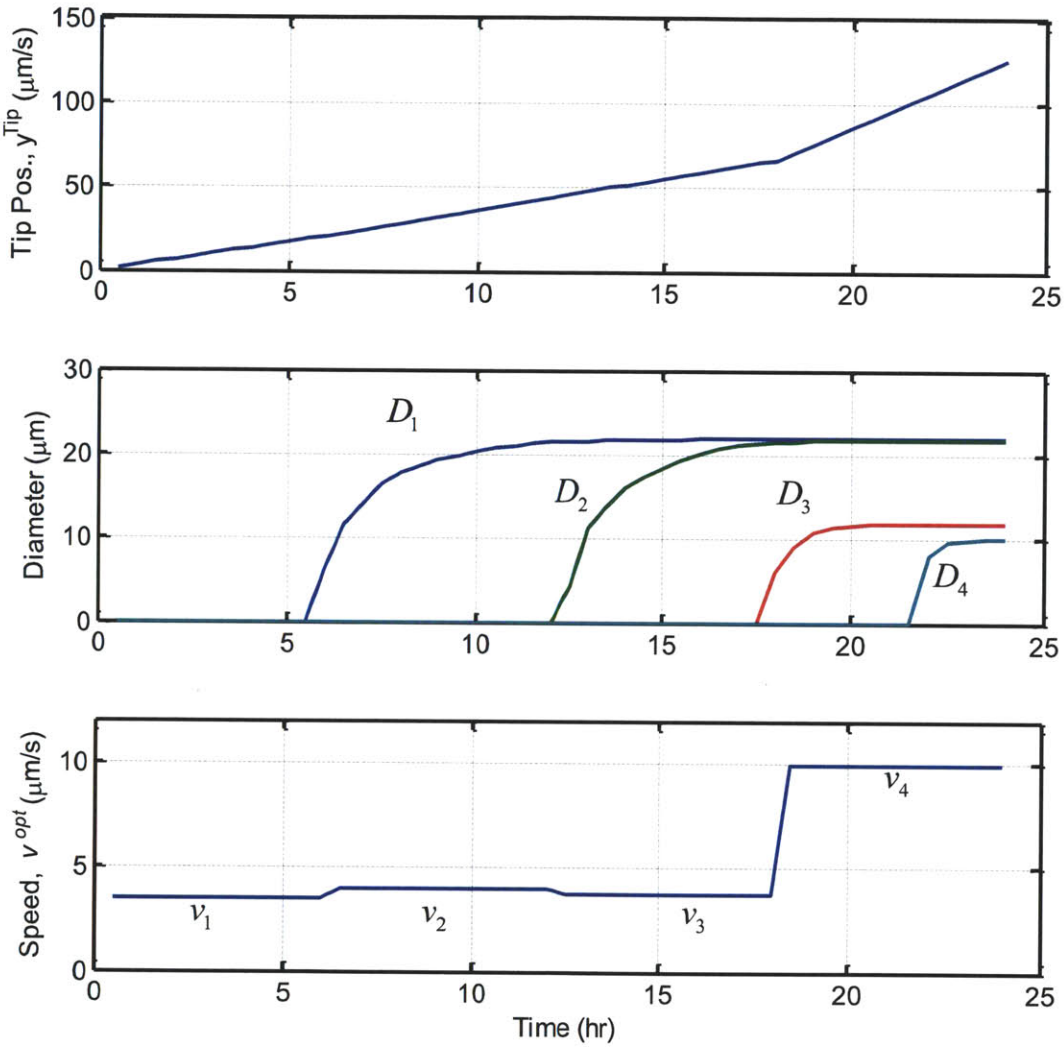

Figure 4-5: State and input time courses using optimal input sequence, $\mathbf{v^{opt}}$.

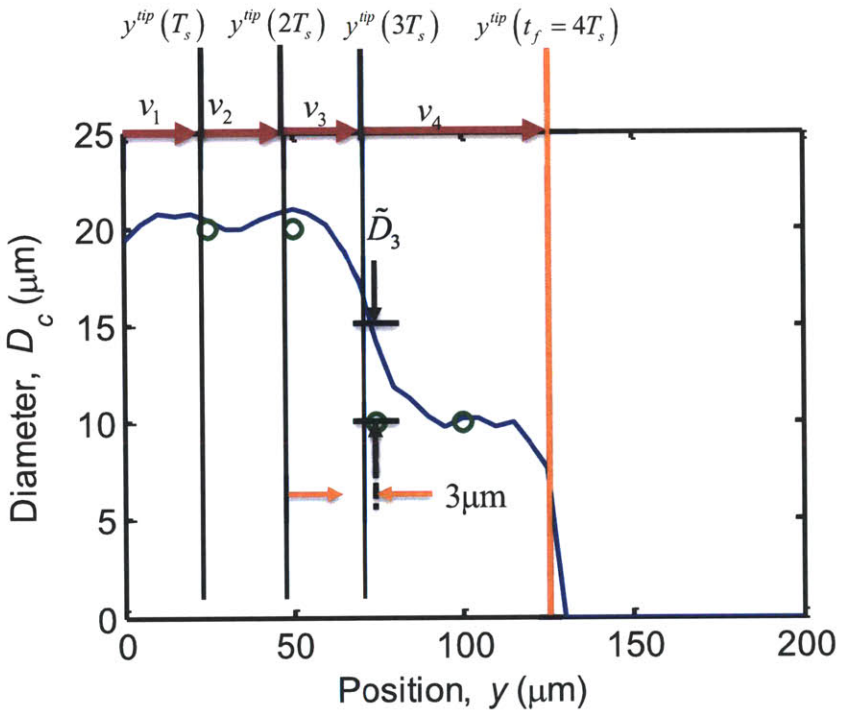

Figure 4-6: Conduit profile obtained by manually manipulating input sequence, $\mathbf{v}$, to reduce error in D_1 and D_2.

4.2 Using ∇ VEGF to Manipulate Speed

Formulating a practical control strategy faces the additional challenge that our model only provides a relationship between $v^{tip}(t)$ and resultant geometry, but does not relate application of biochemical factors, such as ∇VEGF to v^{tip}. Tip cell speed depends on a wide variety of factors, including the state of the tip cell itself, such as activation of migration related signaling pathways, including Rac, Rho, and Focal Adhesion Kinase, among many others [68, 72, 41], and expression of cell-cell and cell-ECM receptors such as integrins and cadherins. In addition, ECM microstructure, including density of collagen fibers, and the presence of cell-cell junctions may play a role [3]. Each of these processes is influenced by many of the others, leading to a complex and, so far, poorly quantified set of mechanisms. Understanding of the interplay between these mechanisms and the final tip cell speed is a formidable and open question and is outside of the scope of this thesis.

In this work, all of our characterization has been conducted using EGM-2MV with different concentrations and gradients of VEGF. To evaluate how effectively we could manipulate elongation rate using VEGF gradients, we observed the growth of 32 sprouts in a microfluidic device, and applied a step input in ∇ VEGF (see Fig. 4-7). We found that we were able to increase mean spead by about 50% with a similar rise in standard deviation (Fig. 4-8).

With standard deviation on the order of the mean, it will be exceedingly difficult to use ∇VEGF as a control input for manipulating elongation rate. As we will discuss more at the end of this chapter and in Section 5.2.1, new approaches will be needed to reduced the variance in the speed response. However, whatever approach proves to be successful in reducing the variance, it is sure to be significant. Therefore, we will address closing the loop to correct for noise in the next two sections.

In the face of such large input speed variability, we propose that feedback control will provide a means of improving variability in the final geometry. In the following sections, we treat our input speed as being corrupted by additive white noise and illustrate the role of a feedback controller to actively correct growth in simulation.

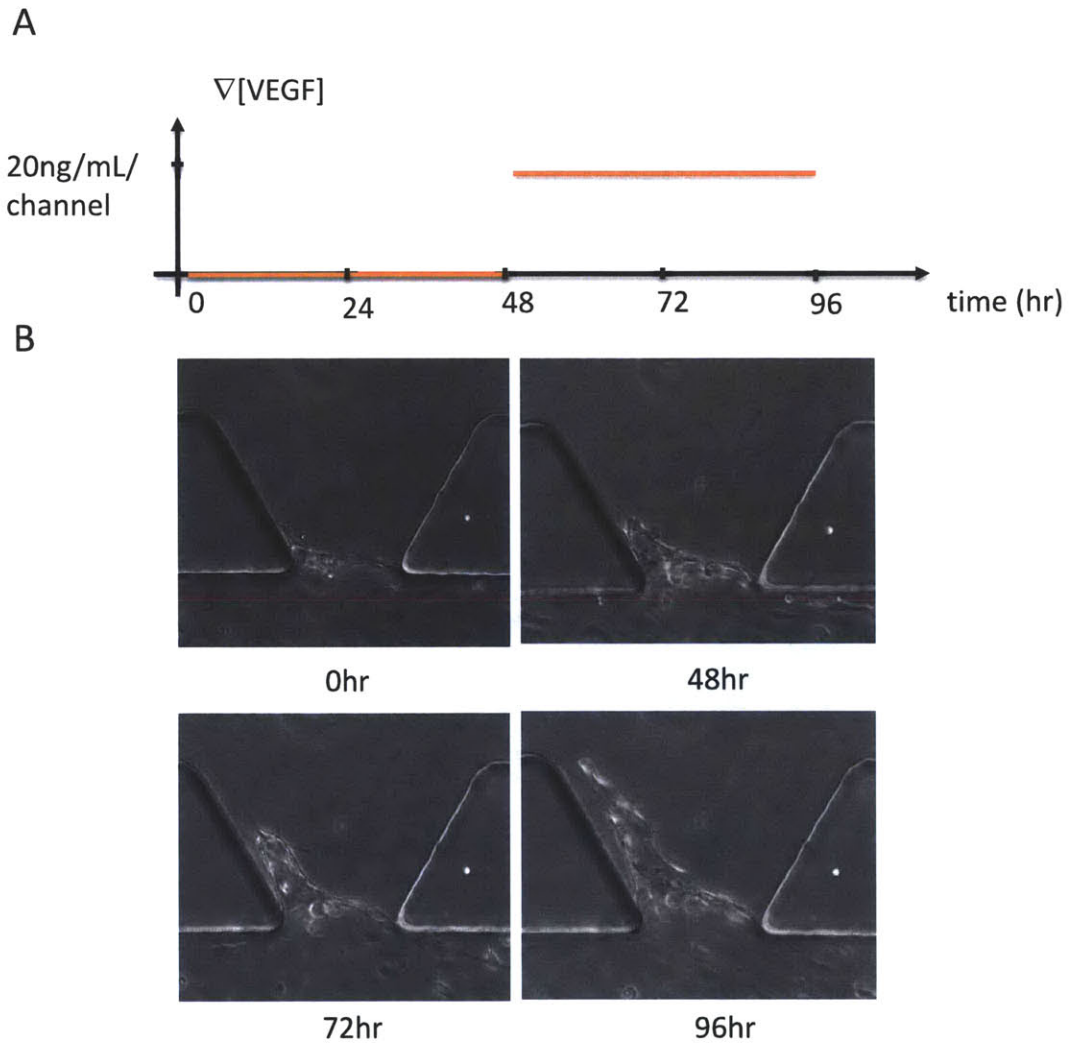

Figure 4-7: Example of sprout changing elongation rate when ∇ VEGF is increased from 0 to 20ng/mL/(gel width).

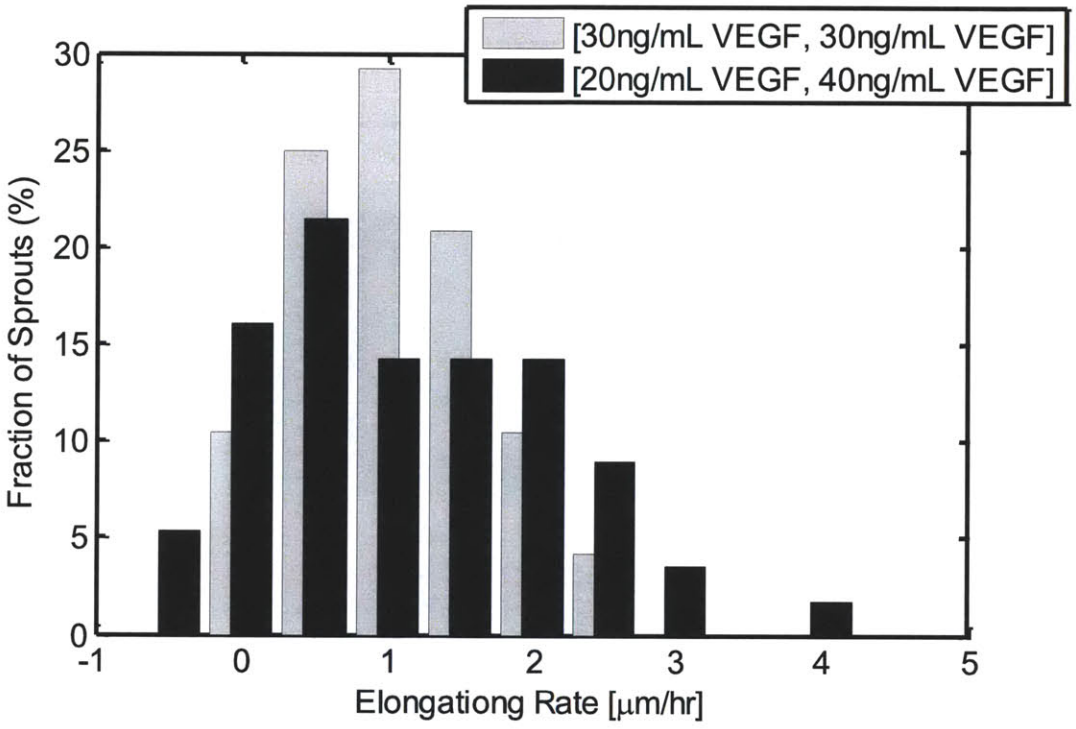

Figure 4-8: Histogram of 32 sprouts' elongation rate before and after a step input of ∇VEGF from 0 to 20ng/mL/(gel width). Mean speed was 0.8 ± 0.7SD μm/hr for 0-48hr and 1.2 ± 1.1SD μm/hr for 48-96hr.

4.3 Reduced Parameterization Approach

In our experience, descending the cost surface typically requires ~ 100 complete forward simulations before the optimum is obtained, depending on how far the initial guess is from the optimal speed sequence. Simulating the full PDE's in COMSOL requires $\sim$ 1min to forward simulate 24hr, meaning that obtaining an optimal input sequence via Eq. 4.5 often requires more than 1hr of computation time. This computation time is well within our estimated sampling time of $T_s = 6$hr, but we have so far only considered a deterministic process. As we introduce process noise in the next section, many more function calls will be necessary to evaluate the mean value of the terminal squared error in Eq. 4.4, requiring perhaps an order of magnitude more computation time.

With this in mind, we explored a simple approximation to the full PDE's by parameterizing to match the computational model. To begin, we recognize that collagen cleaving and increase of the conduit diameter is caused by MMP diffusion in the viscinity of the tip cell. Therefore, MMP concentration at the conduit centerline may be a good indicator of rate of change of diametric increase. To begin, we used the 2D COMSOL model to simulate a tip cell moving at constant velocity, and measured the resultant steady state MMP profile at the centerline, as a function of the distance δ behind the tip cell. Fig. 4-9A shows the profiles taken from simulations at several different cell speeds. The steady state profile changes amplitude, but its other features do not significantly vary with speed. As shown in Fig. 4-9B, normalizing the curves by their maximum values collapses them onto a single curve.

To understand how to parameterize the curve, we recognize that there is little MMP loss within the confines of the conduit — most of the collagen is already degraded except for at the boundaries. Therefore, we turn to the analytic solution for diffusion from a transient point source in a *non-reactive medium* [13]. In our usual axisymmetric coordinates (see Appendix A.5).

$$q(r,y,t) = \frac{Q_{source}}{[4\pi Dt]^{3/2}} \exp\left[-\frac{r^2 + (y - y^{tip}(t))^2}{4Dt}\right] \tag{4.6}$$

In a non-reactive medium, the previous solution could be integrated, with Q_{source} changed to $\dot{Q}_{source}$ to yield the MMP profile vs. time. However, our MMP profile is consumed by the collagen matrix at the conduit boundaries with a characteristic time constant taken from the reaction term of Eq. 3.3:

$$\tau_{MMP} \sim \frac{1}{k_q c_0} = 0.14\text{s} \tag{4.7}$$

with values taken from Table 3.1. Therefore, for longer time intervals, our MMP profile may be approximated in terms of a Bell curve similar to Eq. 4.6. Since our process is operating in steady state, there should be no time dependence if the profile is parameterized in terms of $\delta = y^{tip} - y$. Therefore, we assume a form

$$\hat{q}\left(r = 0, \delta\right) = \exp\left(-\frac{\delta^2}{a^2}\right) \tag{4.8}$$

where a is a length scale. Here we take $a = 9\mu$m. As shown in Fig. 4-9B, the Bell curve approximation is able to capture the MMP profiles. Note that there is some error in front of the cell. This is likely due to a higher rate of MMP loss in front of the cell since collagen concentration is higher there.

One note here is that we have not included the influence of tip cell speed on the transient solution. We are able to do so because diffusion in the y-direction dominates over tip cell motion based convection, $v^{tip}a/D << 1$. Therefore, the tip cell velocity does not significantly influence the profile.

Next, we checked to see whether we could use the Bell curve approximation to the MMP profile to predict the change in the conduit diameter as the tip cell passes through a particular location, $y = 100\mu$m. We note that conduit area, rather than diameter, varies linearly with quantity of MMP released at a cross section. Therefore, we write our dynamics in terms of the conduit cross sectional area $A\left(y\right) = \frac{\pi}{4} {D_c}^2\left(y\right)$. Then we have

$$\dot{A}\left(y, y^{tip}\right) = \kappa \exp\left[-\frac{\left(y - y^{tip}\right)^2}{a^2}\right] \tag{4.9}$$

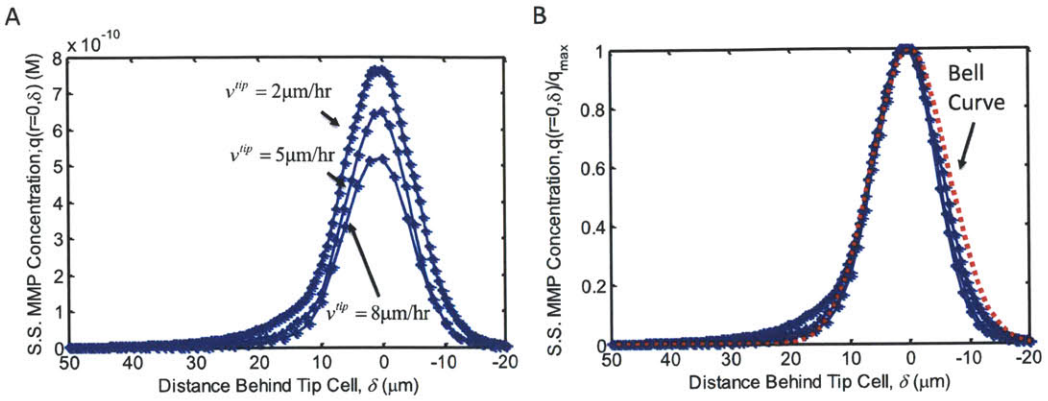

Figure 4-9: MMP profiles taken from computational model in COMSOL. (A). Steady state MMP profiles at the conduit centerline, $q(r=0,\delta)$, measured from the 2D COMSOL model while tip cell is moving at steady speed of 2,5, or 8μm/hr in a straight line. (B) Centerline MMP profiles from (A) collapse onto a single curve when normalized by their peak values, which can be approximated by a Bell curve.

Next, recalling that $\delta = y^{tip} - y$ and integrating from $t = 0$ to t_f yields

$$\begin{aligned} A(y,t_f) &= \kappa \int_0^{t_f} \exp\left[-\frac{\left(y-y^{tip}(t)\right)^2}{a^2}\right] dt \\ &= \kappa \int_0^{t_f} \exp\left[-\frac{\delta^2}{a^2}\right] dt \end{aligned} \tag{4.10}$$

but $d\delta = dy^{tip} = v^{tip}t$, so assuming that the tip cell has passed through the location y and that $\delta >> a$ at time t_f,

$$\begin{aligned} A(y,t_f) &\approx \tfrac{\kappa}{v^{tip}} \int_{-\infty}^{\infty} \exp\left[-\tfrac{\delta^2}{a^2}\right] d\delta \\ &\approx \tfrac{1}{v^{tip}} \kappa \sqrt{\pi a^2} \end{aligned} \tag{4.11}$$

since we know from Chapter 3 that $D_c = 40\sqrt{1/v}$ and $a = 9\mu$m we have that $\kappa = 79.3\mu\text{m}^2/\text{s}$.

Using Eq. 4.9, we are not able to perfectly predict the conduit diameter for all time (Fig. 4-10), but we can predict the final diameter with root-mean squared error of approximately 1μm in the range of speeds we have observed in experiments $(2-10\mu\text{m})$.

Everything we have done so far assumes a constant speed, v^{tip}, and a steady

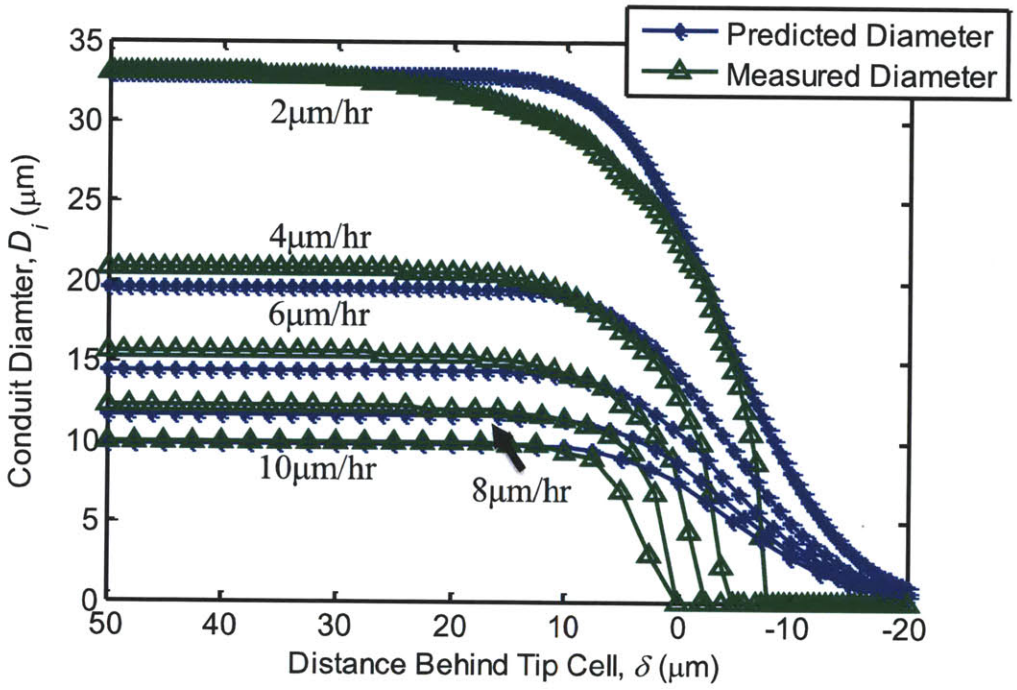

Figure 4-10: MMP concentration at the conduit centerline, $q(0, \delta)$ is a good indicator for rate of change of the conduit boundary at δ.

state MMP profile. However, the MMP profile is speed dependent. We assume that we are able to change speed every $T_s = 6$hr, so it is important to understand how significantly these changes will influence our predictive capability. To this end, we apply a step in speed from $v^{tip} = 5\mu$m/hr while $\delta < 0$ to $v^{tip} = 2\mu$m/hr while $\delta \geq 0$. As shown in Fig. 4-11, the distribution requires approximately 1hr and 3μm until the the profile transitions to within 5% of its new steady state profile. During this time, the conduit diameter changes from approximately 12 to 20μm, the conduit shifts to the new steady state conditions (like in Fig. 4-9).

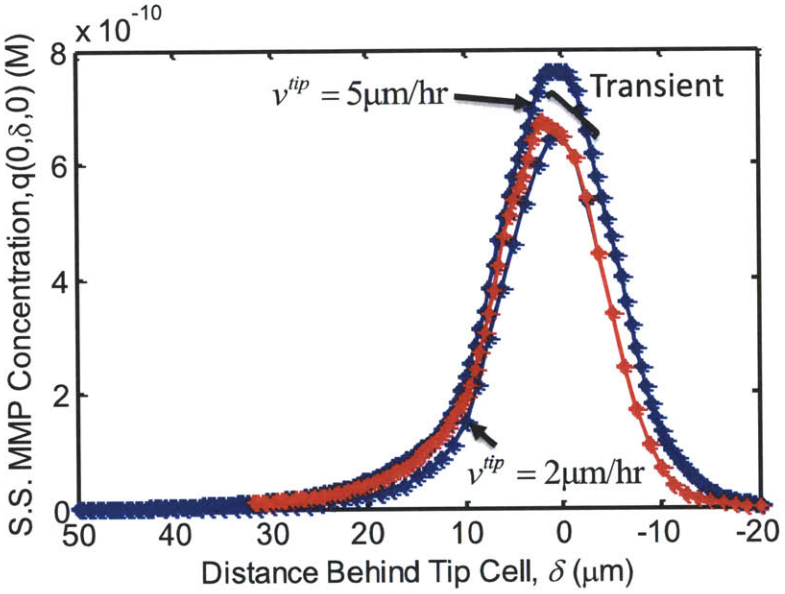

Figure 4-11: Transient MMP measurements from COMSOL at $y = 100\mu$m after step in speed from $v^{tip} = 5\mu$m/hr to $v^{tip} = 2\mu$m/hr at $\delta = 0$ compared with steady state MMP profiles for both speeds. Markers are measurements taken every 1hr.

This entire section has sought to pose a simple set of equations that capture the dominant aspects of the full COMSOL PDE solutions. We are trading low simulation error for computational speed. The last question is whether the simplified solution does an adequate job of predicting the diameter profile and whether the obtained policy matches the policy obtained via COMSOL.

First, we checked to see how well the resulting diameter profile matched the one obtained from COMSOL using the COMSOL-based $\mathbf{v}^{\mathbf{opt}}$. As shown in Fig. 4-12,

the reduced model is able to capture the major features of the full COMSOL model, except for some over prediction of diameter in the transient region near $y^{tip}(t_f)$. The root mean squared error between the two models is 2.1μm for the portion of the conduit behind $y^{tip}(t_f)$.

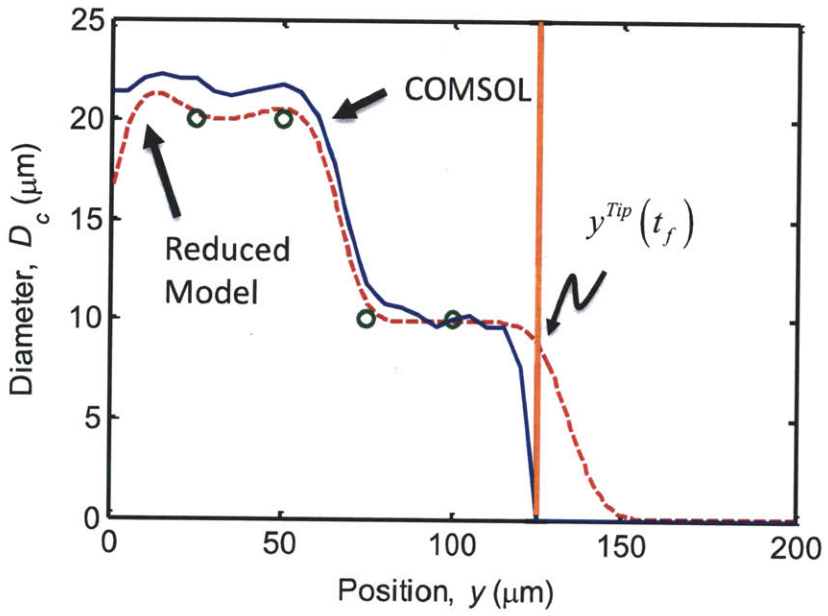

Figure 4-12: Comparison of resultant diameter profile at time t_f from COMSOL and reduced parameter models.

The reduced model captures the final conduit geometry, $D_c(y;t_f)$, but can we use it to estimate the optimal input sequence? Revisiting the optimization problem in the previous section, but now using the reduced model to optimize our cost function, Eq. 4.4, we obtain the reduced parameter optimal policy $\hat{\mathbf{v}}^{\mathbf{opt}} = [\hat{v}_1 \cdots \hat{v}_4]$, and yielding the final conduit profile, $D_c(y;t_f)$, in Fig. 4-13 and input and state time profiles in 4-14. The final profiles look similar, but the reduced parameter model achieved somewhat smaller final error in the desired states by accentuating the changes in speed from interval to interval. The root-mean squared error in velocity is 1.2μm. We stress that results would be more similar to the COMSOL result if additional states were added — at $y = 15\mu$m, for example. The optimal solution from COMSOL may not have converged on this result in part because of the 3μm mesh size used in the simulation, which reduces resolution in the output measurements. In our experience,

decreasing the mesh size to 1μm can increase computation time by as much as an order of magnitude, and is therefore not practical.

Given the assumptions and discrepancies between the reduced model and the computational COMSOL model, we propose that the utility of the reduced model is to find candidate optimal solutions or initial "guesses" for use in the COMSOL optimizer. All optimal input trajectories should be checked against the COMSOL solution

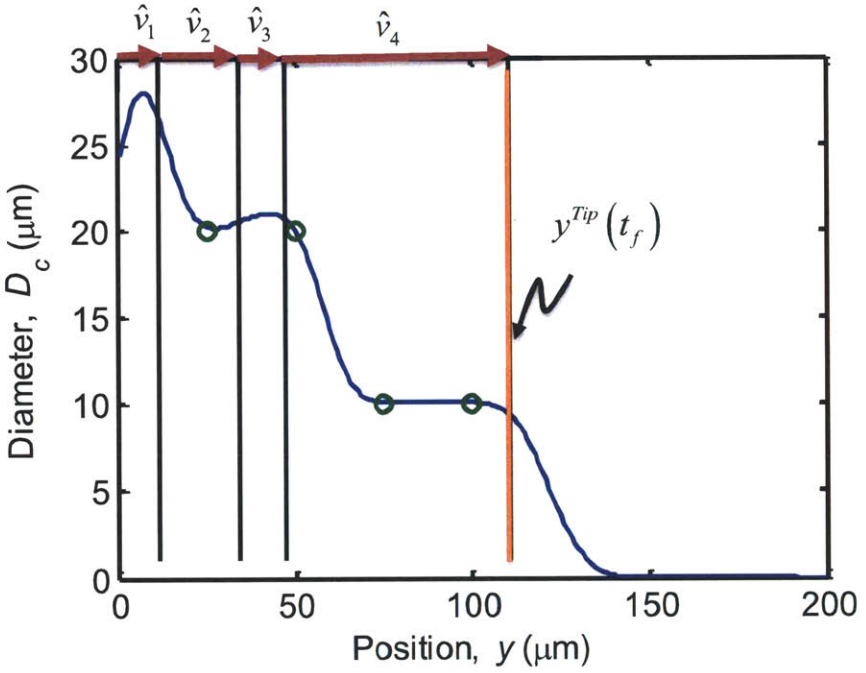

Figure 4-13: Reduced model conduit profile obtained using $\hat{\mathbf{v}}^{\mathbf{opt}}$.

4.4 Feedback

As illustrated in Figs. 4-7 and 4-8, controlling tip cell speed, $v^{tip}(t)$ via application of biochemical factors suffers from very high noise in the response. In addition, the speed-diameter relationship may face process noise due to factors such as inhomogeneities in local collagen concentration or variation in the MMP expression rate to list a few. Therefore, we need to have a means of checking to see whether the system

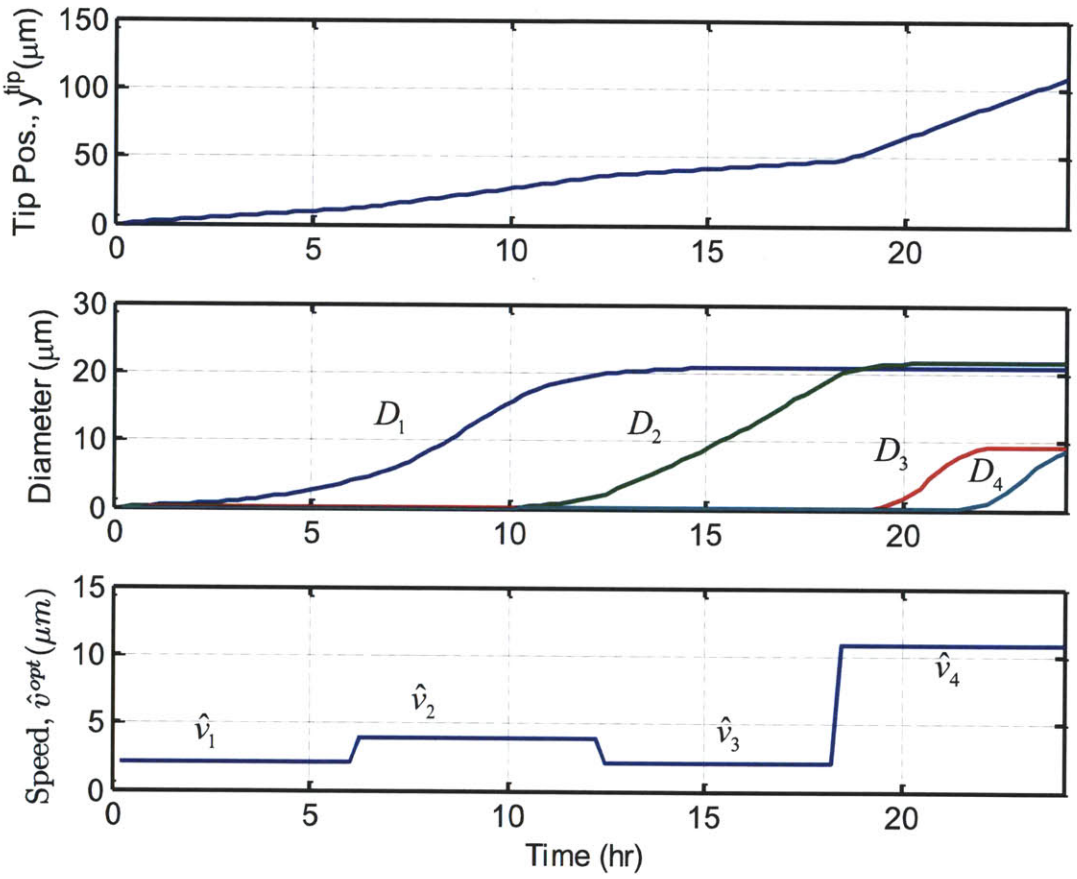

Figure 4-14: Reduced model state and input time courses using optimal input sequence, $\hat{\mathbf{v}}^{\mathbf{opt}}$.

states are evolving as expected and, if not, modifying the remainder of the input sequence to make corrections. Fig. 4-15 illustrates our assumed process dynamics and our scheme for correcting for error using a model predictive controller (MPC) [12, 65]. Since the speed response to a step in ∇VEGF in Fig. 4-8 takes a Gaussian character, we treat the input noise, $\omega(t)$, to be white noise and additive. The process noise, $\mathbf{w}(t)$, may require a more general model description depending on its source. For example, if the matrix inhomogeneities take on a white distribution, their effect may show up multiplicatively on the process dynamics.

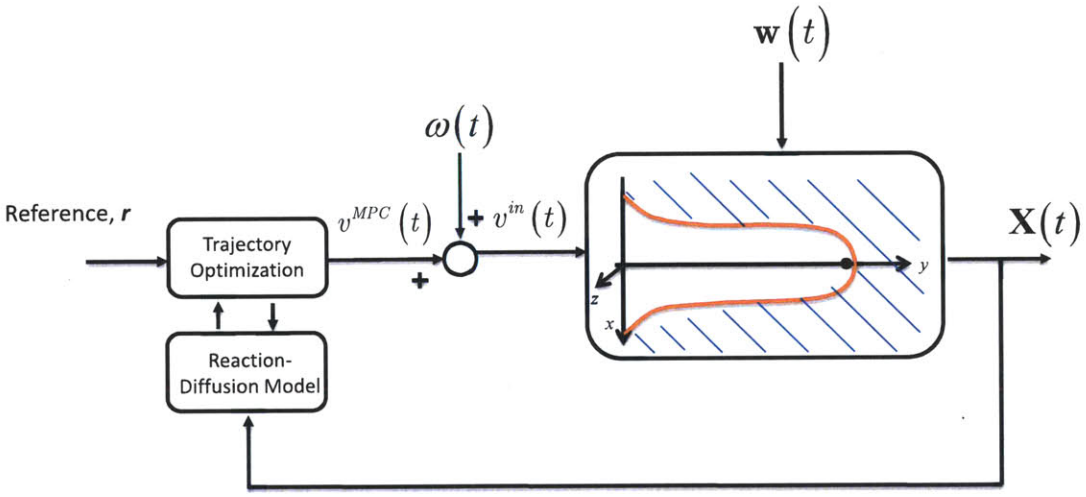

Figure 4-15: Model Predictive Control approach to compensate for input and process noise.

In the previous sections, without noise sources, we computed the entire optimal input sequence, $\mathbf{v^{opt}}$, ahead of time. Since there was no noise, we did not need to recompute the optimal solution at each step. Here we consider the influence of input noise, $\omega(t)$. Under the influence of input noise, we have that the actual tip cell speed during the i^{th} interval becomes

$$v_i^{in} = {v^{opt}}_i + \omega_i \tag{4.12}$$

where $\omega_i = \mathcal{N}(0, \sigma)$. Note that we are treating the input noise as taking a fixed value during the controller sampling period, T_s. This assumption may be appropriate

depending on the time constant of the cellular response to the input, τ_r. If $T_s >> \tau_r$ the assumption may not be appropriate. Since we take $T_s \sim \tau_r$, Eq. 4.12 should be an effective model.

Since the input speed is now stochastic, we need to optimize the input sequence to optimize the *expected* terminal squared error. In the MPC approach, we obtain the input sequence, $\mathbf{v^{MPC}} = \left[v_1^{MPC} \cdots v_m^{MPC}\right]$, to optimize the terminal expected squared error given the current state $\mathbf{X}\left(t = iT_s\right)$, and *assuming that we are not closing the loop* for the duration of the experiment. Therefore, to determine the first input v_1^{MPC} to apply, we define $\bar{\mathbf{v}}_1 = [\bar{v}_1 \cdots \bar{v}_m]$, compute

$$\bar{\mathbf{v}}_1 = \underset{\mathbf{v}\epsilon\mathfrak{V}}{\arg\min} \left\{ E\left[\tilde{\mathbf{X}}(t_f)^T Q \tilde{\mathbf{X}}\left(t_f\right) | \mathbf{X}\left(0\right), \mathbf{v}\right] \right\} \tag{4.13}$$

and assign

$$v_1^{MPC} = \bar{v}_1 \tag{4.14}$$

The assumption that the system will operate in the open loop during during the remainder of the time horizon makes the the resultant policy suboptimal [7]. However, this assumption vastly improves computational complexity and is the typical MPC approach.

Since the input speed is now stochastic, the original optimal policy computed at the beginning of the experiment, $\bar{\mathbf{v}}_1$ is now out of date and needs to be updated based on our measurement of the previous state $\mathbf{X}\left(T_s(i-1)\right)$. Therefore, at the i^{th} control interval we have

$$\bar{\mathbf{v}}_i = \underset{\mathbf{v}\epsilon\mathfrak{V}}{\arg\min} \left\{ E\left[\tilde{\mathbf{X}}(t_f)^T Q \tilde{\mathbf{X}}\left(t_f\right) | \mathbf{X}\left(T_s(i-1)\right), \mathbf{v}\right] \right\} \tag{4.15}$$

where $\bar{\mathbf{v}}_i = [\bar{v}_i \cdots \bar{v}_m]$. Then, assign

$$v_i^{MPC} = \bar{v}_i \tag{4.16}$$

We implemented the MPC approach using the reduced model with $\sigma = 2\mu$m/hr.

We estimated the expectation in the optimization step, Eq.4.15, by forward stimulating using $\mathbf{v}^{in}$ to the terminal state 100 times for each candidate input sequence. Fig. 4-16 shows the MPC input sequence, $\mathbf{v}^{MPC}$ compared with the actual speed $\mathbf{v}^{in}$, and the original estimate of the optimal input sequence $\bar{\mathbf{v}}_1$ in the lower panel. We can see that $\mathbf{v}^{in}$ stochastically fluctuates and does not match $\mathbf{v}^{MPC}$. During the second control interval from 6-12hr, the actual speed v_2^{in}, had enough error that the controller had to increase from its original estimate $\bar{\mathbf{v}}_1$ of the controller speed for $i = 3$ to the corrected value v_3^{MPC}.

The upper panels of Fig. 4-16 show the time evolution of the states subjected to the noisy input $\mathbf{v}^{in}$: $y^{tip}(t; \mathbf{v}^{in})$ and $D_i(t; \mathbf{v}^{in})$. As we can see, there was considerable terminal state error due to the noise in $\mathbf{v}^{in}$. $D_1(t_f; \mathbf{v}^{in})$ has a particularly large error of approximately 10μm due to the large discrepancy between v_2^{in} and v_2^{MPC}. The process evolution illustrating the reason for the very high error in terminal diameter is more apparent from Fig. 4-17, which illustrates the differences between the "expected" profile if $v_i^{in} = v_i^{MPC}$ and the actual profile obtained due to the noisy v_i^{in}.

To conclude this section, we wish to provide a performance measure given our MPC feedback control approach that relies on a coarse sampling period, and suffers from input disturbance. Unfortunately, the relationship between our inputs and cost function is 1) highly nonlinear due to the reaction-diffusion PDE process model and the entire time sequence of inputs determining the final cost, 2) the process is irreversible, and 3) the process is stochastic due the input disturbance. Furthermore, the expected terminal cost in our system will be highly influenced by initial conditions, including any initial growth (this chapter has assumed that initial conditions start with with a uniform diameter of 0).

Stability and performance bounds are well characterized for linear stochastic processes using stochastic Lyapunov functions [45], supermartingale theory [19], and other approaches of illustrating probability one convergence (see, for example [58]). In contrast, an expression for terminal cost in MPC of general nonlinear stochastic systems is not avalailabe. However, it is known that the terminal expected cost using MPC is less than or equal to the terminal expected cost using an optimal open loop

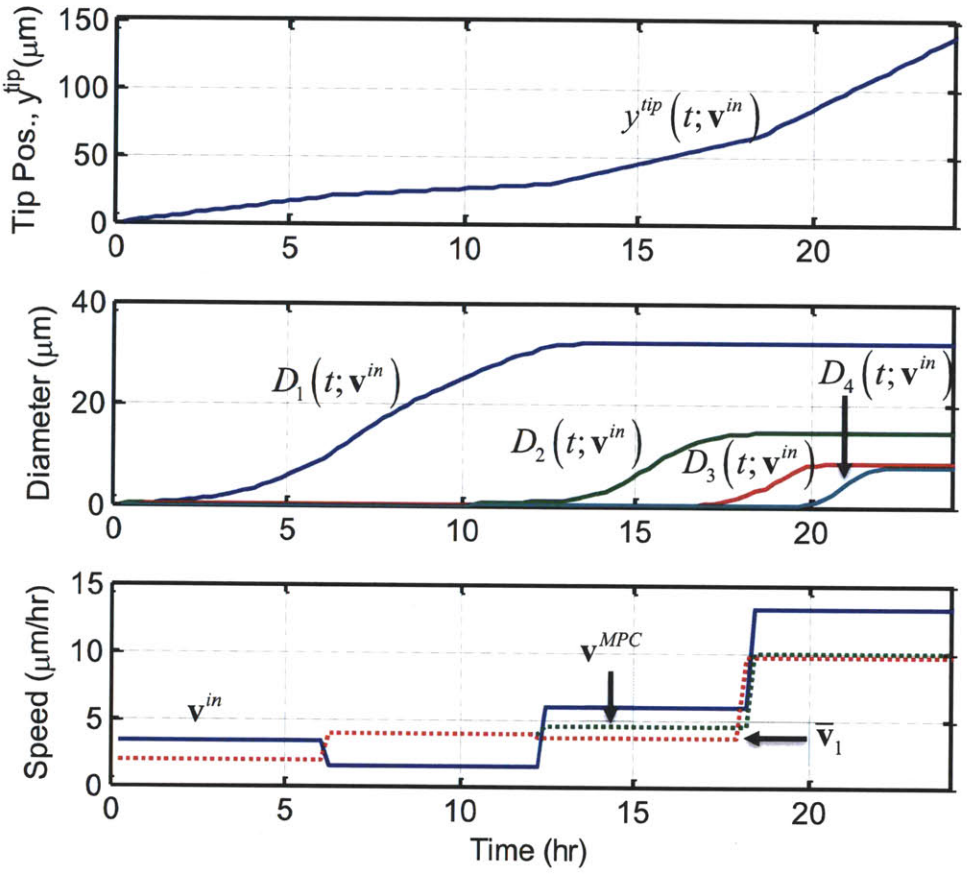

Figure 4-16: Simulated state (tip cell location and diameter) given input speed sequence $\mathbf{v}^{in}$ are shown in the top two panels. The lower panel compares the actual input sequence $\mathbf{v}^{in}$ with the computed MPC input sequence $\mathbf{v}^{MPC}$, and the initial trajectory optimization $\bar{\mathbf{v}}_1$.

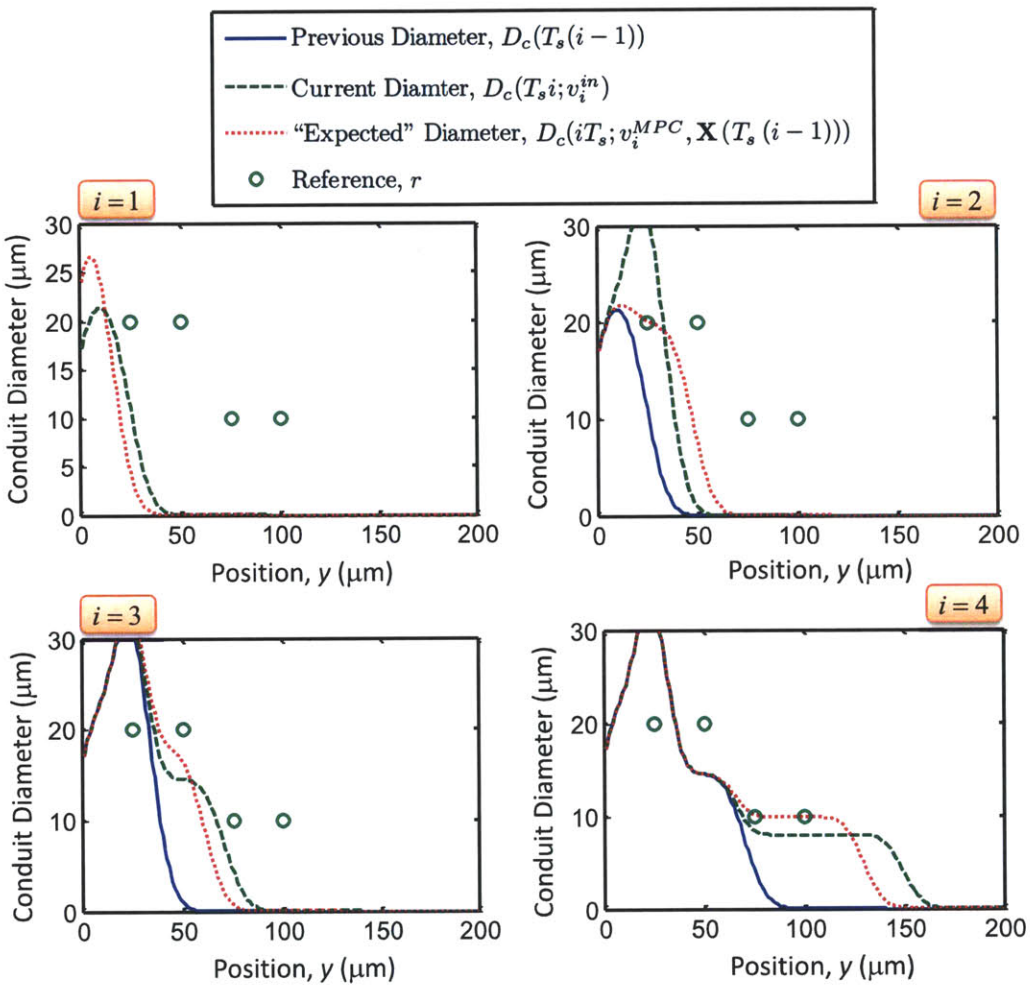

Figure 4-17: Illustration of the time sequence of diameter profile evolution at the end of the i^{th} interval. At the beginning of each interval, we start with state information $\boldsymbol{X}(T_s(i-1))$ and compute the input v_i^{MPC} that will minimize mean squared error during this time step. Each panel shows the "expected" diameter if v_i^{MPC} were not corrupted with noise, ω_i, and the actual result obtained from the noise corrupted v_i^{in}.

policy [7].

Since a general expression is not available, we can compute expected root mean squared (RMS) terminal cost vs. the magnitude of the input disturbance, σ (Fig. 4-18). Nonzero RMS error with $\sigma = 0$ implies that the desired terminal state is not perfectly reachable. Note that the RMS error curve shown applies only to the initial conditions and terminal desired state used above. A separate performance curve must be computed for different initial and desired terminal conditions.

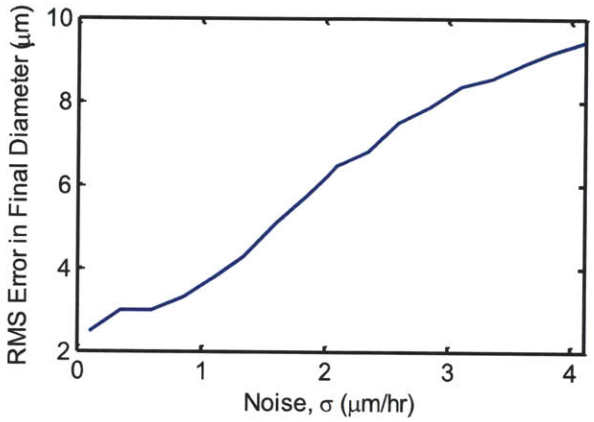

Figure 4-18: RMS diametric error vs. input disturbance magnitude, σ. RMS is taken as the square root of the terminal cost averaged over 10,000 MPC simulations and normalized by the number of reference diameters, n.

4.5 Correcting for Parameter Value Uncertainty

Before concluding this chapter we should briefly touch on the issue of incorrect knowledge/uncertainty of the model parameter values. This uncertainty can lead to considerable bias between the model and the experiment

$$\dot{\boldsymbol{\epsilon}} = E\left[\dot{\mathbf{X}}(t) - \dot{\hat{\mathbf{X}}}\left(t;\hat{\boldsymbol{\theta}}\right)\right] \tag{4.17}$$

where $\dot{\boldsymbol{X}}(t)$ are the true process dynamics, $\dot{\hat{\boldsymbol{X}}}\left(t;\hat{\boldsymbol{\theta}}\right)$ are the model predicted dynamics, and $\hat{\boldsymbol{\theta}}$ is the vector of estimated model parameters, including D, $\dot{Q}_{source}$, k_c, k_q, and c_0, as well as variance of the process and input disturbance. If knowledge of these

parameters is uncertain — in new experiments with new interventions, for example — the model will poorly predict the process. and the optimized input sequence will be incorrect.

To correct for this problem, we can turn to an estimation scheme to tune the model parameters, $\hat{\boldsymbol{\theta}}$ such that the model correctly predicts the experimental process dynamics that have been observed until the the most recent observation. Many approaches are available for tuning the parameters online, including Bayesian and Maximum Likelihood (ML) approaches [50]. A Bayesian estimator is more appropriate when apriori information about the parameter is available, but is computationally intensive. The ML approach is less computationally intensive yet provides a consistent parameter estimate even when the parameters are nonlinearly involved [50]. If the process noise, $\mathbf{w}$, is white, then the ML estimate at time T is

$$\hat{\boldsymbol{\theta}}^{ML}(T) = \arg\max_{\boldsymbol{\theta}} \prod_{i=1}^{T/T_s} \frac{1}{(2\pi)^{3/2}|\boldsymbol{S}|^{1/2}} \exp\left(-\frac{1}{2}\dot{\boldsymbol{\varepsilon}}(T_s i, \boldsymbol{X}(T_s i)\boldsymbol{\theta})^T \boldsymbol{S}^{-1} \dot{\boldsymbol{\varepsilon}}(T_s i, \boldsymbol{\theta})\right) \tag{4.18}$$

where $\boldsymbol{S} = E\left[\boldsymbol{w}\boldsymbol{w}^T\right]$. Two important questions in parameter estimation are 1) can the parammeters be estimated uniquely? and 2) how much variance is there in the estimate? The answers to these questions depend on the number of parameters, how they are involved in the process dynamics, and how well the system is excited based on the inputs. See Appendix B for discussion of identifiability and parameter estimation error variance for estimating parameters involved in individual cell migration.

4.6 Summary of Control

In this chapter, we developed a feedback control approach by starting with our mechanistic PDE model implimented in COMSOL, and reducing it to a much more computationally efficient parameterization. This simple model made it computationally feasible to implement a Model Predictive Controller to correct for noise in the input speed, which we implemented in simulation. Even with our modest noise level — with standard deviation on the order of one-half of the mean — there can still be

large error in the terminal diameter profile.

As shown in Fig. 4-8, we were able to experimentally influence sprout growth via application of biochemical factors such as ∇VEGF, but the noise in the process response is extremely high. Currently, the standard deviation is on the same order as the mean when using ∇VEGF as the control input. New methods of measuring and predicting tip cell response to biochemical inputs will be required to facilitate successful active regulation in angiogenic growth. These new methods include newly developed FRET based biosensors capable of measuring signaling pathway activation in real time [61], or different combinations of migratory cytokines which may yield a higher fidelity response.

A feedback control approach for controlling the vessel geometry will ultimately be necessary, when higher fidelity means of manipulating vessel elongation are achieved. This chapter has presented an effective framework to the task.

Chapter 5

Conclusion

5.1 Contribution of this Work

This thesis has developed a modeling and control framework for regulating angiogenic growth in 3D microfluidic angiogenesis models:

- We began by designing a new high throughput microfluidic assay that yielded a consistent relationship between diameter and elongation rate in nascent vessels.
- We employed the same assay with specific MMP inhibitors and inmmunofloures-cent stains to evaluate which species were most important and where they were localized. We discovered that soluble MMP2 activated at the leading tip cell plays a dominant role in determining nascent vessel diameter.
- We developed a four-parameter reaction-diffusion model, *with just one tunable parameter*, based on the experimentally supported dominant mechanism of sol-uble MMPs secreted from the tip cell. We computationally implemented the model in COMSOL and compared the results with experimental data. The model was able to predict the experimentally observed vessels across multiple experiments without the need to adjust the single tunable parameter.
- We designed an input speed trajectory optimization and feedback approach based on the computational COMSOL model. First, we optimized the speed

trajectory by forward simulating the computational COMSOL model without any input or process noise. Then, we developed a simple ODE state evolution model based on the computational COMSOL results for the full PDE's. Based on the simple model, we were able to optimize the input speed trajectory in simulation while taking into account noise in the input speed, and close the loop using Model Predictive Control to correct for undesirable growth due to the noise.

Combined, these findings provide a complete framework for determining the input speed profile needed to obtain desired nascent vessel geometry. This modeling and feedback approach will be useful in designing treatment time courses and actively correcting vascular network growth in tissue engineering applications. Furthermore, the quantitative model will provide a necessary addition to cell-level computation models attempting to quantify and predict individual cell motions and cell-cell interactions during vessel growth in angiogenesis. See Appendix B and [5, 34].

The key limitation of our approach is in modulating elongation rate using biochemical factors, such as VEGF. As shown in Fig. 4-8, the variability in elongation rate is extremely high. With high variability in the elongation rate, we will also have high variability in the terminal vessel geometry. Reducing variability will most likely require knowledge of dominant factors influencing migration potential, including chemotactic gradients, cell signaling state, and the local microenvironment. This is a currently active research topic [2, 34, 4, 76].

5.2 Future Directions

5.2.1 Completing the Feedback Loop

Based on our findings, the key to regulating geometry in the nascent vessel is low(er)-variance manipulation of vessel elongation rate. Two future avenues of research may yield advances here. The first is to look for more potent migratory stimukli (such as sphingosine-1-phosphate [20]), or combinations thereof, which may facilitate greater

authority over elongation rate. Another approach is to close the loop around migration rate or activation of migration-related signaling pathways, such as Rac, Rho, and Focal Adhesion Kinase. The development of new FRET-based biosensors [61] may enable real time observation of these pathways and provide a means of actively controlling the tip cell migratory potential by feeding back the state of the pathway activation.

5.2.2 Cell Cluster Models for Coordinated Growth

This thesis has focused on formulating a very simple model relating sprout elongation (and tip cell migration) to the nascent vessel geometry. Our approach is effective in describing the geometric evolution of intact vessels. However, the complete *in vivo* process involves multiples stages, including a pruning process where many sprouts are lost due to the cells dissociating, apoptosing, and being removed, and a maturation state where mural cells are attracted to stabilize and regularize vessel geometries [57]. As we move further toward computationally recreating the total angiogenic process, it will be necessary to incorporate more details of cellular phenotypic state, cell-cell, and cell-matrix interactions [17].

There are currently multiple groups working to this end in the literature [2, 34, 4, 76]. However, the challenge, is that a complete mechanistic model will be extremely complex, composed of 100's–1000's of parameters, without accurate estimates for their values. How can we reliably quantify the process using such a complex model?

We have already begun attempting to address this issue by posing a set of very simple low-order equations describing tip cell, and stalk cell migration with $\sim$10 parameters (see Appendix B and [78]). The equations have been designed such that the parameters can be tuned from confocal observations of cellular migration.

The tuned quantitative model from this work will well integrate with our individual cell-level model by quantitatively describing the vessel boundary, which may be taken as a known input for estimating the parameters involved in the individual cells' migration.

5.2.3 Branching Models

Another extension to our work, is formulation of a predictive model for the location of branching sites. As shown in Fig. 3-7, there are multiple cites of MT1-MMP expression at sufficient distances from the active tip cell. It has been suggested that MT1-MMP expression correlated with Notch/Dll4 signaling [28], and these cites may be good indicators of where branches will form. It has been suggested that cells far enough from an active tip cell take on a probabilistic competition to see which will become the tip cell first [4]. However, this competition weighted by Dll4 signaling or other mechanisms may be involved in regularized formation of a complete network.

Looking for the (quantitative) relationships in this process may yield insights into how tip elongation rate will influence the morphology of the complete network in addition to nascent vessel diameter.

Appendix A

Materials and Methods

A.1 Device Fabrication

The devices were fabricated out of polydimethylsiloxane (PDMS - Dow Corning Sylgard 184 at a ratio of 10:1 polymer to cross-linker) using standard soft lithography techniques [48]. Devices were wet autoclaved for 20 minutes followed by a dry autoclave cycle for 20min and baked overnight at 80°C to dry. Devices were plasma bonded to #1.5 glass cover slips (Cell Path) that were pretreated with ethanol. All device channels were then treated with 1 mg/mL poly-D-lysine (PDL) solution (Sigma-Aldrich) for 4hr to enhance cell and collagen matrix binding to the device material [49], followed by additional baking at 80°C for 24-48 hours to dry and make the devices hydrophobic.

Type I collagen gel (BD Biosciences Cat. No. 354236) was prepared at 2.5 mg/mL and pH 7.4, and was pipetted into the devices at low injection pressures to avoid spillage into the main channels. The injection pressures were lower than the upper limit determined by the surface tension cage. Once in place, the collagen solution was allowed to gel for 1 hour in a humidity box via thermal cross-linking. The media channels were then filled with microvascular endothelial growth media (Lonza EGM-2MV Cat. No. CC-3202) to hydrate the gel, and prepare it for endothelial cell adhesion and growth.

A.2 Cell Culture

A.2.1 Passaging and Live Cell Staining

Human microvascular endothelial cells (hmVECs - Lonza Cat. No. CC-2543) were received at passage 3 and expanded to passage 7 in endothelial growth media (Lonza EGM-2MV Cat. No. CC-3202) via standard mammalian adherent cell culture protocols, and then cryogenically frozen until needed. When cells were needed prior to seeding in a device, a passage 7 vial was thawed and expanded to passage 8.

When the cells reached 80-90% confluence, the cells were trypsinized (0.05% Trypsin EDTA, Invitrogen), centrifuged, and then suspended in endothelial growth media to a density of 2.5 million cells/mL. In some experiments (where indicated) live staining of the cells enabled confocal imaging before and after biochemical conditions were applied to the gel region.

Live staining experiments used the cytosolic stain CellTracker Green CMFDA (Invitrogen Cat No. C7025) or CellTracker Orange CMRA (Invitrogen Cat No. C34551) at 5μM, with the nuclear stain Hoechst 33342 (Invitrogen Cat. No. H1399) at 0.1μM both using the recommended protocols for CMFDA from Invitrogen. These stain concentrations were found to maintain cell viability as well as sustained image contrast for the duration of the cultures in the devices.

A.2.2 Cell Loading into Microfluidic Device

Cells were seeded through the main flow channels of the devices. In all cell experiments in this thesis, the downstreem "Y-junction" between channels a and b was blocked with type I collagen. Flow was not used. The hydrostatic pressures across the channels were controlled by pipetting droplets of various sizes for each of the ports (Fig. A-1) and were managed to enable net cell convection in the seeding channel along the length of the device. Additionally, the pressures were managed so as to create a slow interstitial flow through the gel that biases the cells towards the gel for adhering on the gel-medium interface (Fig. A-1). Care was taken to ensure that cells

did not excessively crowd the gel region so as to avoid necrosis.

The cell-seeded devices were allowed to culture for 24hr before condition was applied to ensure a confluent monolayer. Any devices that did not have a confluent monolayer or exhibited excessive cell buildup on the gel regions were discarded after 24hr. After the biochemical condition was applied, the channel medium was replaced every 12hr.

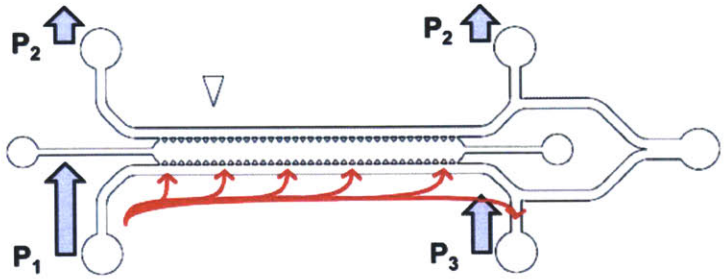

Figure A-1: Illustration of pressure adjustment for cell seeding protocol. A pipette may be used at the port labeled P_3 to draw the cell suspension through more quickly and ensure uniform seeding down the length of the channel.

A.3 Endpoint Staining

Devices were fixed by flowing 4% paraformaldehyde into the channels and leaving it for 10-15mins. Afterward, the devices were blocked with goat serum (Sigma G9023) for 2 hr and MT1-MMP primary antibody in chicken (Sigma Cat. No. GW21125) was applied at 1:100 dilution ratio overnight at 4 C. The following day, Alexa Flour 568 goat anti-chicken (Invitrogen Cat. No. A11041) was flowed into the channels at a dilution ratio of 1:200 and incubated at room temperature for 2hr. Nuclei and F-actin were stained with 1 μM Hoeschest 33342 (Invitrogen Cat. No. H3570) and Alexa 488 Phalloidin (Invitrogen Cat No. A12379) for 30-60min.

A.4 Diameter Measurement

The diameters plotted in Fig. 3-1B were selectively measured from confocal images of nascent vessels with a geometry consisting of an approximately straight centerline, had diameters that had less than 20% variation along their lengths, and had less than 20% difference between the measurements xz-diameter and xy-diameter (see Fig. A-2). The reported diameter values are the means of the xy-diameter along the length of the centerline. Mean elongation speed, was computed as

$$v_{mean} = \frac{\text{measured length}}{\text{experiment duration}} \tag{A.1}$$

Do to the large number of data needed to compute the statistical responses to multiple MMP inhibitors and limited confocal microscope availability, the data in Fig. 3-5, were measured from 2D phase contrast images and taken as the mean value from intact vessels like those shown in Fig. 3-3.

A.5 COMSOL Simulations

The PDE reaction-diffusion model, Eqs. 3.3-3.4, was implemented in COMSOL Multiphysics 4.2 with the chemical reaction toolbox (COMSOL - Burlington, MA) and simulation analysis was conducted in MATLAB (MathWorks, Inc. - Natick, MA). Analysis of the steady state elongation behavior and input optimization for control were conducted using 2D axisymmetric coordinates, infinite boundary conditions, and $\sim 3\mu$m triangular mesh size. The PARDISO algorithm was used. Simulations conducted for comparison with endpoint data implemented the full 3D post geometry (Fig. A-3) with no flux boundary conditions, and $\sim 10\mu m$ triangular mesh size. The 3D simulations used the Biconjugate Gradient Stabilization Method.

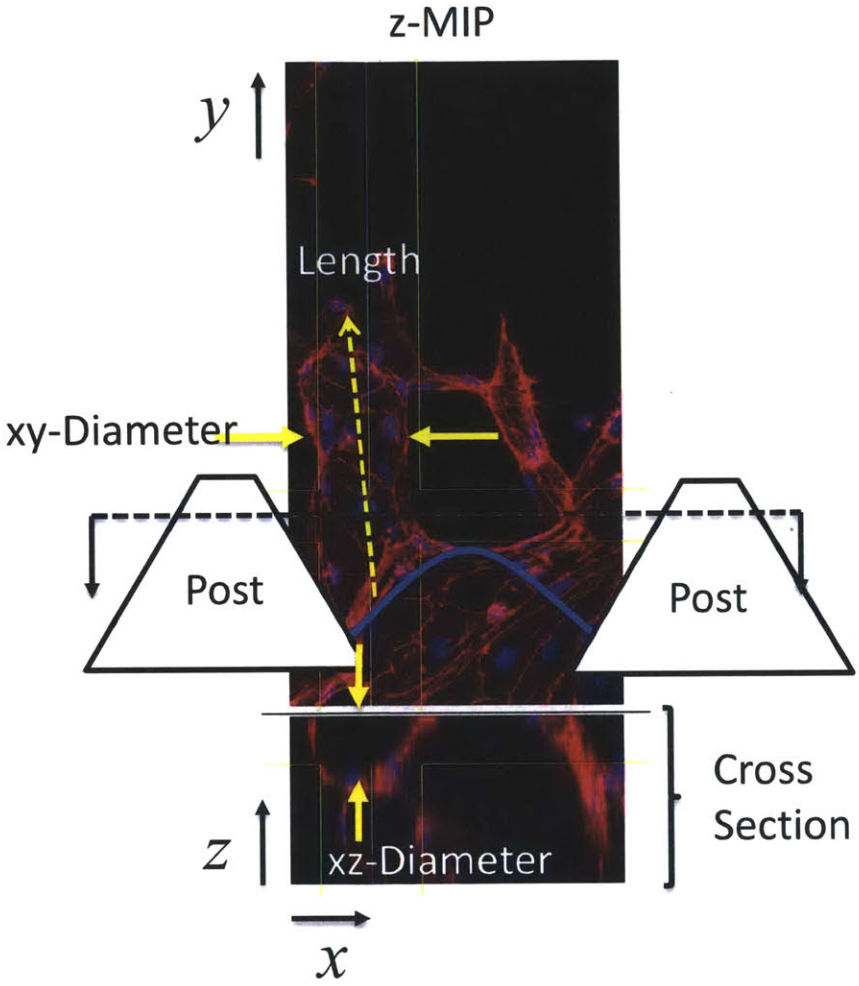

Figure A-2: Illustration of diameter measurement procedure for data plotted in Fig. 3-1.

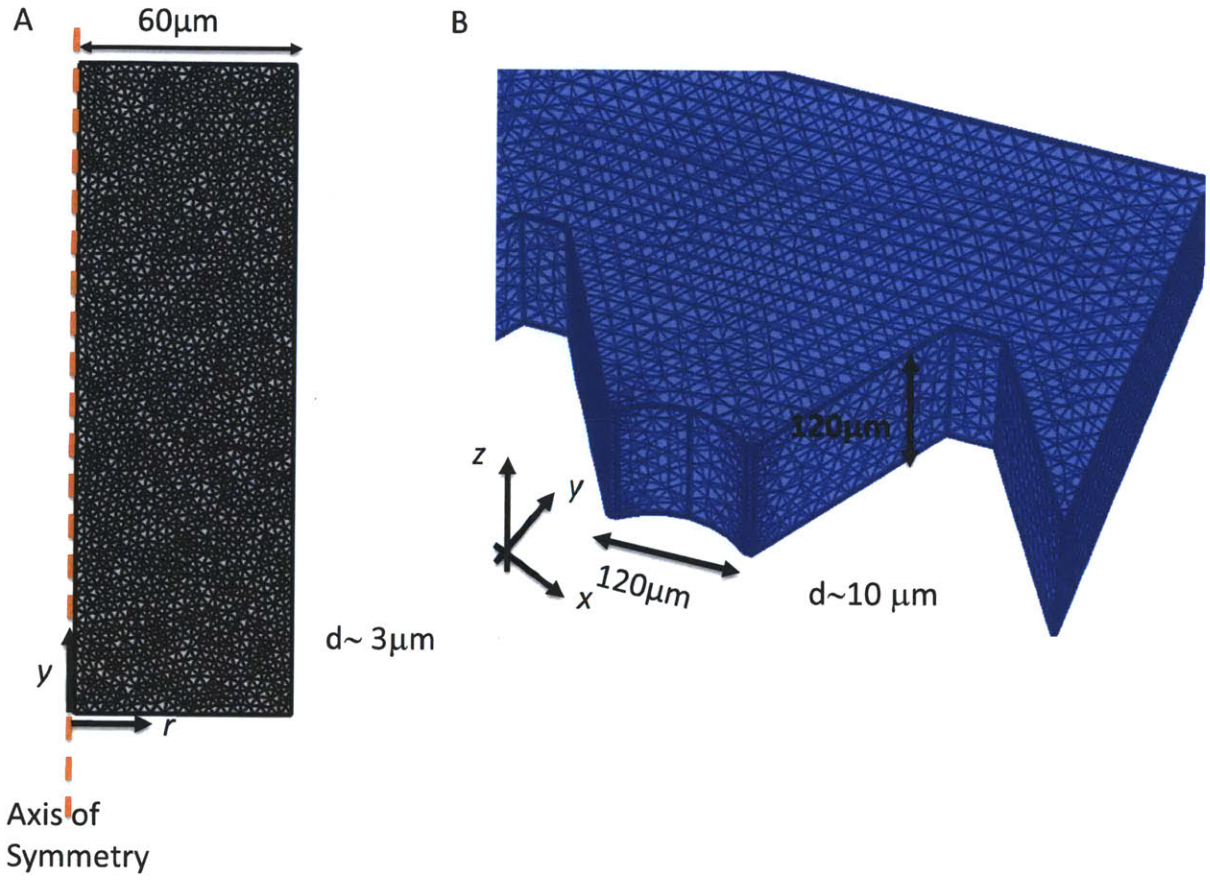

Figure A-3: (A) Illustration of 2D COMOSOL model used for steady-state analysis and control. (B) Full 3D geometry used for comparing computational model with control. Post, top, and bottom boundaries are no-flux.

A.6 MATLAB Optimization Codes for Control

A.6.1 Input Speed Optimization with COMSOL via LiveLink

speedopt.m

```
%%%%%%%%%%%%%%%%%%%%%%%%%%%%%%%%%%%%%%%%%%%%%%%%%%%%%%%%%%%%%%%%%%%%%%%%%%%%%%%%
%%%%%%%%%%%%%%%%%%%%%%%%%%%%%%%%%%%%%%%%%%%%%%%%%%%%%%%%%%%%%%%%%%%%%%%%%%%%%%%%
%Main optimization script using fmincon.

%pendfun calls COMSOL to evalute the terminal cost

options=optimset('MaxFunEvals',300, 'MaxIter', 300, 'TolFun', 0.1, 'DiffMinChange', 0.1);

tape_size=4;

alphalow    = 2*ones(tape_size,1);
alphaup     = 12*ones(tape_size,1);


 [thetaHat,g1,g2,g3,g4,g5,hessian]=fmincon(@(alpha) pendfun(alpha), ...
    alpha0,[],[],[],[],alphalow,alphaup,[],options)

%%%%%%%%%%%%%%%%%%%%%%%%%%%%%%%%%%%%%%%%%%%%%%%%%%%%%%%%%%%%%%%%%%%%%%%%%%%%%%%%
%%%%%%%%%%%%%%%%%%%%%%%%%%%%%%%%%%%%%%%%%%%%%%%%%%%%%%%%%%%%%%%%%%%%%%%%%%%%%%%%
```

pendfun.m

```
%%%%%%%%%%%%%%%%%%%%%%%%%%%%%%%%%%%%%%%%%%%%%%%%%%%%%%%%%%%%%%%%%%%%%%%%%%%%%%%%
%%%%%%%%%%%%%%%%%%%%%%%%%%%%%%%%%%%%%%%%%%%%%%%%%%%%%%%%%%%%%%%%%%%%%%%%%%%%%%%%
%Save the control input, and run COMSOL script, which will retreive it.
function [J] = pendfun(alpha_in)
alpha_in
alpha_save=alpha_in*1e-6/3600;
save('D:\Work\Comsol Testing\2DSim\TwoDOLFC2\controlu.mat', 'alpha_save')
global yTip diamMeas xdes


xdes=[100 20 20 10 10]';

%run COMSOL script and measure diameters at desired locations. Note: cannot
%be fun as a function. sproutFunction is actually as cript. This is a
%LiveLink limitation
sproutFunction

J = finalCost([yTip; diamMeas])

end % of pendfun

% ////////////////////////////////////////////////////////////////////////
% Compute terminal cost of diameter states
% ====================================================
function C = finalCost(X)
global xdes;

% Xerr = X - repmat(xdes,1,size(X,2));
% Xerr(1,:) = mod(Xerr(1,:)+pi,2*pi)-pi;
%
% [Q,R,Qend] = get_QR;
% %IMPLEMENT THE FINAL COST

%C=.5*Xerr'*Qend*Xerr;

C=sum((X(2:end)-xdes(2:end)).^2);
end
% ////////////////////////////////////////////////////////////////////////

%%%%%%%%%%%%%%%%%%%%%%%%%%%%%%%%%%%%%%%%%%%%%%%%%%%%%%%%%%%%%%%%%%%%%%%%%%%%%%%%
%%%%%%%%%%%%%%%%%%%%%%%%%%%%%%%%%%%%%%%%%%%%%%%%%%%%%%%%%%%%%%%%%%%%%%%%%%%%%%%%
```

sproutFunction.m

```
%%%%%%%%%%%%%%%%%%%%%%%%%%%%%%%%%%%%%%%%%%%%%%%%%%%%%%%%%%%%%%%%%%%%%%%%%%%%%%%%
%%%%%%%%%%%%%%%%%%%%%%%%%%%%%%%%%%%%%%%%%%%%%%%%%%%%%%%%%%%%%%%%%%%%%%%%%%%%%%%%
%This script loads the COMSOL model via LiveLink, manipulates parameters,
%and runs the simulation. Note that the input 'alpha_in' is provided to
%COMSOL via the COMSOL readable function yTipPos.m
global yTip diamMeas

%Load the COMSOL model
model=mphload('OLFC1.mph')

% Duration of simulation: 24hr
duration=86400; % in seconds

%model.param.set('vtip',vtip);
model.param.set('duration',duration);  %Send duration to the model

model.sol('sol1').run; % Run the simulation

ts=60^2; %in seconds

%set r and y measurement step sizes (x=r here)
xs=0.1;  %in um
%ys=2;    %in um

%Format a measurement grid
[x, y] = meshgrid([0:xs:60]*1e-6,[25 50 75 100]*1e-6);
sizex=size(x,1); sizey=size(x,2);
xx=reshape(x, sizex*sizey, 1); yy=reshape(y, sizex*sizey, 1);

%Measure model using LiveLink
[c q]= mphinterp(model,{'c', 'q'}, 'dataset', 'dset1','coord',[xx';yy'], 't', duration);
cc=reshape(c,sizex, sizey); qq=reshape(q,sizex, sizey);

yTip=mphglobal(model, 'yTip', 'dataset', 'dset1', 't',duration)*1e6

%Measure diameters based from collagen concentration values
diamMeas=zeros(sizex,1);
for i=1:sizex
    diamMeas(i)=2*length(find(cc(i,:)<0.2*8.6e-3))*xs;  %in um
end
%diamMeas

%Extract final geometry and time profiles, and plot
%////////////////////////////////////////////////////////////////////////////
%geometry profile
ys=5;
[x, y] = meshgrid([0:xs:60]*1e-6,[0:5:200]*1e-6);
sizex=size(x,1); sizey=size(x,2);
xx=reshape(x, sizex*sizey, 1); yy=reshape(y, sizex*sizey, 1);


[c q]= mphinterp(model,{'c', 'q'}, 'dataset', 'dset1','coord',[xx';yy'], 't', duration);
cc=reshape(c,sizex, sizey); qq=reshape(q,sizex, sizey);

diamOut=zeros(sizex,1);
for i=1:sizex
    diamOut(i)=2*length(find(cc(i,:)<0.2*8.6e-3))*xs;  %in um
end

figure; plot([0:5:200], diamOut, [25 50 75 100],  [20 20 10 10], 'o', 'LineWidth', 2);

% hold on
% figure; plot([25]*ones(25,1),[1:25], [25]*ones(25,1),[1:25],, [25]*ones(25,1),[1:25],[100]*ones
    (25,1),[1:25])
% xlabel('Position, {\it y} (\mum)'); ylabel('Diameter, {\it D_c} (\mum)')

%time profiles
dt=30*60; N=floor(duration/(30*60));

[x, y] = meshgrid([0:xs:60]*1e-6,[25 50 70 100]*1e-6);
sizex=size(x,1); sizey=size(x,2);
xx=reshape(x, sizex*sizey, 1); yy=reshape(y, sizex*sizey, 1);

uLoad=load('D:\Work\Comsol Testing\2DSim\TwoDOLFC2\controlu.mat');
u=uLoad.alpha_save;

diamTime=zeros(sizex,N);
for time=1:N
[c q]= mphinterp(model,{'c', 'q'}, 'dataset', 'dset1','coord',[xx';yy'], 't', time*dt);
cc=reshape(c,sizex, sizey); qq=reshape(q,sizex, sizey);

for i=1:sizex
    diamTime(i,time)=2*length(find(cc(i,:)<0.2*8.6e-3))*xs;  %in um
end
yTime(time)=mphglobal(model, 'yTip', 'dataset', 'dset1', 't',time*dt)*1e6;


uTime(time)=u(ceil(time*4/N));


end
```

```
figure(24)
subplot(311)
plot([dt:dt:dt*N]/60^2, yTime(1,:), 'LineWidth', 2);
ylabel('Tip Pos., y^{Tip} (\mum/s)')
grid on

subplot(312)
plot([dt:dt:dt*N]/60^2,diamTime(1,:), [dt:dt:dt*N]/60^2,diamTime(2,:), [dt:dt:dt*N]/60^2,diamTime
    (3,:)*11.8/max(diamTime(3,:)), [dt:dt:dt*N]/60^2,diamTime(4,:), 'LineWidth', 2);
ylabel('Diameter (\mum)')
grid on

subplot(313)
plot([dt:dt:dt*N]/60^2, uTime*3600e6, 'LineWidth', 2)
xlabel('Time (hr)'); ylabel('Speed, {\it v ^{opt}} (\mum/s)'); ylim([0 12])
grid on

figure(26); plot([0:5:200], diamOut, [25 50 75 100], [20 20 10 10], 'o', 'LineWidth', 2); hold on
plot([yTime(ceil(N/4))]*ones(25,1),[1:25], [yTime(ceil(N/2))]*ones(25,1),[1:25],[yTime(ceil(N*3/4)
    )]*ones(25,1),[1:25],[yTime(ceil(N))]*ones(25,1),[1:25])
xlabel('Position, {\it y} (\mum)'); ylabel('Diameter, {\it D_c} (\mum)')

%//////////////////////////////////////////////////////////////////////////
```

```
%%%%%%%%%%%%%%%%%%%%%%%%%%%%%%%%%%%%%%%%%%%%%%%%%%%%%%%%%%%%%%%%%%%%%%%%%%%%
%%%%%%%%%%%%%%%%%%%%%%%%%%%%%%%%%%%%%%%%%%%%%%%%%%%%%%%%%%%%%%%%%%%%%%%%%%%%
```

yTipPos.m

```
%%%%%%%%%%%%%%%%%%%%%%%%%%%%%%%%%%%%%%%%%%%%%%%%%%%%%%%%%%%%%%%%%%%%%%%%%%%%
%%%%%%%%%%%%%%%%%%%%%%%%%%%%%%%%%%%%%%%%%%%%%%%%%%%%%%%%%%%%%%%%%%%%%%%%%%%%
%COMSOL directly evalutes this function via LiveLink to comput yTip as a
%function of time given the control sequence alpha_in from pendfun.m. This
%function assume that alpha is of length 4 and duration=86400
function y=yTipPos(t)
uLoad=load('D:\Work\Comsol Testing\2DSim\TwoDOLFC2\controlu.mat')
u=uLoad.alpha_save;
u*3600*1e6 %convert units to um/hr from m/s
t1=86400/4;
t2=2*t1;
t3=3*t1;
t4=4*t1;
for i =1:length(t)
    if t(i)<t1
       y(i)=u(1)*t(i);
    elseif t(i)<t2
        y(i)=u(1)*t1 + u(2)*(t(i)-t1);
    elseif t(i)<t3
        y(i)=u(1)*t1+u(2)*(t2-t1)+u(3)*(t(i)-t2);
    else
        y(i)=u(1)*t1+u(2)*(t2-t1)+u(3)*(t3-t2)+u(4)*(t(i)-t3);
    end
end
end
%%%%%%%%%%%%%%%%%%%%%%%%%%%%%%%%%%%%%%%%%%%%%%%%%%%%%%%%%%%%%%%%%%%%%%%%%%%%
%%%%%%%%%%%%%%%%%%%%%%%%%%%%%%%%%%%%%%%%%%%%%%%%%%%%%%%%%%%%%%%%%%%%%%%%%%%%
```

A.6.2 OLFC Optimization with Reduced Model

OLFC3.m

```
%%%%%%%%%%%%%%%%%%%%%%%%%%%%%%%%%%%%%%%%%%%%%%%%%%%%%%%%%%%%%%%%%%%%%%%%%%%%
%%%%%%%%%%%%%%%%%%%%%%%%%%%%%%%%%%%%%%%%%%%%%%%%%%%%%%%%%%%%%%%%%%%%%%%%%%%%
%This is the main OLFC script

clc; close all; clear all

global K a y1 A1 y2 A2 y3 A3 y4 A4 xdes currentState currentTime;

y1 = 25;  A1 = pi/4*(20e-6)^2;
y2 = 50;  A2 = pi/4*(20e-6)^2;
y3 = 75;  A3 = pi/4*(10e-6)^2;
y4 = 100; A4 = pi/4*(10e-6)^2;

%Kappa(j)=13e-11*2e-2*2*(j)^(0.5)*(33/44)^2;


a = 1/80;
%K = 13e-11*2e-2*2*(33/44)^2;
```

```
xdes = [100 A1 A2 A3 A4]'; % the desired final state


% Plant dymanics
%////////////////////////////////////////////////////////////////////////
x = [0 0 0 0 0]'; %initial state
dt=0.24; %in hr
N=101;  %run for 24hr.
%alphaOld=zeros(5,1)+5;
alphaOld=[0 3.466 3.9 3.72 9.9]';

for i=1:N
    xOut(:,i)=x;

    if sum(i==round([1:N/4:N]))>0
        alpha=speedOptFMINCON(i,x, alphaOld); %Call fmincon to get updated input optimization
        u=alpha(1)+2*randn(1); %new input is the first element of the optimized alpha plus input
            noise
        if i ==1
            uOriginal=alpha;
        end
        uIntended=alpha(1);
        clear alphaOld
        alphaOld=alpha;
        clear alpha
    end

    uIntendedOut(i)=uIntended(1);
    uOut(i)=u;
    x = x + dynamics(x,u).*dt;   %keep track of actual evlution of states
    uOriginalOut(i)=uOriginal(ceil(i/N*4));
end
%////////////////////////////////////////////////////////////////////////

yTip=xOut(1,:);
save('yTipOpt.mat','yTip', 'uOriginalOut', 'uOut') % saveinputs and tip location

%Plot time profiles
%////////////////////////////////////////////////////////////////////////
figure(24)
subplot(311)
plot([dt:dt:dt*N], xOut(1,:));
xlim([0 24]); ylabel('Tip Pos., y^{tip}(\mum)')

subplot(312)
plot([dt:dt:dt*N],sqrt(4/pi*xOut(2,:)), [dt:dt:dt*N],sqrt(4/pi*xOut(3,:)), [dt:dt:dt*N],sqrt(4/pi*
    xOut(4,:)), [dt:dt:dt*N],sqrt(4/pi*xOut(5,:)));
xlim([0 24]); ylabel('Diameter, D_1, (\mum)')

subplot(313)
plot([dt:dt:dt*N],uOut, [dt:dt:dt*N], uIntendedOut, [dt:dt:dt*N], uOriginalOut)
xlabel('Time (hr)'); ylabel('Speed, u (\mum/hr)')
xlim([0 24]);
%////////////////////////////////////////////////////////////////////////

%%%%%%%%%%%%%%%%%%%%%%%%%%%%%%%%%%%%%%%%%%%%%%%%%%%%%%%%%%%%%%%%%%%%%%%%
%%%%%%%%%%%%%%%%%%%%%%%%%%%%%%%%%%%%%%%%%%%%%%%%%%%%%%%%%%%%%%%%%%%%%%%%
```

speedOptFMINCON.m

```
%%%%%%%%%%%%%%%%%%%%%%%%%%%%%%%%%%%%%%%%%%%%%%%%%%%%%%%%%%%%%%%%%%%%%%%%
%%%%%%%%%%%%%%%%%%%%%%%%%%%%%%%%%%%%%%%%%%%%%%%%%%%%%%%%%%%%%%%%%%%%%%%%
%This function finds the optimal input sequence for the remainder of the
%experiment conditioned on current state knowledge
function thetaHat=speedOptFMINCON(timeIn, stateIn, alpha0)
global K a y1 A1 y2 A2 y3 A3 y4 A4 xdes currentState currentTime;
currentTime=timeIn; currentState=stateIn;


options=optimset('MaxFunEvals',300, 'MaxIter', 300, 'TolFun', 0.1, 'DiffMinChange', 0.1);

%theta=[D Itilde sigThresh Qsource];


tape_size=4;

alphalow    = 2*ones(tape_size,1);
alphaup    = 12*ones(tape_size,1);



 [thetaHat,g1,g2,g3,g4,g5,hessian]=fmincon(@(alpha) pendfun(alpha), ...
    alpha0,[],[],[],[],alphalow,alphaup,[],options)
% [thetaHat,fval,exitflag,output] = fminsearch(@(alpha) pendfun(alpha),...
%      alpha0,options)
end
```

```
%%%%%%%%%%%%%%%%%%%%%%%%%%%%%%%%%%%%%%%%%%%%%%%%%%%%%%%%%%%%%%%%%%%%%%%%%%%%%%%%
%%%%%%%%%%%%%%%%%%%%%%%%%%%%%%%%%%%%%%%%%%%%%%%%%%%%%%%%%%%%%%%%%%%%%%%%%%%%%%%%
```

pendfun.m

```
%%%%%%%%%%%%%%%%%%%%%%%%%%%%%%%%%%%%%%%%%%%%%%%%%%%%%%%%%%%%%%%%%%%%%%%%%%%%%%%%
%%%%%%%%%%%%%%%%%%%%%%%%%%%%%%%%%%%%%%%%%%%%%%%%%%%%%%%%%%%%%%%%%%%%%%%%%%%%%%%
%///////////////////////////////////////////////////////////////////////////
%This function forward simulated from the current state using alpha_in
%The mean squared error is returned by taking the mean of terminal squareed
%error 100 times when subjected to input noise
function [J] = pendfun(alpha_in)
for monteIter=1:100
    % dynamics dt
    dt = 0.24; T = 24;

    % pendulum parameters
    global K a y1 A1 y2 A2 y3 A3 y4 A4 xdes currentState currentTime;


    N = floor(T/dt)+1-currentTime;
    xtape = zeros(length(currentState),N);
    utape = zeros(1,N);
    alpha = zeros(N,1);
    if nargin>0
        alpha = alpha_in;
    end

    % Simulate forward
    %IC = [0 0]';
    IC = currentState;

    x = IC; %
    for i=1:N-1
        xtape(:,i) = x;
        if i<(6/0.24)
            u=alpha(1);
        else
            u = alpha(ceil(i/(6/0.24)))+2*randn(1);
        end
        utape(i) = u;
        x = x + dynamics(x,u).*dt;
        %x(1)
        %[u i*dt]
    end
    %[x(1);sqrt(4/pi*x(2:end))]
    %size([0:dt:dt*N])
    %size(xtape(1,:))
    % figure(24)
    % subplot(311)
    % plot([dt:dt:dt*N], xtape(1,:));
    %
    % subplot(312)
    % plot([dt:dt:dt*N],xtape(2,:));
    %
    % subplot(313)
    % plot([dt:dt:dt*N],utape);
    % drawnow;

    %dJdalpha = compute_gradients(xtape,utape,dt);
    %dJdalpha=[];
    %J = sum(cost(xtape,utape,dt)) + finalCost(xtape(:,N));
     Jinstance(monteIter) = finalCost(x);
end
J=mean(Jinstance)
end % of pendfun
%///////////////////////////////////////////////////////////////////////////

%///////////////////////////////////////////////////////////////////////////
function C = finalCost(X)
global xdes;

% Xerr = X - repmat(xdes,1,size(X,2));
% Xerr(1,:) = mod(Xerr(1,:)+pi,2*pi)-pi;

[Q,R,Qend] = get_QR;
%IMPLEMENT THE FINAL COST

%C=.5*Xerr'*Qend*Xerr;
sqrt(X)
C=sum((sqrt(4/pi*xdes(2:end))*1e6-sqrt(4/pi*X(2:end))).^2)
end
%///////////////////////////////////////////////////////////////////////////

%%%%%%%%%%%%%%%%%%%%%%%%%%%%%%%%%%%%%%%%%%%%%%%%%%%%%%%%%%%%%%%%%%%%%%%%%%%%%%%%
```

pendfun.m

```
%%%%%%%%%%%%%%%%%%%%%%%%%%%%%%%%%%%%%%%%%%%%%%%%%%%%%%%%%%%%%%%%%%%%%%%%%%%%%%%%%%%%%%%%%%%%%%%%%%%%%
%%%%%%%%%%%%%%%%%%%%%%%%%%%%%%%%%%%%%%%%%%%%%%%%%%%%%%%%%%%%%%%%%%%%%%%%%%%%%%%%%%%%%%%%%%%%%%%%%%%%%
%This function computes the state derivatives
function xdot = dynamics(x,u)
global K a y1 A1 y2 A2 y3 A3 y4 A4 xdes;

A1dot = 80*exp(-a*(y1-x(1,:)).^2);

A2dot = 80*exp(-a*(y2-x(1,:)).^2);

A3dot = 80*exp(-a*(y3-x(1,:)).^2);

A4dot = 80*exp(-a*(y4-x(1,:)).^2);


xdot = [u A1dot A2dot A3dot A4dot]';
end

%%%%%%%%%%%%%%%%%%%%%%%%%%%%%%%%%%%%%%%%%%%%%%%%%%%%%%%%%%%%%%%%%%%%%%%%%%%%%%%%%%%%%%%%%%%%%%%%%%%%%
%%%%%%%%%%%%%%%%%%%%%%%%%%%%%%%%%%%%%%%%%%%%%%%%%%%%%%%%%%%%%%%%%%%%%%%%%%%%%%%%%%%%%%%%%%%%%%%%%%%%%
```

Appendix B

Time Lapse Observation Based Modeling and Identification of Cell Behaviors in Angiogenic Growth

B.1 Introduction

This chapter addresses modeling and system identification of the vessel growth process based on experimental time lapse observation of sprout development in *in vitro* angiogenesis assays. As shown in Fig. 1-1A, angiogenesis begins when one Endothelial Cell (EC) differentiates into a special phenotype, called a "tip cell". This cell begins by breaking out of the existing blood vessel and invades the surrounding scaffold. As it invades further into the matrix, other cells, called "stalk cells" follow behind it (see Fig. 1-1B). When these cells work together in a coordinated fashion, they eventually lead to a tube-like vessel capable of transport. When a new vessel forms, one or multiple new branches may form off of the original. When this process happens in multiple stages, a new vascular network forms to satisfy the need of signaling tissues.

Angiogenesis is an extremely complex process involving the activation and stimulation of ECs by external growth factor concentrations and gradients in the matrix. In addition, the ECs respond to the mechanical properties of the matrix and in-

fluence the matrix properties, both mechanically and chemically [17]. All of these interactions are happening in a heterogeneous environment, where no two cells see the same condition. Also, different cells are operating in different phenotypic states [17], meaning that some cells are tip cells and some are stalk cells, and each cell takes on another functional state such as migratory, proliferative, apoptotic, or quiescent. Despite vast nonuniformity, a collection of ECs is able to behave in a coordinated fashion and generate a complex vascular network.

A predictive mathematical model of angiogenesis is extremely important for determining how to manipulate and coordinate vascular development. A multitude of computational models exist in the literature that have focused on capturing different aspects of the process. See [51] for a good review. However, many of these models are extremely complex, involving hundreds of parameters (see [4], for example) that cannot be estimated from available data. None have been successfully applied to predict how a network will evolve based on current measurements. This work attempts to formulate a lumped parameter model of cell migration based on observed behaviors and involving just a few tunable parameters that may be estimated from data.

This paper will begin by analyzing angiogenic sprout behaviors observed in *in vitro* assays conducted in the laboratory. Next, we will pose a set of lumped parameter cell migration and matrix evolution dynamics based on our experimental observations, findings in the literature, and hypothesis. We will discuss identification of parameters involved in the dynamics and present simulation experiments that address parameter identification given limited measurements from experimental data.

B.2 Angiogenic Behaviors

Experiments are indispensable in gaining insights as to how ECs behave and create a vascular network pattern. Over the last 40 years, angiogenesis experiments have been performed in either *in vivo* environments or *in vitro* environments using traditional on-the-gel dish experiments [23]. The former provides the right environment for the cells to grow, but due to the extreme complexity of the *in vivo* environment, it is

difficult to interpret the data. The latter is simple, but the standard on-the-gel experiment significantly differs from the actual *in vivo* environment.

Recently the authors' research team has developed microfluidic platforms for *in vitro* angiogenesis experiments [15]. The device enables tight control of the delivery of various growth factors, providing an environment much closer to the actual *in vivo* environment than that of the on-the-gel dish experiment. It also provides excellent visibility for observing 3-dimensional cell behaviors using advanced imaging technology, e.g. confocal microscopy with fluorescent markers.

Fig. 1-2 shows the device used for angiogenesis experiments. A collagen gel matrix is formed between micro-fluidic channels A and B. Human Micro-Vascular Endothelial Cells (hMVEC) are seeded on one side of the gel matrix facing Channel B. Fluids containing growth factors and other molecules are delivered to the gel matrix through both channels. The fluid provided to Channel A contains a higher concentration level of VEGF than that of Channel B, so that a uniform gradient of VEGF concentration can be formed across the gel matrix. In response to the gradient of VEGF provided, ECs sprout out and extend towards the higher VEGF concentration. The sprouting process is observed from beneath using a confocal microscope, which can measure 3-dimensional movements of the individual cells. Fig. B-1 shows an example of the type of confocal microscopy data we can obtain. Fig. B-1a shows a sprout that has grown from the monolayer over 24hr. We monitor the growth process using the confocal imaging system and obtain position trajectories for the cells involved in the growth process.

Our experiments using the device have allowed us to watch cell population behavior, i.e. how cells migrate together and what patterns they form. We have made the following observations:

- **Tip cells** The tip cells move in 3D and establish the path or "conduit" that the sprout is going to form into.

- **Stalk cells** The stalk cells migrate along the conduit wall formed by the tip cell toward the tip. As shown in Fig. B-1b, the stalk cells follow the trajectory

taken by the tip cell. A migrating stalk cell can also pass other stalk cells in the quiescent state within the same conduit.

- **Sprout spacing** Once a new sprout is created, no sprout comes out from neighbor cells. Only one cell among many cells in close proximity becomes a tip cell, so that sprouting sites are separated. See Fig. B-2 and [4].

- **Coupling** Cell motions in the sprout appear to be coupled together; migrating stalk cells apparently attract as well as repel each other (not shown).

- **Conduit size** Conduit width is related to tip cell migration speed. If the tip cell migrates quickly, the conduit is narrow. If the tip movies slowly, the conduit is wider. As described in detail later, a tip cell secrets a special protease to degrade the gel matrix. Depending on its speed, the density of protease released per unit distance traveled will be different. A wider conduit is necessary for lumen formation by stalk cells. Fig. B-2 shows how two stalk cells migrate on different sides of the same conduit when it is sufficiently wide. The narrow conduit in Fig. B-1 leads to a line of cells. It was formed by a tip cell that moved $\sim 40\mu$m in 22hr. In contrast, the lumen in Fig. B-2 was formed by a tip cell that moved $\sim 50\mu$m in 16hr.

- **Detachment** When the tip cell migrates too quickly, it detaches from the cells behind it and advances into the scaffold. When the tip gets too far away, the stalk cells lose their sense of directionality and often retract toward the monolayer (not shown).

B.3 Dynamic Modeling

B.3.1 Overview

This chapter forms dynamic equations based on the previous observations, information from the literature, and hypothesis, where no information is known. For simplic-

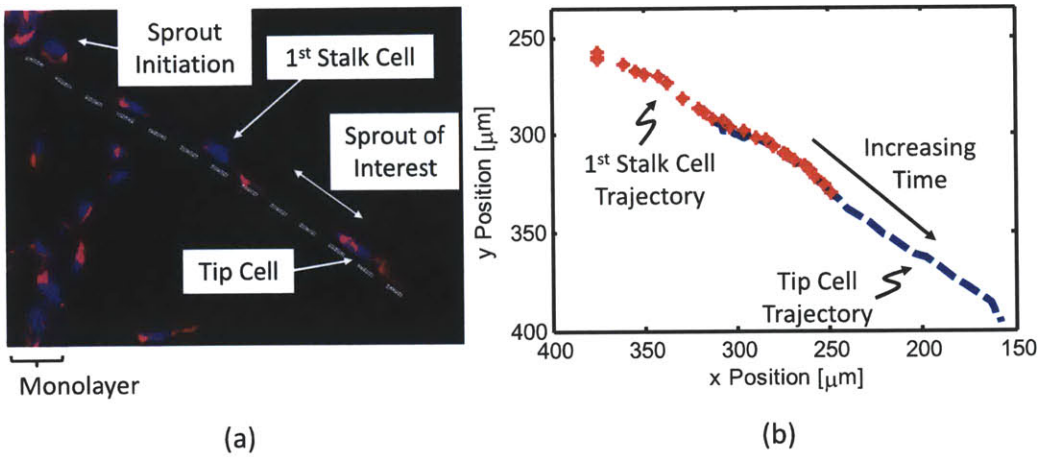

Figure B-1: (A) Tip cell and first stalk cell in sprout; (B) Stalk cell follows the path taken by the tip.

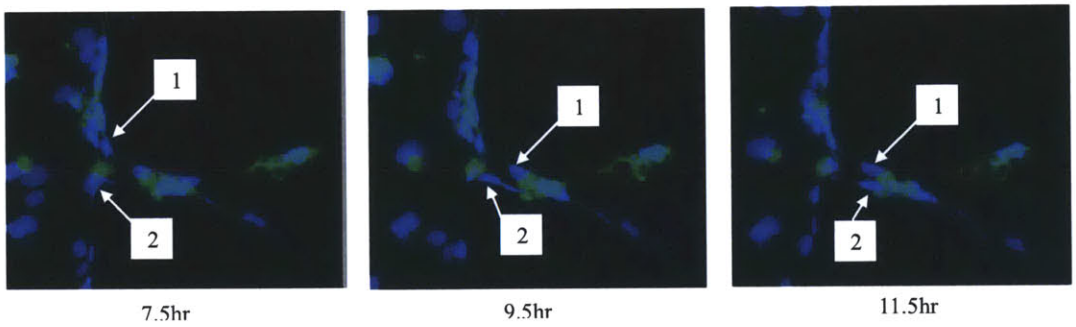

Figure B-2: Stalk cells 1 and 2 migrate on the conduit wall.

ity, we ignore phenotypic state, except for the distinction between tip and stalk cells. For more details on modeling and identification of phenotypic state, see [24, 17].

All cells are numbered from 1 through N, including new cells created through proliferation. Let $\mathbf{x} = [x, y, z]^T \in \Re^3$ be a cartesian coordinate system fixed to the matrix field, and $\mathbf{x}_t^i \in \Re^3$ and $\mathbf{v}_t^i \in \Re^3$ be, respectively, the position and velocity of the i^{th} cell at time t. The position of each cell is represented by the center point of its nucleus. If the cell is a tip cell, they are denoted $\mathbf{x}_t^{tip} \in \Re^3$ and $\mathbf{v}_t^{tip} \in \Re^3$, respectively. All state transitions are described in discrete time with a sampling interval of Δt. As described previously, tip cell and stalk cells have distinct migration mechanisms governed by 3-dimensional vs. 2-dimensional stochastic dynamic equations. The gel

matrix field, on the other hand, is assumed to be deterministic, and is governed mainly by diffusion and binding dynamics of various growth factors [17]. Governing dynamics in each of these phenotype states will be formulated next.

B.3.2 Tip Cell Migration Dynamics

Tip cell migration is a 3-dimensional dynamical process guided by several factors. Most prominent and well studied is the gradient of chemo attractant, VEGF. A tip cell is capable of detecting the gradient of VEGF by extending filopodia in diverse directions [29]. In the following dynamic formulation, only VEGF is considered as an exogenous growth factor that guides the migration of the tip cell. Let $u_t(\mathbf{x}) \in \Re^1$ be the concentration of VEGF at coordinates $\mathbf{x}$ in the matrix field and $\nabla u_t(\mathbf{x}) \in \Re^3$ be the gradient of VEGF concentration at $\mathbf{x}$. The tip cell velocity is directed in the positive VEGF gradient direction:

$$\begin{aligned} \mathbf{v}_{t+1}^{tip} &= \begin{cases} \mathbf{w}_t^{tip} & ; \quad |\nabla u_t| = 0 \\ h_1(\nabla u_t; a_1, d_1) \cdot \frac{\nabla u_t}{|\nabla u_t|} + \mathbf{w}_t^{tip} & ; \quad |\nabla u_t| \neq 0 \end{cases} \\ \mathbf{x}_{t+1}^{tip} &= \mathbf{x}_t^{tip} + (\Delta t)\, \mathbf{v}_t^{tip} \end{aligned} \tag{B.1}$$

where $\mathbf{w}_t^{tip} \in \Re^3$ is an uncorrelated noise with zero mean values and covariance $\mathbf{S}$, and $h_1(\nabla u_t, a_1, d_1)$ is a scalar function that saturates at a_1:

$$h_1(\nabla u_t,\, a_1, d_1) = a_1 \left[1 - \exp\left(-\left|\nabla u_t\right| / d_1\right)\right] \tag{B.2}$$

Parameters a_1 and d_1 as well as covariance $\mathbf{S}$ are to be identified based on experimental data. The scalar function $h_1(\nabla u_t, a_1, d_1)$ is pertinent to the tip cell's abilities to degrade the collagen gel matrix and generate a traction force for moving forward. Therefore, this term depends on the properties of the gel matrix, including stiffness. It is well known that the adhesion of filopodia and lamillopodia to the surrounding gel matrix and contraction of actin fibers inside the filopodia/lamillopodia are the mechanism of generating the traction force. However, details of quantitative mech-

anism are unknown. In this paper these details are left to tuning of parameters, a_1 and d_1, based on actual cell migration data. The function $h_1(\nabla u_t, a_1, d_1)$ saturates, because the tip cell receptors of VEGF are known to saturate in response to a steep VEGF gradient [71]. The noise term $\mathbf{w}_t \in \Re^3$ in the above dynamic equation represents the random walk nature of tip cell migration, which has been reported in several references [51].

As observed in the *in vitro* experiments, the tip cell behavior is affected by stalk cells in the proximity of the tip cell. In case a tip cell is directly connected to a stalk cell through cytoskeleton adhesion, a significant reaction force acts on the tip cell as it pulls the stalk cell. In such situations, the above dynamic equations must be augmented by adding a term representing the inter-cellular forces. Since the above dynamic equations are valid for isolated tip cells, those parameters involved in $h_1(\nabla u_t, a_1, d_1)$ must be obtained from isolated tip cell migration data.

B.3.3 Matrix Field State Equations

The collagen gel matrix is degraded mostly by matrix metalloproteinase (MMP), released by the tip cell. Let $C_{MMP}(\mathbf{x}, t)$ be the concentration of MMP at coordinates $\mathbf{x}$ at time t, and Q_{MMP} be the rate at which MMP is produced by a single tip cell. Assuming no interstitial flow, the MMP released by a tip cell diffuses to the local gel matrix, governed by the following diffusion dynamics [17]:

$$\frac{\partial C_{MMP}(\mathbf{x},t)}{\partial t} = D_{MMP}\nabla^2 C_{MMP}(\mathbf{x},t) + Q_{MMP}\delta(\mathbf{x} - \mathbf{x}_t^{tip}) \tag{B.3}$$

where D_{MMP} is a diffusion coefficient, and $\delta(\bullet)$ is the delta function, which takes 0 other than the tip cell location: $\mathbf{x} = \mathbf{x}_t^{tip}$. As the tip cell migrates, it releases MMP from a different location and in consequence the MMP concentration exhibits a unique distribution depending on the time trajectory of the tip cell.

The MMP degrades the gel matrix by cleaving the cross links of gel fibers. This lowers the "integrity" of the gel matrix, allowing the tip cell to penetrate the gel

matrix. Let $I(\mathbf{x}, t)$ be the integrity of gel matrix at coordinates $\mathbf{x}$ and time t.

$$\frac{\partial I(\mathbf{x}, t)}{\partial t} = -k_{c-m} C_{MMP}(\mathbf{x}, t) I(\mathbf{x}, t) \tag{B.4}$$

where k_{c-m} is the rate at which the gel matrix is cleaved by MMP.

B.3.4 Directed Stalk Cell Migration

Stalk cells migrate along the conduit created in a gel matrix. Similar to tip cell migration, stalk cell migration is directionally guided. The detail mechanism of directional guidance is not known. However, the experimental observations strongly suggest that each stalk cell has the ability to detect the direction of the tip cell. For a stalk cell to detect the direction solely based on the local information it can sense, there must be some form of gradient signal spread across the conduit and its vicinity. Therefore, we hypothesize that a tip cell leaves cues that spread out within the conduit creating a gradient signal and that stalk cells are guided by the gradient.

Let $q_t(\mathbf{x})$ be the strength of the cue generated by a tip cell and observed at coordinates $\mathbf{x}$ at time t. The guided migration of a stalk can be described as:

$$\begin{aligned} \mathbf{v}_{t+1}^i &= \mathbf{v}_t^i (1 - b) + a_2 \cdot \nabla q_t \left(\mathbf{x}_t^i\right) + \mathbf{w}_t^{stalk} \\ \mathbf{x}_{t+1}^i &= \mathbf{x}_t^i + (\Delta t)\, \mathbf{v}_t^i \end{aligned} \tag{B.5}$$

where parameter b in the first term represents viscous damping that the faster moving stalk cells are likely to feel while migrating in the conduit, the second term forces the stalk cell in the positive gradient of cue intensity, and the final term is a random walk term. Recall that stalk cells often move at a significantly higher speed than a tip cell and thereby the viscous damping may not be ignored, unlike the tip cell migration. The damping may be due to the degraded collagen products left in the conduit as well as integrin binding to the conduit wall.

The cues are generated by the tip cell and thereby the intensity $q_t(\mathbf{x})$ reflects the migration trajectory of the tip cell. Similar to the release of MMP, the cues are released by the tip cell at different locations as it migrates. As a result, the cue

intensity has a spatiotemporal distribution, similar to that of MMP. Furthermore, the *in vitro* experimental observations provide insights into how the cue $q_t(\mathbf{x})$ should be constructed. Specifically, the data revealed two stalk cell behaviors characteristic to its guided migration pertinent to the assumed cues intensity.

- Stalk cells often became unable to track the conduit as the distance to the tip cell got longer.
- Stalk cells often became unable to track the conduit as the time elapsed since the conduit was first created by the tip cell.

The latter implies that cue intensity decays with time. The former implies that the cues released by the tip cell dilute as the distance gets longer. Based on these observations, we consider the following simple dynamic model for generating

$$q_{t+1}(\mathbf{x}) = \alpha \cdot q_t(\mathbf{x}) + a_3 \exp\left(-\frac{|\mathbf{x} - \mathbf{x}_t^{tip}|}{d_2}\right) \tag{B.6}$$

where α is to determine the time decay rate, $0 < \alpha < 1$ and a_3 and d_2 are, respectively, the intensity scale and the distance scale of the cues released by the tip cell. Since the parameter a_2 in Eq. B.5 also indicates the intensity scale, parameter a_3 can be set to 1 without loss of generality. Given a tip cell trajectory, $\mathbf{x}_\tau^{tip}$, $0 \leq \tau \leq t$, the cue intensity $q_t(\mathbf{x})$ can be computed from B.6 with initial condition $q_0(\mathbf{x}) = 0$. Taking the spatial derivatives of $q_t(\mathbf{x})$ and using them in Eq. B.5 yield the directed stalk cell migration dynamics.

B.3.5 Crawling on the Conduit Wall

The stalk cell migration is basically 2-dimensional, being constrained to the wall surface of the conduit. According to the matrix field state equations, B.3 and B.4, the matrix integrity varies continually across the cross sectional matrix field, as opposed to a rigid surface having discontinuity in integrity level. When migrating, stalk cells tend towards the free space to avoid constraints or resistive forces, but at the same time stalk cells have to adhere to rigid matrix fibers in order to generate a traction force.

These two conflicting requirements take a stalk cell to a middle ground somewhere between the highest and the lowest integrity levels. Let I_{nom} be the middle ground nominal value of the matrix integrity. When a stalk cell deviates from the middle ground, a type of restoring force should work on the cell, so that it can tend towards the right level of matrix integrity I_{nom}. This restoring effect can be written as

$$\mathbf{R}\left(\mathbf{x}_t^i\right) = -R\left(I\left(\mathbf{x}_t^i, t\right) - I_{nom}\right)\nabla I\left(\mathbf{x}_t^i, t\right) \tag{B.7}$$

where R is a scalar gain and $I\left(\mathbf{x}_t^i, t\right)$ is the integrity level at $\mathbf{x}_t^i$ derived from Eqs. B.3 and B.4.

The above method for forcing stalk cells to crawl on a conduit wall requires rather heavy computations of the matrix field state equations, B.3 and B.4. If the conduit location is known or visually observable, 2-dimensional migration dynamics can be described as a differential-algebraic equation (DAE), using a geometric constraint equation, which is algebraic. Suppose that the conduit wall, or more rigorously, the plane where the integrity level is I_{nom}, is given by an implicit function:

$$g_t\left(\mathbf{x}\right) = 0 \tag{B.8}$$

Then the 2-dimensional migration dynamic equations are given by Eq. B.5 subject to the algebraic constraint: $g_t\left(\mathbf{x}\right) = 0$. This DAE model will be used for parameter estimation in the following section.

Multiple stalk cells often interact with each other, influencing other cell's migration dynamics. For example, we often observe that multiple cells move together within the same conduit. Also, we observe that a stalk cell passes other stalk cells within the same conduit. As more stalk cells are recruited to a conduit and new cells are created through proliferation, the cell density increases within the conduit, and thereby more interactions may occur. There are at least three types of cell-cell interaction mechanisms, and the details are current research issues in cell biology. At the present work, which is largely based on time lapse cell trajectory observation, we focus on the type of cell-cell interactive forces that correlate with the relative locations of their nuclei:

$\mathbf{f}(\mathbf{x}_t^j - \mathbf{x}_t^i)$, $i \neq j$. When adjacent cells are too close, a repelling force is generated to push them away. When they are at a certain distance, they attract each other, but the attractive force diminishes as the distance gets longer. We consider the following function $\mathbf{f}$ for the interactive force between cells i and j with $\Delta\mathbf{x}_t^{ij} = \mathbf{x}_t^j - \mathbf{x}_t^i$:

$$\mathbf{f}\left(\Delta\mathbf{x}_t^{ij}\right) = \begin{cases} c_1 \cdot \operatorname{sinc}\left(\frac{\left|\Delta\mathbf{x}_t^{ij}\right|}{\gamma}\right) \frac{\Delta\mathbf{x}_t^{ij}}{\left|\Delta\mathbf{x}_t^{ij}\right|}, & 0 < \left|\Delta\mathbf{x}_t^{ij}\right| \leq \gamma \\ c_2 \cdot \operatorname{sinc}\left(\frac{\left|\Delta\mathbf{x}_t^{ij}\right|}{\gamma}\right) \frac{\Delta\mathbf{x}_t^{ij}}{\left|\Delta\mathbf{x}_t^{ij}\right|}, & \gamma \leq \left|\Delta\mathbf{x}_t^{ij}\right| \leq 2\gamma \end{cases} \tag{B.9}$$

for $j \neq i$, $1 \leq i, j \leq N$ where c_1, c_2, and γ are parameters to tune.

Adding collective forces from all surrounding cells to the previous dynamic equations yields

$$\begin{aligned} \mathbf{v}_{t+1}^i &= \mathbf{v}_t^i (1-b) + a_2 \nabla q_t - \sum_{j \neq i} \mathbf{f}\left(\mathbf{x}_t^j - \mathbf{x}_t^i\right) + \mathbf{w}_t^{stalk} \\ \mathbf{x}_{t+1}^i &= \mathbf{x}_t^i + (\Delta t)\, \mathbf{v}_t^i \end{aligned} \tag{B.10}$$

subject to $g_t(\mathbf{x}_t^i) = 0$. We will use this form of stalk cell migration dynamics for stochastic system identification.

B.4 Stochastic Identification

B.4.1 Approach

Based on the experimental observations and the literature information, a set of parametric models for describing the behavior of sprouting ECs have been obtained. These models explain many of the experimental results and reflect the literature information, yet the models include hypothetical sub-processes that have not yet been verified or firmly grounded on biochemistry. These include the guidance mechanism of stalk cell migration, forces acting between adjacent cells, local properties of the gel matrix degraded by a tip cell, the branch formation mechanism, and so forth. Extensive research efforts in biochemistry are required for verifying these poorly understood sub-processes. To supplement those efforts, however, this section presents a synthetic

approach to verifying the model. Namely, we integrate all the sub-processes and synthesize emergent behaviors that can be identified with observable data. The tip cell migration process, for example, is an aggregated process comprised of many sub-processes, including VEGF gradient detection by filopodia, secretion of MMP, degradation of the gel matrix, adhesion to matrix fibers, traction force generation, and so on. These facets have been aggregated into the tip cell migration dynamics having just a few parameters and the phenotype state transition model. This synthesized model predicts variables that are directly observable, i.e. migration velocities. The parameters involved can be determined by comparing the predicted velocities against observed data: a standard procedure of system identification. The error covariance associated with the system identification may indicate the validity of the model and the quality of prediction. Although those experimental data are phenomenological trajectory data, they reflect aggregate effects of many sub-processes.

The *in vitro* microfluidic experiments of EC sprouting provides time lapse data of tip cells and stalk cells as well as monolayer sprouting and branching processes. For each of three major measurements, a). tip cell migration, b). stalk cell migration, and c). monolayer sprouting and branching, the parameter estimation can be performed in sequence. After identifying the three observable processes, the entire emergent behavior, i.e. the blood vessel pattern formation, will be derived.

We use the Maximum Likelihood Estimate (MLE) for estimating the parameters involved in each observable model. MLE is simple, yet it provides a consistent estimate even for nonlinear systems. In our problem, the parameters are involved nonlinearly in each of the observable models.

B.4.2 Estimating Parameters of Tip Cell Migration

We assume that the gradient of VEGF concentration is uniform over the gel matrix field. In other words, the concentration varies linearly across the gel matrix. This can be accomplished with a two channel micro-fluidic device [15]. We also assume that the initial matrix stiffness and integrity are uniform across the gel matrix. Then the parameters to identify are two parameters involved in the saturation function, a_1

and d_1, and the variance of the Gaussian noise $\mathbf{w}_t^{tip}$. Let θ be the parameter vector containing all these parameters to estimate. The tip cell velocity at time $t+1$ can be predicted based on the dynamic model in Eq. B.1 as

$$\hat{\mathbf{v}}_{t+1}^{tip}\left(\nabla u_t;\hat{\theta}\right) = h_1\left(\nabla u_t;\hat{a}_1,\hat{d}_1\right)\cdot\frac{\nabla u_t}{|\nabla u_t|} \tag{B.11}$$

where $\hat{z}$ represents estimate of unknown variable or parameter z. The prediction error is given by the discrepancy from the actual measurement $\mathbf{v}_{t+1}^{tip}$

$$\phi(t,\theta) = \mathbf{v}_{t+1}^{tip} - \hat{\mathbf{v}}_{t+1}^{tip}\left(\nabla u_t;\hat{\theta}\right) = \mathbf{v}_{t+1}^{tip} - h_1\left(\nabla u_t;\hat{a}_1,\hat{d}_1\right)\cdot\frac{\nabla u_t}{|\nabla u_t|} \tag{B.12}$$

Assuming that the model structure is correct, it follows from the tip cell dynamic model (1) that the probability distribution of the prediction error $\phi\left(t,\theta_0\right)$ is Gaussian with zero mean values for the correct parameter distribution θ_0, since the prediction error comes from the uncorrelated noise $\mathbf{w}_t^{tip}$.

$$p_\Phi\left(\phi\left(t\right);\theta_0\right) \sim N\left(0,\mathbf{S}\right) \tag{B.13}$$

where $\mathbf{S}$ is the error covariance of noise $\mathbf{w}_t^{tip}$. This implies that the prediction error is independent with respect to time t, and the Maximum Likelihood Estimate of the parameter vector based on $t=1$ through T data is then given by

$$\hat{\theta}_{tip}^{MLE}\left(T\right) = \arg\min_{\theta}\left(\sum_{t=1}^{T}\phi(t,\theta)^T\mathbf{S}^{-1}\phi(t,\theta) + \ln|\mathbf{S}|\right) \tag{B.14}$$

If the covariance is isotropic, $\mathbf{S} = \sigma_{tip}^2\mathbf{I}$, the number of parameters to estimate reduces to only three: $\theta_{tip} = \begin{bmatrix} a_1 & d_1 & \sigma_{tip} \end{bmatrix}^T$.

B.4.3 Estimating Parameters of Stalk Cell Migration

Assuming again that the covariance of the Gaussian noise $\mathbf{w}_t^{stalk}$ is isotropic, $\sigma_{stalk}^2\mathbf{I}$, the parameters to estimate are $\theta_{stalk} = [b,\ a_2,\ d_2,\ \alpha,\ c_1,\ c_2,\ \gamma,\ \sigma_{stalk}]^T$, where b is the viscous damping, a_2, d_2, and α are associated with the cue intensity, and c_1, c_2,

and γ are for cell-cell interactive forces.

Eliminating the uncorrelated noise term $\mathbf{w}_t^{stalk}$, the velocity predictor is given by

$$\begin{aligned}\hat{\mathbf{v}}_{t+1}^i(\mathbf{v}_t^i;\hat{\theta}_{stalk}) = \mathbf{v}_t^i(1-\hat{b}) + \hat{a}_2\nabla q_t(\mathbf{x}_t^i;\hat{\alpha},\mathbf{x}_\tau^{tip},0\le\tau\le t) \\ -\sum_{j\neq i}\mathbf{f}(\mathbf{x}_t^j-\mathbf{x}_t^i;\hat{c}_1,\hat{c}_2,\hat{\gamma})\end{aligned} \tag{B.15}$$

Note that the stalk cell migration is constrained to the wall of the conduit. The predicted velocity does not necessarily lie on the conduit wall. The prediction error in the direction normal to the conduit wall is meaningless. Therefore, for parameter estimation we use only the two components of the prediction error that is parallel to the wall surface. The challenge is that the number of parameters is high for the stalk cell migration dynamics. Experimental data containing a rich variety of data segments associated with diverse cell-cell interactions are necessary to identify these parameters.

B.5 Simulation Experiments

The cell sprouting model obtained previously is now examined through simulation experiments. Considering the complexity of the process, it is necessary to investigate the feasibility of the proposed method of synthetic process identification prior to applying the method to actual experimental data. This can be done by using a known process for which the true parameter values are known. Stochastic simulations are performed to create a data set. Then the system identification method is applied in order to examine whether the original parameter values are recovered from the data set. If the model structure is not adequate, the parameter estimation process will not converge. Though it converges, a lot of data will be required. The covariance of estimation error will also provide us with useful information in designing actual experiments.

The first simulation experiment described below focuses on the dynamics of single sprout growth. The simulation consists of a collection of 17 cells that begin distributed

Table B.1: Migration parameter values.

Tip Cells			Stalk Cells							
a_1	d_1	σ_{tip}	b	a_2	d_2	σ_{stalk}	α	c_1	γ	c_2
1	20	0.25	0.5	0.5	10	0.25	0.5	2	10	0.4

in a monolayer in the yz-plane at $x = 10$. A cell in the center of the plane is differentiated into a tip cell and takes on the dynamics of Eq. B.1, which responds to a gradient applied on the x-direction alone:$\nabla u = \begin{bmatrix} \nabla u_x & 0 & 0 \end{bmatrix}^T$.

The remaining cells take on stalk cell dynamics as given by Eq. B.10. The scaffold matrix dynamics are given by an approximation to Eq. B.4 and Eq. B6. The nominal parameter values used in the simulation are given in Table 1. These parameter values are used throughout this chapter.

Fig. B-3 shows the output of the simulation under different conditions. The color contour in each part defines constant matrix integrity, I, while the solid black contours are lines of constant q. Fig. B-3a shows the cell locations after time $t = 10$, projected into the xy-plane at $z = 50$. Fig. B-3b shows the same information at $t = 100$ when the VEGF gradient is too high, $\nabla u_x = 80$. When the gradient is too high, the tip cell migrates too quickly into the gel and the stalk cells become separated from it. When the tip cell is too far away, any stalk cells that have migrated into the conduit may retract toward the gel. Fig. B-3c shows what happens when the VEGF gradient is chosen at a lower value, $\nabla u_x = 10$. In this case, the tip sprouts out and stalk cells follow it into conduit. A stable, hollow, lumen forms and can continue to grow. Fig. B-3d shows the same stable lumen with cells projected onto the yz-plane at $x = 15$. The lumen cells are spatially distributed on different sides of the conduit where the matrix integrity is approximately $I = I_{nom}$.

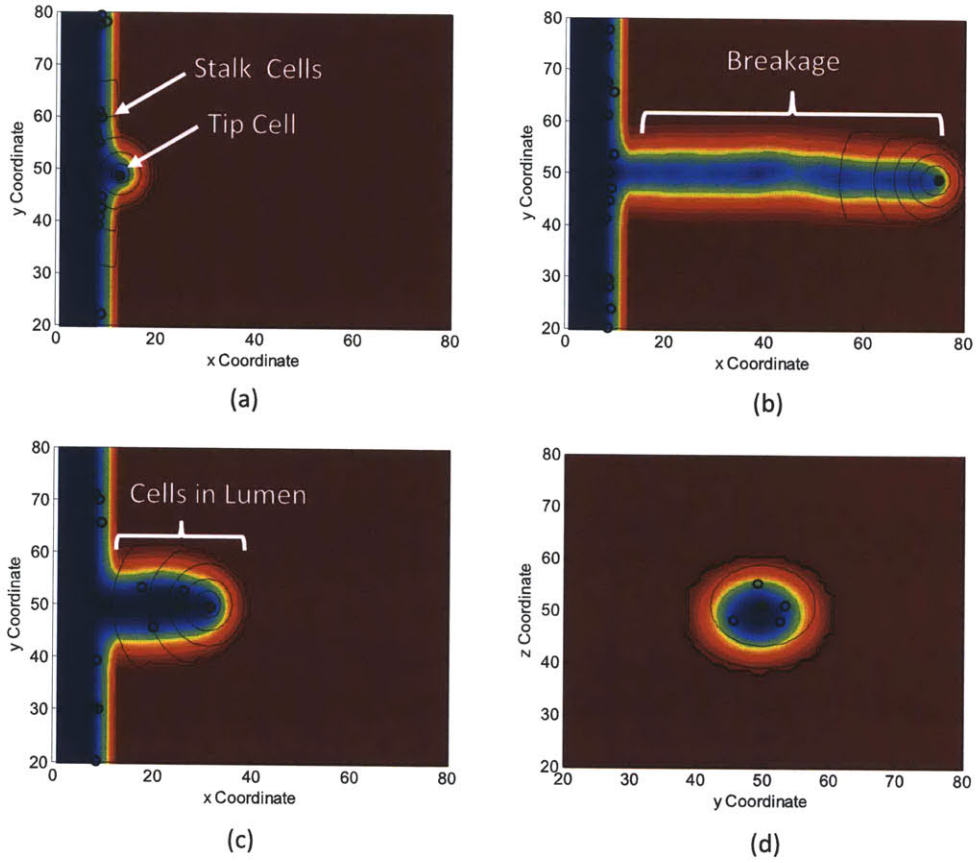

Figure B-3: Simulation of single sprout growth.

B.5.1 System ID

Tip Cells

We can form a MLE estimator using data obtained from the simulation described in the previous section. In physical experiments, we only have access to cell location trajectory information, $\mathbf{x}_t^{tip}$ and $\mathbf{x}_t^i$ and applied VEGF gradient, ∇u_x.

Using the MLE, we can estimate the parameters involved in the dynamic equations. We can get an idea of how much data we need by estimating the unknown parameters with different amounts of data for an ensemble of different simulation experiments. Then we can compute the ensemble mean and variance of parameter estimation error. Fig. B-4 shows the results for estimating the tip cell parameters, a_1, d_1, and σ_{tip}. In each of the ensemble simulations, the simulation had the same

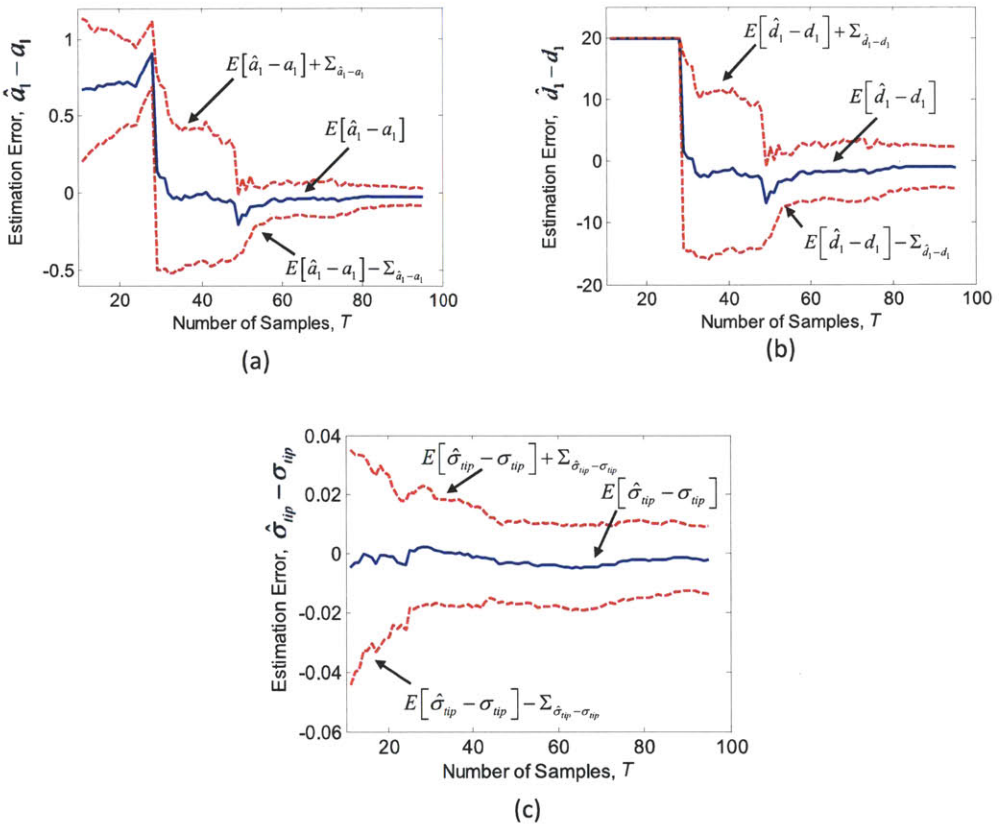

Figure B-4: Ensemble mean parameter estimation error with standard deviation.

initial conditions. Also, the initial guess for the parameters was $\bar{a}_1 = 2$, $\bar{d}_1 = 20$, and $\bar{\sigma}_{tip} = 0.5$. Here, we used three sets of data with different levels of VEGF gradient, ∇u_x. The first data set with $\nabla u_x = 10$ was used for the first 28 time steps, followed by the data set of $\nabla u_x = 40$, and then $\nabla u_x = 80$.

Initially, with just the data from a single level of input, there is not enough information to correctly estimate the chemotactic saturation function parameters. Thus, the optimization maximizing the log-likelihood function does not correctly estimate a_1 and d_1. The results show that three levels of input excitation are good enough to obtain the correct parameter values, and the ensemble expected parameter estimation error decreases to zero. The tip cell dynamics only have three parameters and can be correctly estimated with just three levels of system input, ∇u_x.

Stalk Cells

The parameters involved in the stalk cell equation of motion are considerably more difficult to estimate than the tip cell parameters. The difficulty arises from several factors. First, there are a total of eight parameters involved in the stalk cell equations, compared with just three parameters in the tip cell equation. Some of the eight parameters may be coupled so that changing two of them may have similar effect on the migration of the stalk cells. This means that it may not be possible to uniquely identify all of the parameters. Particularly challenging is the fact that the hypothesized chemoattractant, $q(\mathbf{x})$, is unknown. Also, since the restoring force due to the boundary is generated normal to the wall, we can merely ignore the component of cell motion normal to the wall and use only the components parallel to the wall for estimation.

To examine the validity and identifiability of the model structure, we first consider the case where the cue intensity $q(\mathbf{x})$ is known. This reduces the number of parameters to identify to six. Table 2 shows the parameter estimation results using the same data used in the previous section. The expectation and variance are computed from the estimate over all 10 data sets. Note that all the parameters are reliably identified.

It is nice to see how well different parameters can be estimated because it gives a clear idea of how important each term is in the governing dynamics. Any parameters that are poorly estimated are either part of a term which has a small influence over the overall cell dynamics or are lumped with other parameters. While the true parameters are unknown in a physical experiment, the ensemble parameter estimation variance gives clues about how a model should be retailored.

Note that with these estimates, the mean and standard deviation of the output estimation error are $E[\hat{\mathbf{v}}_t^i - \mathbf{v}_t^i] = -0.01$ and $\Sigma_{\hat{\mathbf{v}}_t^i - \mathbf{v}_t^i} = 0.26$, respectively. Theoretically, with $\sigma_{stalk} = 0.25$, the best we can possibly do is $E[\hat{\mathbf{v}}_t^i - \mathbf{v}_t^i] = 0$ and $\Sigma_{\hat{\mathbf{v}}_t^i - \mathbf{v}_t^i} = 0.25$.

Since we do not know $q(\mathbf{x})$ in practice, we have to address the full estimation problem with a total of eight parameters in θ_{stalk}. Unfortunately, with the observable information from the simulation alone, i.e., stalk position, there is not enough infor-

Table B.2: Estimation results with $q(\mathbf{x})$ known.

	b	a_2	γ	c_1	c_2	σ_{stalk}
True Val.	0.50	0.50	10.0	2.0	0.40	0.25
Est. Val.	0.50	0.54	10.06	1.81	0.40	0.25
Error Var. $\times 10^2$	0.01	0.06	0.64	1.40	0.12	0.00

Table B.3: Estimation results with $q(\mathbf{x})$ unkown.

	b	a_2	d_2	α	γ	c_1	c_2	σ_{stalk}
True Val.	0.50	0.50	10.0	0.50	10	2.0	0.40	0.25
Est. Val.	0.49	0.53	10.13	–	10.00	2.00	0.43	0.25
Error Var. $\times 10^2$	1.78	7.49	77.61	–	9.09	5.96	3.56	0.38

mation to reliably estimate all of the system parameters. In fact we cannot reliably estimate any of the system parameters if α also needs to be estimated. In practice, it will be necessary to estimate some of the parameters from independent experiments. For example, α can be estimated based on a systematic set of studies to see how fast the tip cell can migrate into the gel while stalk cells are still following. The larger the data set, the better the parameter can be estimated. Here, we use the same parameters and input used previously, and assume α is known. Table 3 shows the ensemble estimation results over 10 data sets. The estimator once again works well.

B.6 Conclusion

This work has presented a method for developing a set of lumped parameter dynamic equations for EC motion in angiogenesis and testing/tuning the model against data. This approach will allow multiple model structures or hypotheses to be tested against each other to see which model better explains the data. These models can be tested in simulation before application to experimental data to ascertain how confidently the parameters can be estimated and whether the model should be revised based on what can be identified from measurable data. In addition, a simple model with few

tunable parameters will be useful for predicting process evolution and understanding how different components of the process dynamics influence process evolution and stability.

Bibliography

[1] T. Asahara, D. Chen, T. Takahashi, K. Fujikawa, M. Kearney, M. Magner, G.D. Yancopoulos, and J.M. Isner. Tie2 receptor ligands, angiopoietin-1 and angiopoietin-2, modulate vegf-induced postnatal neovascularization. *Circulation Research*, 83(3):233–240, 1998.

[2] A.L. Bauer, T.L. Jackson, and Y. Jiang. A cell-based model exhibiting branching and anastomosis during tumor-induced angiogenesis. *Biophysical journal*, 92(9):3105–3121, 2007.

[3] Amy L. Bauer, Trachette L. Jackson, and Yi Jiang. Topography of extracellular matrix mediates vascular morphogenesis and migration speeds in angiogenesis. *PLoS Comput Biol*, 5(7):e1000445, 07 2009.

[4] K. Bentley, H. Gerhardt, and P.A. Bates. Agent-based simulation of notch-mediated tip cell selection in angiogenic sprout initialisation. *Journal of Theoretical Biology*, 250(1):25–36, 2007.

[5] Katie Bentley, Giovanni Mariggi, Holger Gerhardt, and Paul A. Bates. Tipping the balance: Robustness of tip cell selection, migration and fusion in angiogenesis. *PLoS Comput Biol*, 5(10):e1000549, 10 2009.

[6] D.A. Berk, F. Yuan, M. Leunig, and R.K. Jain. Fluorescence photobleaching with spatial fourier analysis: measurement of diffusion in light-scattering media. *Biophysical Journal*, 65(6):2428 - 2436, 1993.

[7] D.P. Bertsekas. *Dynamic programming and optimal control.* Number v. 1 in Athena Scientific optimization and computation series. Athena Scientific, 2005.

[8] David E. Birk, Frederick H. Silver, and Robert L. Trelstad. *Cell Biology of Extracellular Matrix*, chapter Matrix Assembly, pages 221–249. Springer, 2nd edition, 1991.

[9] L. Bonetta. Flow cytometry smaller and better. *Nature methods*, 2(10):785–795, 2005.

[10] C.E. Brinckerhoff and L.M. Matrisian. Matrix metalloproteinases: a tail of a frog that became a prince. *Nature Reviews Molecular Cell Biology*, 3(3):207–214, 2002.

[11] G.S. Butler, M.J. Butler, S.J. Atkinson, H. Will, T. Tamura, S.S. van Westrum, T. Crabbe, J. Clements, M.P. dOrtho, and G. Murphy. The timp2 membrane type 1 metalloproteinase receptor regulates the concentration and efficient activation of progelatinase a. *Journal of Biological Chemistry*, 273(2):871, 1998.

[12] E. F. Camacho and C. Bordons. *Model Predictive Control.* Springer, 2nd ed. edition, 2004.

[13] H.S. Carslaw and J.C. Jaeger. *Conduction of heat in solids.* Oxford science publications. Clarendon Press, 1986.

[14] T.H. Chun, F. Sabeh, I. Ota, H. Murphy, K.T. McDonagh, K. Holmbeck, H. Birkedal-Hansen, E.D. Allen, and S.J. Weiss. Mt1-mmp-dependent neovessel formation within the confines of the three-dimensional extracellular matrix. *Journal of Cell Biology*, 2004.

[15] S. Chung, R. Sudo, P.J. Mack, C.R. Wan, V. Vickerman, and R.D. Kamm. Cell migration into scaffolds under co-culture conditions in a microfluidic platform. *Lab on a Chip*, 9(2):269–275, 2009.

[16] D.C. Darland and P.A. D'Amore. Blood vessel maturation: vascular development comes of age. *Journal of Clinical Investigation*, 103:157–158, 1999.

[17] Anusuya Das, Doug Lauffenburger, Harry Asada, and Roger Kamm. A hybrid contimuum-discrete modeling approach to predicting and controlling angiogenesis: Analysis of combinatorial gorwth factor and matrix effects on vessel sprouting morphology. *accepted for publication in Phil. Trans. A*, 2010.

[18] Elena I. Deryugina, Boris Ratnikov, Edward Monosov, Tanya I. Postnova, Richard DiScipio, Jeffrey W. Smith, and Alex Y. Strongin. Mt1-mmp initiates activation of pro-mmp-2 and integrin [alpha]v[beta]3 promotes maturation of mmp-2 in breast carcinoma cells. *Experimental Cell Research*, 263(2):209 – 223, 2001.

[19] J.L. Doob. *Stochastic processes.* Wiley publications in statistics. Wiley, 1953.

[20] D. English, Z. Welch, A.T. Kovala, K. Harvey, O.V. Volpert, D.N. Brindley, and J.O.E.G.N. Garcia. Sphingosine 1-phosphate released from platelets during clotting accounts for the potent endothelial cell chemotactic activity of blood serum and provides a novel link between hemostasis and angiogenesis. *The FASEB Journal*, 14:2255–2265, 2000.

[21] William R. English, Batrice Holtz, Gavin Vogt, Vera Knuper, and Gillian Murphy. Characterization of the role of the mt- loop. *Journal of Biological Chemistry*, 276(45):42018–42026, 2001.

[22] A.B. Ennett, D. Kaigler, and D.J. Mooney. Temporally regulated delivery of vegf in vitro and in vivo. *Journal of Biomedical Materials Research Part A*, 79(1):176–184, 2006.

[23] S. Even-Ram and K.M. Yamada. Cell migration in 3D matrix. *Current opinion in cell biology*, 17(5):524–532, 2005.

[24] W. Farahat and H. Asada. Identification of phenotypic state transition probabilities in living cells. In *Proceedings of the 2nd ASME Dynamical Systems and Control Conference*, Hollywood, CA, 2009.

[25] Waleed A. Farahat, Levi B. Wood, Ioannis K. Zervantonakis, Alisha Schor, Sharon Ong, Devin Neal, Roger D. Kamm, and H. Harry Asada. Ensemble analysis of angiogenic growth in three-dimensional microfluidic cell cultures. *Submitted, PLoS One*, 2011.

[26] R. Fletcher. *Practical Methods of Optimization: Unconstrained optimization.* Practical Methods of Optimization. J. Wiley, 1980.

[27] Judah Folkman and Michael Klagsbrun. Angiogenic factors. *Science*, 235(4787):pp. 442–447, 1987.

[28] Y. Funahashi, C.J. Shawber, A. Sharma, E. Kanamaru, Y.K. Choi, and J. Kitajewski. Notch modulates vegf action in endothelial cells by inducing matrix metalloprotease activity. *Journal of Angiogenesis Research*, 3(1):1–13, 2011.

[29] Holger Gerhardt. Vegf and endothelial guidance in angiogenic sprouting. In Christiana Ruhrberg, editor, *VEGF in development*, Molecular Biology Intelligence Unit, chapter 6, pages 68–78. Springer New York, 2008.

[30] Carina Hellberg, Arne Östman, and C.-H. Heldin. Pdgf and vessel maturation. In Rüdiger Liersch, Wolfgang E. Berdel, and Torsten Kessler, editors, *Angiogenesis Inhibition*, volume 180 of *Recent Results in Cancer Research*, pages 103–114. Springer Berlin Heidelberg, 2010.

[31] L. Holmgren, A. Glaser, S. Pfeifer-Ohlsson, and R. Ohlsson. Angiogenesis during human extraembryonic development involves the spatiotemporal control of pdgf ligand and receptor gene expression. *Development*, 113(3):749, 1991.

[32] C.P. Huang, J. Lu, H. Seon, A.P. Lee, L.A. Flanagan, H.Y. Kim, A.J. Putnam, and N.L. Jeon. Engineering microscale cellular niches for three-dimensional multicellular co-cultures. *Lab chip*, 9(12):1740–1748, 2009.

[33] Y. Itoh, A. Takamura, N. Ito, Y. Maru, H. Sato, N. Suenaga, T. Aoki, and M. Seiki. Homophilic complex formation of mt1-mmp facilitates prommp-2 activation on the cell surface and promotes tumor cell invasion. *The EMBO journal*, 20(17):4782–4793, 2001.

[34] Trachette Jackson and Xiaoming Zheng. A cell-based model of endothelial cell migration, proliferation and maturation during corneal angiogenesis. *Bulletin of Mathematical Biology*, 72:830–868, 2010. 10.1007/s11538-009-9471-1.

[35] E A Jaffe, C R Minick, B Adelman, C G Becker, and R Nachman. Synthesis of basement membrane collagen by cultured human endothelial cells. *The Journal of Experimental Medicine*, 144(1):209–225, 1976.

[36] R.K. Jain. Molecular regulation of vessel maturation. *Nature medicine*, 9(6):685–693, 2003.

[37] L. Jakobsson, C.A. Franco, K. Bentley, R.T. Collins, B. Ponsioen, I.M. Aspalter, I. Rosewell, M. Busse, G. Thurston, A. Medvinsky, S. Schulte-Merker, and H. Gerhardt. Endothelial cells dynamically compete for the tip cell position during angiogenic sprouting. *Nature Cell Biology*, pages 943–945, 2010.

[38] E.D. Karagiannis and A.S. Popel. Distinct modes of collagen type i proteolysis by matrix metalloproteinase (mmp) 2 and membrane type i mmp during the migration of a tip endothelial cell: insights from a computational model. *Journal of theoretical biology*, 238(1):124–145, 2006.

[39] T. Kaully, K. Kaufman-Francis, A. Lesman, and S. Levenberg. Vascularization: The conduit to viable engineered tissues. *Tissue Engineering Part B: Reviews*, 15(2):159–169, 2009.

[40] Farrah Kheradmand, Kirtee Rishi, and Zena Werb. Signaling through the egf receptor controls lung morphogenesis in part by regulating mt1-mmp-mediated activation of gelatinase a/mmp2. *Journal of Cell Science*, 115(4):839–848, 2002.

[41] W.B. Kiosses, S.J. Shattil, N. Pampori, and M.A. Schwartz. Rac recruits high-affinity integrin $\alpha v\beta 3$ to lamellipodia in endothelial cell migration. *Nature cell biology*, 3(3):316–320, 2001.

[42] N. Koike, O.G. Dai Fukumura, P. Au, J.S. Schechner, and R.K. Jain. Tissue engineering: creation of long-lasting blood vessels. *Nature*, 428(6979):138–139, 2004.

[43] S.S. Kulkarni, R. Orth, M. Ferrari, and N.I. Moldovan. Micropatterning of endothelial cells by guided stimulation with angiogenic factors. *Biosensors and Bioelectronics*, 19(11):1401–1407, 2004.

[44] P.K. Kundu and I.M. Cohen. *Fluid mechanics*. Number v. 10 in Fluid mechanics. Academic Press, 2008.

[45] H.J. Kushner. On the stability of stochastic dynamical systems. *Proceedings of the National Academy of Sciences of the United States of America*, 53(1):8, 1965.

[46] L. Lamalice, F. Le Boeuf, and J. Huot. Endothelial cell migration during angiogenesis. *Circulation research*, 100(6):782, 2007.

[47] E. Lammert, O. Cleaver, and D. Melton. Induction of pancreatic differentiation by signals from blood vessels. *Science*, 294(5542):564, 2001.

[48] M.W. Laschke, Y. Harder, M. Amon, I. Martin, J. Farhadi, A. Ring, N. Torio-Padron, R. Schramm, M. Rucker, D. Junker, et al. Angiogenesis in tissue engineering: breathing life into constructed tissue substitutes. *Tissue Engineering*, 12(8):2093–2104, 2006.

[49] J.D. Leslie, L. Ariza-McNaughton, A.L. Bermange, R. McAdow, S.L. Johnson, and J. Lewis. Endothelial signalling by the notch ligand delta-like 4 restricts angiogenesis. *Development*, 134(5):839, 2007.

[50] David J. C. Mackay. *Information Theory, Inference and Learning Algorithms*. Cambridge University Press, 1st edition, June 2003.

[51] N.V. Mantzaris, S. Webb, and H.G. Othmer. Mathematical modeling of tumor-induced angiogenesis. *Journal of Mathematical Biology*, 49(2):111–187, 2004.

[52] Susanna Monaco, Valentina Sparano, Magda Gioia, Diego Sbardella, Donato Di Pierro, Stefano Marini, and Massimo Coletta. Enzymatic processing of collagen iv by mmp-2 (gelatinase a) affects neutrophil migration and it is modulated by extracatalytic domains. *Protein Science*, 15(12):2805–2815, 2006.

[53] G. Murphy, H. Stanton, S. Cowell, G. Butler, V. Knauper, S. Atkinson, and J. Gavrilovic. Mechanisms for pro matrix metalloproteinase activation. *Apmis*, 107(1-6):38–44, 1999.

[54] H. Nagase, R. Visse, and G. Murphy. Structure and function of matrix metalloproteinases and timps. *Cardiovascular research*, 69(3):562–573, 2006.

[55] Hideaki Nagase. *Matrix Metalloproteinases*, chapter Stromelysins 1 and 2, pages 43–84. Academic Press, San Diego, 1998.

[56] Y. Nishida, H. Miyamori, E.W. Thompson, T. Takino, Y. Endo, and H. Sato. Activation of matrix metalloproteinase-2 (mmp-2) by membrane type 1 matrix metalloproteinase through an artificial receptor for prommp-2 generates active mmp-2. *Cancer Research*, 68(21):9096–9104, 2008.

[57] Sara S. Nunes, Kevin A. Greer, Chad M. Stiening, Helen Y.S. Chen, Kameha R. Kidd, Mark A. Schwartz, Chris J. Sullivan, Harish Rekapally, and James B. Hoying. Implanted microvessels progress through distinct neovascularization phenotypes. *Microvascular Research*, 79(1):10 – 20, 2010.

[58] L. Odhner and H. Asada. Stochastic recruitment: Controlling state distribution among swarms of hybrid agents. In *American Control Conference, 2008*, pages 4226 –4231, june 2008.

[59] P. Oses, M.A. Renault, R. Chauvel, L. Leroux, C. Allieres, B. Seguy, J.M.D. Lamaziere, P. Dufourcq, T. Couffinhal, and C. Duplaa. Mapping 3-Dimensional Neovessel Organization Steps Using Micro-Computed Tomography in a Murine Model of Hindlimb Ischemia. *Arteriosclerosis, thrombosis, and vascular biology*, 2009.

[60] H.C. Ott, T.S. Matthiesen, S.K. Goh, L.D. Black, S.M. Kren, T.I. Netoff, and D.A. Taylor. Perfusion-decellularized matrix: using nature's platform to engineer a bioartificial heart. *Nature medicine*, 14(2):213–221, 2008.

[61] Mingxing Ouyang, Jie Sun, Shu Chien, and Yingxiao Wang. Determination of hierarchical relationship of src and rac at subcellular locations with fret biosensors. *Proceedings of the National Academy of Sciences*, 105(38):14353–14358, 2008.

[62] M.L. Patterson, S.J. Atkinson, V. Kn
"auper, and G. Murphy. Specific collagenolysis by gelatinase a, mmp-2, is determined by the hemopexin domain and not the fibronectin-like domain. *FEBS letters*, 503(2-3):158–162, 2001.

[63] L.-K. Phng and Holger Gerhardt. Angiogenesis: A team effort coordinated by notch. *Developmental Cell*, 16(2):196 - 208, 2009.

[64] MJ Plank, BD Sleeman, and PF Jones. A mathematical model of tumour angiogenesis, regulated by vascular endothelial growth factor and the angiopoietins. *Journal of theoretical biology*, 229(4):435–454, 2004.

[65] S. Joe Qin and Thomas A. Badgwell. An overview of industrial model predictive control technology. pages 232–256, 1997.

[66] AA Qutub, G Liu, P Vempati, and AS Popel. Integration of angiogenesis modules at multiple scales: from molecular to tissue. *Pac Symp Biocomput*, pages 316–327, 2009.

[67] Amina Qutub and Aleksander Popel. Elongation, proliferation & migration differentiate endothelial cell phenotypes and determine capillary sprouting. *BMC Systems Biology*, 3(1):13, 2009.

[68] Myrto Raftopoulou and Alan Hall. Cell migration: Rho gtpases lead the way. *Developmental Biology*, 265(1):23 – 32, 2004.

[69] R.C.A. Sainson, J. Aoto, M.N. Nakatsu, M. Holderfield, E. Conn, E. Koller, and C.C.W. Hughes. Cell-autonomous notch signaling regulates endothelial cell branching and proliferation during vascular tubulogenesis. *The FASEB Journal*, page 04, 2005.

[70] W.B. Saunders, K.J. Bayless, and G.E. Davis. Mmp-1 activation by serine proteases and mmp-10 induces human capillary tubular network collapse and regression in 3d collagen matrices. *Journal of cell science*, 118(10):2325–2340, 2005.

[71] A. Shamloo, N. Ma, M. Poo, L.L. Sohn, and S.C. Heilshorn. Endothelial cell polarization and chemotaxis in a microfluidic device. *Lab on a Chip*, 8(8):1292–1299, 2008.

[72] T. Shemesh, A.B. Verkhovsky, T.M. Svitkina, A.D. Bershadsky, and M.M. Kozlov. Role of focal adhesions and mechanical stresses in the formation and progression of the lamellum interface. *Biophysical journal*, 97(5):1254–1264, 2009.

[73] A.N. Stratman, W.B. Saunders, A. Sacharidou, W. Koh, K.E. Fisher, D.C. Zawieja, M.J. Davis, and G.E. Davis. Endothelial cell lumen and vascular guidance tunnel formation requires mt1-mmp-dependent proteolysis in 3-dimensional collagen matrices. *Blood*, 114(2):237–247, 2009.

[74] M.G. Tonnesen, X. Feng, and R.A.F. Clark. Angiogenesis in wound healing. In *Journal of Investigative Dermatology Symposium Proceedings*, volume 5, pages 40–46. Nature Publishing Group, 2000.

[75] M. Toth, I. Chvyrkova, M.M. Bernardo, S. Hernandez-Barrantes, and R. Fridman. Pro-mmp-9 activation by the mt1-mmp/mmp-2 axis and mmp-3: role of timp-2 and plasma membranes. *Biochemical and biophysical research communications*, 308(2):386–395, 2003.

[76] Rui D. M. Travasso, Eugenia Corvera Poire, Mario Castro, Juan Carlos Rodrguez-Manzaneque, and A. Hernandez-Machado. Tumor angiogenesis and vascular patterning: A mathematical model. *PLoS ONE*, 6(5):e19989, 05 2011.

[77] V. Vickerman, J. Blundo, S. Chung, and R. Kamm. Design, fabrication and implementation of a novel multi-parameter control microfluidic platform for three-dimensional cell culture and real-time imaging. *Lab Chip*, 8(9):1468–1477, 2008.

[78] Levi Wood, Roger Kamm, and Harry Asada. Stochastic modeling and identification of emergent behaviors of an endothelial cell population in angiogenic pattern formation. *The International Journal of Robotics Research*, 30(6):659–677, 2011.

[79] I. Yana, H. Sagara, S. Takaki, K. Takatsu, K. Nakamura, K. Nakao, M. Katsuki, S. Taniguchi, T. Aoki, H. Sato, et al. Crosstalk between neovessels and mural cells directs the site-specific expression of mt1-mmp to endothelial tip cells. *Journal of Cell Science*, 120(9):1607–1614, 2007.

[80] I.K. Zervantonakis, S. Chung, R. Sudo, M. Zhang, J.L. Charest, and R.D. Kamm. Concentration gradients in microfluidic 3d matrix cell culture systems. *International Journal of Micro-Nano Scale Transport*, 1(1):27–36, 2010.